Master of Science Thesis

Semi-Analytical Buckling and Optimisation of Variable Stiffness, Variable Thickness Laminates.

Lander Vertonghen

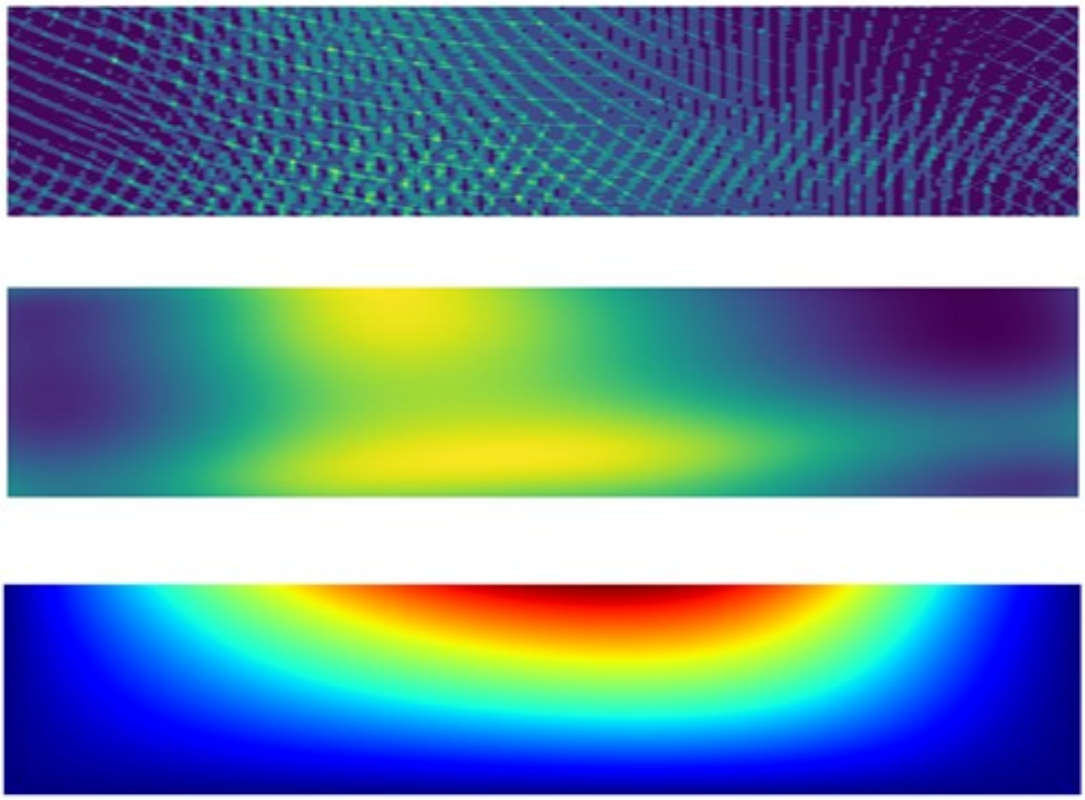

Faculty of Aerospace Engineering · Delft University of Technology

TU Delft Delft University of Technology

Semi-Analytical Buckling and Optimisation of Variable Stiffness, Variable Thickness Laminates.

Master of Science Thesis

For obtaining the degree of Master of Science in Aerospace Engineering
at Delft University of Technology

Lander Vertonghen

13/12/2019

Faculty of Aerospace Engineering · Delft University of Technology

Delft University of Technology
Faculty of Aerospace Engineering
Department of Aerospace Structures and Materials

GRADUATION COMMITTEE

Dated: 13/12/2019

Chair holder:

Prof. dr. C. Bisagni

Committee members:

Dr.-Ing. S.G.P. Castro

Dr. ir. D.M.J. Peeters

Abstract

Variable Angle Tow designs have shown to improve structural performance by providing a better stiffness distribution. However, additional manufacturing constraints are involved compared to straight fibre laminates: mainly the maximum fibre steering curvature that can be achieved. Moreover, if a gap free laminate is constructed, overlaps will be formed depending on the relative fibre orientation when the continuous tows are bent to follow a reference path in Automated Fibre Placement and a one-sided irregular thickness profile is created. To counter the latter effect and still obtain uniform thickness laminates, a cut and restart strategy of the tows is often used in industry, leaving the final product with small gap areas. However, previous research has hinted both numerically and experimentally on further buckling improvements of variable stiffness laminates incorporating overlaps, resulting in a variable thickness profile.

To investigate these possible benefits and their extent, the thickness build-up and overlap locations are specially considered in this proposed framework on Variable Angle Tows. In first instance, a virtual manufacturing surrogate of the laminate is produced to represent the discrete thickness profile due to the overlaps. This is performed by plotting each tow graphically and subsequently retracing the total thickness based on the superimposed opacity over the laminate. The tow paths are obtained from the interpolated fibre orientation, which simultaneously incorporates the steering limit of the manufacturing process. The surrogate information is then compared to a smeared approximation of the thickness build-up, based solely on the steering angle.

The linear buckling simulation is performed by means of a semi-analytical model on a plate formulation, where the one-sided thickness profile variation is modelled by incorporating an offset from the geometrical varying midplane to a common one, around which the laminate stiffnesses are calculated. These adapted stiffnesses are then used in solving the neutral equilibrium buckling problem, where the displacements are approximated by means of the Ritz method, with a set of Legendre polynomial shape functions and numerical integration of the stiffness matrices.

The semi-analytical smeared model correlates to within $\pm 5\%$ of the discrete thickness Finite Element Model for a range of geometries, loading and boundary conditions. This verifies the thickness approximation for linear buckling of small tow widths compared to the laminate's dimensions, yet was inconclusive for larger tow width ratios. Finally, laminates with a varying thickness profile are optimised alongside the variable stiffness for different cases and compared to uniform thickness counterparts at isomass. The results show small improvements in the symmetric problem, but a higher gain is obtained for unsymmetrical conditions with an unrestricted layup sequence, as the thickness increase can be highly tailored together with the variable fibre orientation to locations requiring higher stiffness.

Preface

This thesis rapport represents the end of my time as a student at the Delft University of Technology. It have been six and a half great years, however I am looking forward to what the future will bring. I would like to thank in particular my supervisor Dr.-Ing. Saullo G.P. Castro, for the interesting discussions and guidance during this project. Furthermore, I appreciate the insights provided by Dr. ir. Daniël M.J. Peeters. Finally, I would like to give a special consideration to friends and family who have supported me throughout my studies, in good and rough times.

Lander Vertonghen
13 December 2019
Delft

Contents

List of Figures

List of Tables

Nomenclature

Acronyms

AFP	Automated Fibre Placement
CLPT	Classical Lamination Plate Theory
CP	Control Point
CS	Constant Stiffness
CTS	Continuous Tow Shearing
FEM	Finite Element Method
FSDT	First-order Shear Deformation Theory
OHC	Open Hole Compression
OHT	Open Hole Tension
TPE	Total Potential Energy
TSL	Tow Steered Laminates
VAT	Variable Angle Tow
VSL	Variable Stiffness Laminates

Symbols

$[\bar{B}]$	Strain matrix	$[-, 1/mm]$
$[B_0]$	Linear strain components	$[-, 1/mm]$
$[B_L]$	Non-linear strain components	$[-]$
c	Amplitude associated with shape function g in the Ritz method	$[mm]$
E_{xx}	Longitudinal stiffness	$[MPa]$
E_{yy}	Transverse stiffness	$[MPa]$
F_{ext}	Distributed in-plane loading condition	$[N/mm]$
g	Shape functions in the Ritz approximation	$[-]$
G_{xy}	Shear stiffness	$[MPa]$
$[K_0]$	Linear constitutive stiffness matrix	$[N/mm]$
$[K_{G_0}]$	Geometric stiffness matrix	$[N/mm]$
L	Length of the laminate	$[mm]$
$[M]$	Applied edge moments	$[Nmm/mm]$
$[N]$	Applied edge loads	$[N/mm]$
$[N_{K_G}]$	Initial membrane stress matrix	$[N/mm]$
N_s	Number of sampling points	$[-]$
$N_{overlaps}$	Number of sampling points	$[-]$
r_s	Radius of curvature	$[mm]$
$[Q]$	Ply plane stress stiffness matrix	$[MPa]$
$[S_u]$	Row vector containing the in-plane shape functions in x direction	$[-]$
$[S_v]$	Row vector containing the in-plane shape functions in y direction	$[-]$

$[S_w]$	Row vector containing the out-of-plane shape functions	$[-]$
t_{avg}	Average thickness	$[mm]$
t_{local}	Local thickness	$[mm]$
t_{max}	Maximum thickness	$[mm]$
t_{min}	Minimum thickness	$[mm]$
t_{tow}	Tow thickness	$[mm]$
U	Strain energy	$[mJ]$
u_{bend}	Bending displacement	$[mm]$
u^0	Stretching displacement	$[mm]$
V	External work	$[mJ]$
W	Width of the laminate	$[mm]$
w	Tow width	$[mm]$
$w(x, y)$	Out-of-plane displacement	$[mm]$
w_e	Effective tow width	$[mm]$
$x' - y'$	Manufacturing coordinate system	$[mm]$
$x - y$	Global coordinate system	$[mm]$

Greek Symbols

α	Opacity value	$[-]$
β	Bending rotation	$[rad]$
$\Delta x'$	Step size	$[mm]$
ϵ	In-plane strain	$[-]$
$\{\epsilon\}$	Strain vector	$[-, 1/mm]$
θ	Global fibre orientation	$[°]$
κ	Out-of-plane curvature	$[1/mm]$
λ	Buckling eigenvalue	$[-]$
ν_{xy}	Poisson's ratio	$[-]$
Π	Total potential energy	$[mJ]$
ρ	Fibre steering curvature	$[1/m]$
ρ_{mat}	Material density	$[kg/m^3]$
σ	Stress vector	$[MPa]$
ϕ	Local manufactured fibre orientation	$[°]$
Φ	Buckling eigenmode coefficients corresponding to λ	$[-]$
χ	Ply rotation angle	$[°]$
$\xi - \eta$	Natural coordinate system	$[mm]$

Chapter 1

Introduction

In the aerospace industry, weight reduction has always been an important goal in order to increase efficiency. This has caused a shift in the materials, from wood to metal until lately composites, such as on the Boeing 787 or Airbus A350. Owing to their specific strength and stiffness, combined with their mechanical tailoring properties, composite materials have been employed more extensively. The latest composite developments involve the emergence of Tow Steered Laminates (TSL), also called Variable Angle Tow (VAT) laminates, increasing structural capabilities by incorporating a higher degree of tailoring.

The early use of local fibre steering was performed in order to increase open hole strength [1]. Later on, Biggers et al. [2] strategically positioned uni-directional strips in order to improve the buckling capabilities of composite plates, locally varying the stiffness and benefiting from load redistribution. The addition of these strips resulted in Variable Stiffness Laminates (VSL). Building upon this idea of varying the stiffness distribution locally, VAT laminates were created. VAT laminates consist in the spatial variation of the fibre orientations within a ply, as opposed to straight fibres, as used in conventional Constant Stiffness (CS). This difference is shown in Figure 1.1. Besides buckling improvements, the advantages of VAT laminates have been further shown in decreasing stress concentrations by arranging the fibres along the principal stress directions [3] and increasing the post-buckling loading before failure [4].

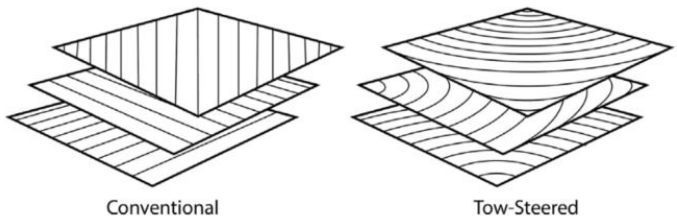

Figure 1.1: Conventional CS laminate on the left, and tow steered VAT laminate on the right [5].

Moreover, the manufacturing process is an important part along with the material and structural design making up the trinity concept. With the introduction of varying fibre orientations, traditional production methods for conventional laminates had to be adapted or new ones created, due to the added steering challenges to be taken into account. Each of them brings along a set of limitations, required to be taken into account in the design phase to achieve feasible products, but also side effects in the form of an irregular thickness profile. The latter effects will be investigated in this research, along the variable stiffness.

This report is set up as follow: Part I is an overview of a literature and this thesis research questions, and starts by giving background information about VAT characterisation and production in Chapter 2. This includes a discussion on the angle variation modelling, the distinct manufacturing methods and their limitations. Furthermore, different modelling techniques for linear buckling are addressed in Chapter 3, followed by the obtained results and outcomes. Based on this review, Chapter 4 sets out the research objective and questions for this thesis.

In Part II, the methodology applied during this thesis and theoretical background are presented. Chapter 5 first outlines the virtual manufacturing procedure and special considerations due to the varying thickness to take into account. Thereafter, the assumptions and theory regarding linear buckling of VAT is discussed in Chapter 6, for both the semi-analytical model and Finite Element Method (FEM) verification. Moreover, the optimisation and verification cases are explained in Chapter 7.

Afterwards, Part III is dedicated to the results of this thesis. The verification of the virtual manufacturing procedure is performed in Chapter 8, followed by the verification of semi-analytical tool and the thickness approximation in Chapter 9. Once these methods have been proven suitable to represent varying thickness VAT, the optimisation results are explored in Chapter 10. Subsequently, the optimised results are compared with a FEM shell formulation in Chapter 11.

Finally, the conclusion to this research is given in Chapter 12, stating the most important findings. Building upon those, recommendations for further work or improvements are given in Chapter 13.

Part I

Literature Review

Chapter 2

Variable Angle Tows

The design of VAT has been inspired and based on the mechanism of CS laminates characterisation, however distinct difference arise from the spatial variation of the fibres. This chapter treats with these specific considerations and how they have been dealt with in previous work. First, the representation of the varying fibre trajectories is discussed in Section 2.1, followed by the stiffness representation of the laminate in Section 2.2. Finally manufacturing methods and their particularity are examined in Section 2.3, with a special attention to these particularities on the final product of these phenomena in Section 2.4.

2.1 Fibre Path Definition

The most important part of VAT is the variation of the fibre orientation and consequently its path definition, as it is not straight anymore. Several non-linear variation methods have been proposed and adopted in the industry, e.g. a combination of B splines [6] or Bezier curves [7]. However a linear angle variation description, the most simple case, has been implemented broadly in the investigation of VAT [4], and is discussed in Section 2.1.1. Another representation involving Lagrange polynomials is treated in Section 2.1.2, as it allows for a compact definition, yet being non-linear and versatile. Lastly, the conversion from lamination parameters to a VAT stacking sequence is briefly discussed in Section 2.1.3.

Before describing the different path possibilities, some generic terms associated to the definition are explained: the shift and variation direction. The first one refers to the direction along which the fibre angle remains constant and the tow path is simply shifted when placed during manufacturing. On the contrary, the variation axis is aligned with the direction along which the fibre orientation is changed.

2.1.1 Linear Angle Variation

The linear angle variation was proposed by Guerdal et al. [8], where the variation happens along one local axis (x'), as shown in Figure 2.1. The mathematical definition of this variation is given by Equation 2.1. When the axis system is rotated by an angle ϕ with respect to the global axis, then the fibre orientation variation is not one dimensional anymore, but becomes a function of both global planar coordinates, i.e. $\theta = \theta(x, y)$.

$$\theta(x') = \phi + (T_1 - T_0)\frac{|x'|}{d} + T_0 \tag{2.1}$$

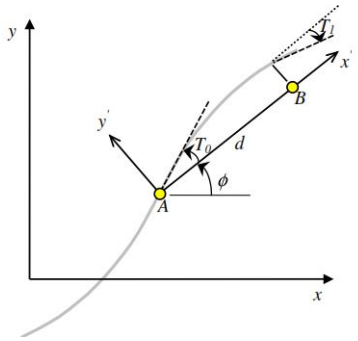

Figure 2.1: Linear fibre path variation [8].

T_1 and T_0 are angle values at two predetermined points, at a distance d apart along the x' axis. Equation 2.1 gives the fibre orientation, which is related to the fibre path by means of Equation 2.2 [9].

$$\frac{dx}{dy} = \tan\theta \tag{2.2}$$

2.1.2 Non-Linear Angle Variation

To allow a more complex and wider design space, non-linear fibre orientations have also been adopted. Wu et al. [10] suggested a non-linear angle variation based on Lagrange interpolation and Control Points (CP) scheme. Any two dimensional changing fibre path, as shown in Figure 2.2 a), can be represented by an interpolation between predefined points with associated angle values θ_{mn}, as represented in Figure 2.2 b). The mathematical definition of the Lagrange interpolation is given in Equation 2.3, where the complete fibre path can also be rotated by an angle ϕ. The addition of CP results in a higher degree of the interpolation polynomial, and subsequent non-linearity of the distribution. Simultaneous, a wider variety of paths can be obtained [11].

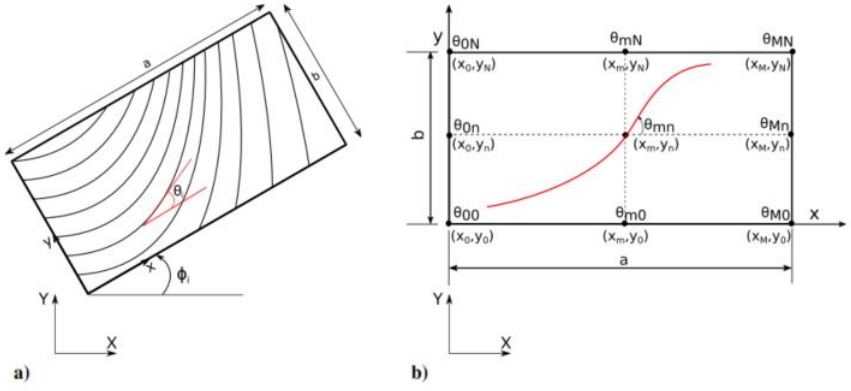

Figure 2.2: Tow steered ply representation: a) fibre path angle and orientation, b) interpolation and control point location [11].

$$\theta_i(x,y) = \Phi_i + \sum_{m=0}^{M}\sum_{n=0}^{N}\theta_{mn}\prod_{k=0,k\neq m}^{M}\frac{x-x_k}{x_m-x_k}\prod_{p=0,p\neq n}^{N}\frac{y-y_p}{y_n-y_p} \tag{2.3}$$

The benefit of an interpolation method, is that the interpolation variables are also the angle values at the CP [10]. Furthermore, it profits the simulations by reducing the amount of variables needed to define the tow paths. Early FEM research into VAT defined a different stacking sequence per element, inherent to the mesh and mesh size [12]. This would lead to over thousands of variables to optimise for, whereas CP method only use a few dozens. However, this procedure limits the design space [13].

The two dimensional interpolation can also become one dimensional, where CP are only used along one axis, and it then reduces to Equation 2.4. In the limit case of only two CP point in a one dimensional configuration at the extremes of the laminate, the linear variation as discussed in Section 2.1.1 is obtained [10].

$$\theta(x) = \Phi_i + \sum_{m=0}^{M}\theta_m\prod_{k\neq m}^{M}\frac{x-x_k}{x_m-x_k} \tag{2.4}$$

De Quadros et al. [14] applied the same interpolation method on the lamination parameters' distribution, by controlling the curvature and "*resulting in smoother distributions of stiffness and, as a consequence, possibly leading to a laminate with smoother fiber angle curvatures*" [14]. Finally, in the case of a two dimensional varying fibre orientation, no global shifting and variation direction can be defined.

2.1.3 Retrieval from Lamination Parameters

In case of VAT analysis with lamination parameters, introduced in Section 2.2.2, these parameters must then be converted back to a feasible stacking sequence over the plate. Van Campen et al. [15] used a generic algorithm combined with a gradient based optimiser to evaluate initial guesses of a stacking sequence and thereafter converge to the desired equivalent optimum lamination parameters on a local basis at each nodal location. They also included steering curvature constraints, by evaluating the modulus of the gradient of the fibre orientation, to incorporate the manufacturing constraint, as discussed in Section 2.3.

2.2 Stiffness Representation

In order to simulate the structural behaviour of TSL, their mechanical properties must be defined. The same approach is used as for CS straight fibre laminates, representing VAT characteristics by means of the ABD matrix, directly from the stacking sequence, or in terms of lamination parameters.

2.2.1 ABD Matrix

The ABD matrix is the result of the thin plate classical lamination theory [8] and represents the laminate behaviour to applied edge loads (N) and moments (M) to the in-plane strains ε and out-of-plane curvatures κ, as reported in Equation 2.5. It is a function of the stacking sequence and material properties. More details on plate modelling theories are presented in Section 3.1.1.

$$\begin{bmatrix} N \\ M \end{bmatrix} = \begin{bmatrix} A & B \\ B & D \end{bmatrix}\begin{bmatrix} \varepsilon \\ \kappa \end{bmatrix} \tag{2.5}$$

The A matrix describes the in-plane stiffness terms, including the shear-extension coupling, as does the D matrix with the out-of-plane behaviours, bending and twisting. The B matrix on the other hand, couples the in and out-of-plane behaviour. However, with the spatial fibre variation, the stacking sequence with associated fibre orientation changes constantly. Therefore, the ABD matrix terms are no more constant for a given laminate, but instead are a function of the location, i.e. ABD = ABD(x,y).

2.2.2 Lamination Parameters

The ABD matrix is the constitutive relation for laminates, however it can be defined alternatively. Lamination parameters, introduced by Hahn and Tsai [16], allow for a compact representation of the stacking sequence regardless of the amount of plies and their orientations. The lamination parameters are bound and related to each other through trigonometric relations, enforcing a valid range [17]. The definition of the in-plane (V) lamination parameters is given in Equation 2.6 as an example. Subsequently, the A matrix is linearly related to these lamination parameters by means of Equation 2.7 [12]. The B and D matrix are derived in an analogous manner [18].

$$(V_1, V_2, V_3, V_4) = \int_{-1/2}^{1/2} \bar{z}^2(\cos 2\theta(\bar{z}), \sin 2\theta(\bar{z}), \cos 4\theta(\bar{z}), \sin 4\theta(\bar{z}))d\bar{z} \tag{2.6}$$

$$A = \frac{h}{12}(\Gamma_0 + V_1\Gamma_1 + V_2\Gamma_2 + V_3\Gamma_3 + V_4\Gamma_4) \tag{2.7}$$

$\theta(\bar{z})$ is the fibre angle distribution throughout the normalised thickness $\bar{z}$, defined as z/h, the local height over the complete thickness. Γ_0 to Γ_4 are invariant material matrices, based on the mechanical properties of a ply. As lamination parameters only give the stiffness matrices, a stacking sequence must be found to approximate this stiffness distribution afterwards. As for the initial ABD matrix, the lamination parameters also vary spatially for VAT laminates.

Using lamination parameters allows to find the global optimum solution to specific problems [12], as well as reducing the computational time for the ABD matrix computation. However, a stacking sequence matching the stiffness distribution must be obtained afterwards, which is not always physically possible [15]. Methods to convert the lamination parameters to a stacking sequence were discussed in Section 2.1.3.

2.3 Manufacturing

New and current CS manufacturing methods have been invented or adapted to be able to produce fibre steering capabilities. Nowadays, two main manufacturing methods are available for VAT production: Automated Fibre Placement (AFP) and Continuous Tow Shearing (CTS). Both have advantages and disadvantages, as well as constraints. They differentiate each other, mainly by their application method: AFP bends the fibres, whereas CTS shears them to follow the reference path. The difference in shown in Figure 2.3.

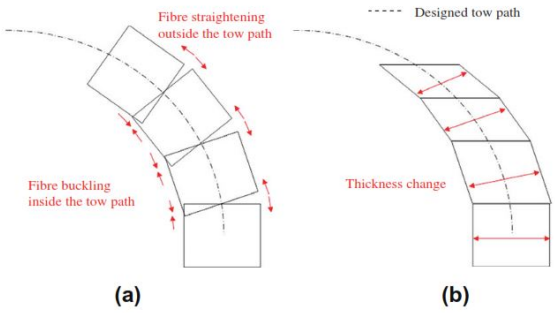

Figure 2.3: Tow steering principle during the manufacturing process: a) AFP, b) CTS [19].

2.3.1 Automated Fibre Placement

AFP is the first invented method, and follows directly from CS manufacturing machines. It consists in a machine head capable of placing, cutting and restarting simultaneous up to 32 individual different tows [20]. During this process, the final product includes defects, in terms of gaps or overlaps, as displayed in Figure 2.4. The influence of the defects is further discussed in Section 2.4.

Width variation

When a fibre is bent to follow a reference path, the effective width w_e of the tow changes as shown in Figure 2.4. This transformation was approximated by Blom et al. [9] by means of Equation 2.8, relating the local fibre orientation ϕ and tow width w.

$$w_e \approx \frac{w}{\cos \phi} \tag{2.8}$$

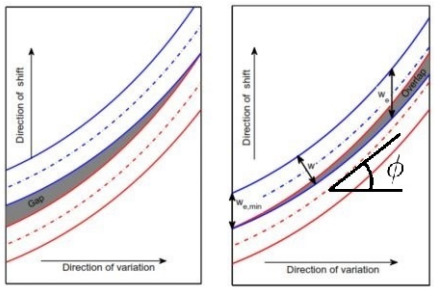

(a) Gap between two courses (b) Overlapping courses

Figure 2.4: VAT manufacturing results: AFP with gaps (a) and AFP with overlaps (b), adapted from [9].

Defects

Defects are caused by the non-parallel path course due to the variable steering angle and subsequent width variation. This involves the creation of overlaps, as displayed in Figure 2.4. However, if overlaps are to be avoided, the tow shift between two course can be increased, creating gaps in the product [21]. Gaps are resin rich pockets, and may become predominant location for damage and failure [22]. In case of buckling, overlaps are preferred to gaps, as discussed in Section 3.4.

Alternatively, the tow drop method can be used to try and avoid overlaps and fill up gaps. This consists in using the cut and restart capabilities of the AFP process. The principle is to place a tow between gaps, or to stop a tow before contributing to a longer overlap region as shown in Figure 2.5.

This capability is governed by two important parameters: L_{cut} and L_{add}. L_{cut} is the minimum tow length that can possibly be used: this is usually dependent on the manufacturing head and consists in the distance to the cutting mechanism. L_{add} is the minimum gap length that will be recognised, i.e. how long a gap must be before it will be filled up by a tow. The latter is a parameter that can be controlled by the designer, placing tows more frequently for smaller L_{add} values, however increasing manufacturing costs and times [5].

Therefore, AFP manufacturing programs are typically configured based on relative gap (a_g) and overlap (a_o) percentages. These are the ratios between either the overlap or gap region and the tow width. The gap region is defined as the distance between 2 adjacent tows, indicated by $a_g w$ in Figure 2.5. The overlap region is the total amount of common overlay with both adjacent tows, illustrated by $a_0 w$ in Figure 2.5. If during the production process, the actual gap ratio remains greater than the predefined gap percentage (i.e. $h_{g/o}/w \geq a_g$), tows will keep on being added. Alternatively, the tows will be cut in case the overlap ratio is smaller than the negative overlap percentage (i.e. $h_{g/o}/w \leq -a_o$). Typical a_g and a_o values are 50-50% [5].

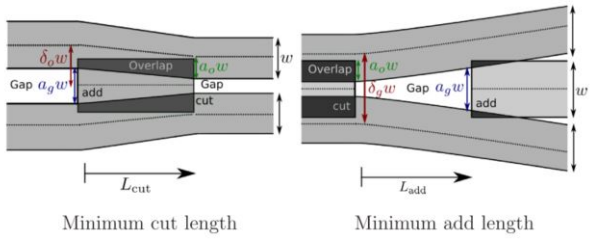

Figure 2.5: Cut and restart tactics [5].

Curvature Constraints

During the AFP manufacturing process, fibres are prone to wrinkling and twisting, as shown in Figure 2.6 [5, 23]. This is a direct result from compressive strains applied on the inner side of the curved fibres. To counter this effect, the path curvature is constrained, and early assumptions used a maximum curvature ρ of 1.575 $1/m$ [13], regardless of material properties.

Therefore, further specific research was conducted into the influence of different material properties. Beakou et al. [23] looked into the effect of material tackiness on the wrinkling behaviour. By means of semi-analytical modelling, they incorporated the tackiness as out-of-plane springs and found that an increased tackiness results in a smaller steering radius possibility for a given tow width, ranging from 865 mm for very tacky tows to 950 mm for no tackiness. The tackiness levels were measured based on a probe tack test, with the tackiest being a normal prepreg at 30° C.

Moreover, they investigated the influence of a range of standard tow widths and concluded it to increase more significantly the maximum curvature constraint than the tackiness effect. For a wider tow of 25.4 mm, the minimum steering radius was 1400 mm, whereas reducing the width to 12.7 mm allowed for a radius as low as 650 mm. During experimental work, Smith et al. [24] came to the same conclusion testing 1/4 and 1/8 inch tows. They believe the only disadvantage remaining in using the smaller tows is the capability of AFP machines to handle them, as smaller tows create more easily jams in the head's guides and rollers.

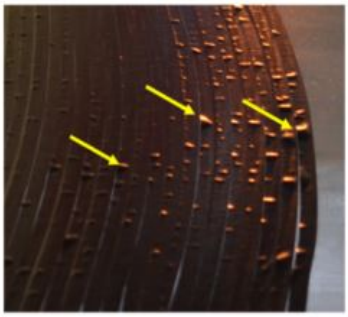

(a) Fibre puckering [5].

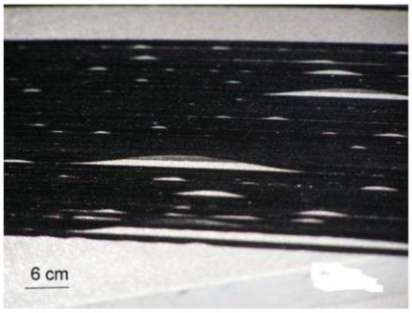

(b) Local buckling of the steered tows [23].

Figure 2.6: AFP defects.

During these experiments, it was also observed that wrinkling is a time sensitive phenomena. If the lay down process is slowed down, a tighter path with a higher curvature could be obtained [23]. To conclude, the curvature constraint is not constant, but instead depends largely on the material and manufacturing properties.

2.3.2 Continuous Tow Shearing

The second manufacturing process, proposed by Kim et al. [19], is a novel technique in its early stages, based on the shearing of the tows: Continuous Tow Shearing (CTS). The method consists in dry fibres on a resin film, which are grabbed by the machine head to be sheared into following the reference path, as is shown in Figure 2.3. Just before the deposition but after the shearing, the machine head heats up the resin to impregnate the tows in-situ. The CTS method makes use of dry fibres, as resin impregnated fibres would prove to be too viscous to handle by the machine head, hence prohibit the tow shearing mechanism.

Furthermore, CTS techniques are better at following the reference path than AFP [25] and perform a perfect shifting method. This involves following the same curvature path along the shifting direction, without the creation of gaps or overlaps, i.e. achieving perfect tessellation [19]. The advantages of CTS "*could reduce the process-induced defects such as fibre wrinkling, resin rich areas and fibre discontinuities, significantly*" [19]. However, CTS manufacturing is slower than AFP [26].

Thickness variation
During the shearing process, the tow thickness t does not remain constant. This is because conservation of volume must be satisfied, hence the thickness variation of the nominal ply thickness t_0 by the shearing angle θ follows Equation 2.9 [19]. This action is also represented in Figure 2.7.

$$t = \frac{t_0}{\sin\theta} \tag{2.9}$$

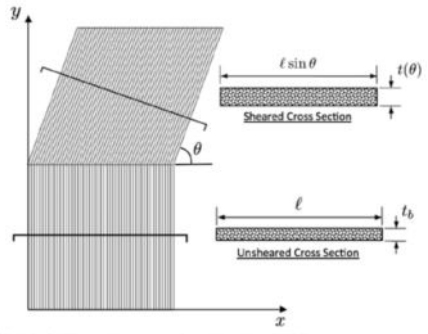

Figure 2.7: Tow thickness variation under a shear angle θ [27].

Constraints
Despite showing potential advantages, the CTS concept is still immature in productivity and reliability, especially compared to the AFP process having been used and perfected for more than 30 years [25]. Despite only having been investigated on a smaller scale, the curvature constraint in these experiments exhibited a *"minimum radius of curvature of the tow path could be decreased to less than several tens of millimetres, which was less than a tenth of that of the conventional AFP technique"* [19].

2.4 Constraint Impact

As was discussed for both manufacturing methods, the main difference lies in the maximum curvature that can be achieved. This has a direct influence on the complexity and design space of the tow paths that can be used. AFP is a more mature technology at this stage, but can be steered with a smaller curvature than CTS.

Secondly, CTS is able to match the reference path and adjacent tows more accurately. This feature is not possible with AFP, which leads to the formation of gaps or overlaps, even though the cutting and restarting capabilities can be used to lessen the effect. This difference between AFP and CTS is well shown in Figure 2.8.

However, the path matching feature is only possible *"especially when the designed tow paths are simply shifted, the CTS technique could produce a VAT composite panel with tessellated tows, i.e. without any tow drop, tow overlap, and fibre discontinuity"* [19]. In case a two dimensional steering variation is used as developed in Section 2.1.2, the latter advantage is not feasible anymore.

Moreover, when either laminates are manufactured using continuous tows with overlaps in AFP or CTS plies are stacked together, a different variable thickness profile is obtained. Local thickening effects appear in the AFP technique due to the distinct occurrence of gaps and overlap in the different

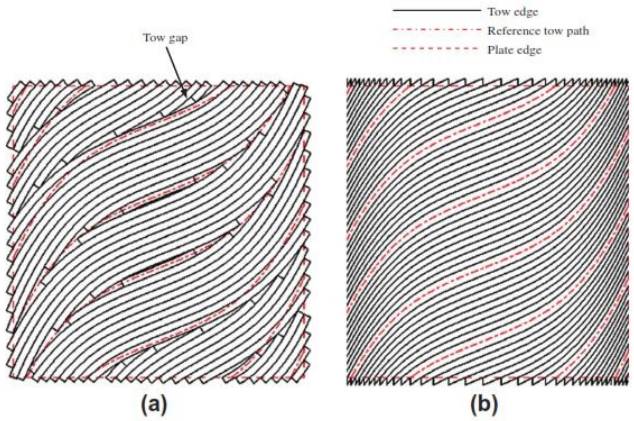

Figure 2.8: Tow placement following a reference path: a) Automated Fibre Placement b) Continuous Tow Shearing [19].

layers. On the contrary, CTS does not create gaps or overlaps, but a smoother thickness variation is obtained, since a constant volume must be kept. The two different features are shown in Figure 2.9.

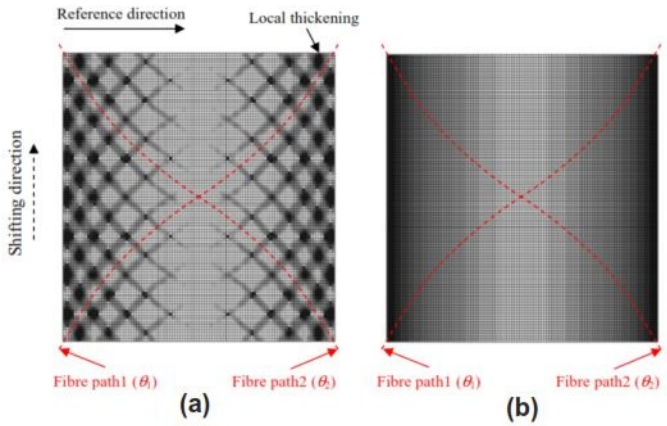

Figure 2.9: Tow steering thickness variation, darker being thicker: a) AFP, b) CTS [19].

Finally, for both thickening patterns, respective researchers believe these effects to be beneficial for structural performance [9, 19], as discussed in Section 3.4.

Chapter 3

Linear Buckling Analysis

When aerospace structures are subjected to different loading cases, they are mainly limited by buckling due to compressive loads, shear loads, or a complex loading state involving both. Allowing for a higher load carrying capability before buckling occurs is beneficial, as less material can be used for the same loading, resulting in lower mass. A typical buckling response curve of a pristine cylinder loaded in compression is shown in Figure 3.1. Two regions can be defined: a linear and non-linear one. The first part is the initial linear response, when no buckling is occurring while only end shortening is happening. Thereafter, a bifurcation point is attained, marking the buckling point and the instability of the structure. Lastly, the second non-linear part consists of the post buckling regime until failure is attained.

In case of beams, the buckling point is usually taken as the failure, since out-of-plane deflection occurs quickly afterwards, leading to fast failure. On the contrary, supported plates can sustain in-plane loads higher than the buckling load before deforming drastically and failing. This difference is shown in Figure 3.2.

The bifurcation point between the linear and non-linear part defines the linear buckling load, as explained in Section 3.1. This is opposed to the non-linear post buckling regime, which requires the use of iterative non-linear solvers, such as the Newton-Raphson or arc length based scheme [28–30].

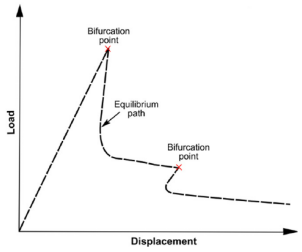

Figure 3.1: Load-displacement path for a compressed cylinder [31].

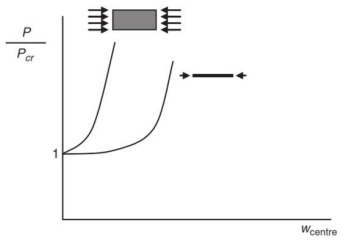

Figure 3.2: Centre out-of-plane defection versus in-plane loading for beams and plates [32].

This chapter describes different ways of calculating the buckling point. First, semi-analytical modelling for both conventional and steered fibre composite plates is discussed in Section 3.1. Thereafter, a small part is dedicated to the implementation and usage of FEM for buckling in Section 3.2. Moreover, a dedicated discussion on variable thickness consideration in modelling is done in Section 3.3. Finally, the results of simulations and experiments of linear buckling are elaborated in Section 3.4.

3.1 Semi-Analytical Modelling

Buckling is usually defined as the out-of-plane displacement when subjected to in-plane loading, but it actually represents the bifurcation point between the stable and unstable region of the structure. This is characterised by a single point of neutral stability, and can be found applying by the Neutral Equilibrium Criterion, as defined in Equation 3.1 [33]. This is the second variation of the Total Potentiality Energy (TPE) of the system Π, reducing to a linear eigenvalue problem as shown in Equation 3.2, also called linear buckling.

$$\delta^2\Pi = 0 \tag{3.1}$$

$$([K_0] - \lambda[K_{G_0}])\left\{\Phi\right\} = \left\{0\right\} \tag{3.2}$$

λ and Φ are the eigenvalues and corresponding eigenmodes, giving respectively the buckling load and shape, where the lowest λ represents the first buckling load and mode. Depending on the amount of approximation functions, the same number of modes will be solved for. $[K_0]$ and $[K_{G_0}]$ are the linear constitutive and geometric stiffness matrix of the structure, obtained from the integration of the kinematic relations substituted in the TPE formulation. These matrices depend on the selected plate theory, discussed in Section 3.1.1. In case of conventional laminates, the integration of the stiffness matrices can still be performed analytically, as done by Castro et al. [34]. However, due to the spatial variation of the ABD components in VAT laminates (see Section 2.2.1), these components must be kept within the integrand during the integration. Only for particular cases can it still be solved analytically, however the integrands become more complex with the spatial angle variation. Hence, numerical integration schemes are commonly used to capture the varying stiffness distribution, such as the Gaussian quadrature rule [8] or quasi-Monte Carlo [10].

The eigenvalue problem itself is often solved by means of the Rayleigh-Ritz method [8, 10, 35, 36], by assuming adequate shape functions to represent the displacement field. Several approximating functions are possible, as discussed in Section 3.1.3.

3.1.1 Plate Theory

To model the deformation of laminates, several plate theories have been proposed, based on different physical interpretations and mathematical simplifications of the real life mechanism. These theories consist in kinematic relations, describing the material strains undergone due to external loads for a given geometry. Afterwards, the kinematic relations are substituted in the TPE formulation to which the solution procedure is applied (e.g. Rayleigh-Ritz). Different plate theories are discussed next.

Classical Lamination Plate Theory

The Classical Lamination Plate Theory (CLPT) is based on the assumption of plane stress and the Kirchhoff hypothesis, stating that the cross section remains normal to the midplane once deformed [35]. This is a valid deformation approximation for thin laminates [10]. It is the simplest plate theory formulation and has been employed in both conventional [34, 37, 38] and VAT laminates [8, 10, 11] research. CLPT uses the ABD matrix as defined in Section 2.2.1, which is the most simplified case of a full laminate's stiffness tensor due to the assumptions of the model.

First-order Shear Deformation Theory
First-order Shear Deformation Theory (FSDT) expands CLPT by taking transverse shear effects into account. This permits the inclusion-of-trough the thickness deformation, by assuming the plate cross section not to remain normal to the midplane anymore, invalidating the plane stress condition. Indeed, this condition is not satisfied anymore, as it considers no out-of-plane strains through-the-thickness. In FSDT, the in-plane displacement are assumed to vary linearly through the thickness, however the theory requires an experimental shear stress correction factor to satisfy equilibrium [39]. It is an adequate theory suited to represent thin to moderate thick laminates [36] and has both been used to model conventional [34] and VAT [36, 40, 41] designs. As a result of the additional degrees of freedom, the FSTD stiffness tensor includes extra terms compared to the ABD matrix. In case transverse shear effects are neglected, the CLPT formulation is obtained.

Higher-order Shear Deformation Theory
To avoid shear correction factors and represent more specifically the actual transverse shear stress distribution through-the-thickness, higher-order shear deformation theories have been developed. They are more complex representations of the transverse shear effect and satisfy the equilibrium conditions. The transverse shear effects are represented by different in-plane displacement variation, such as parabolic, cubic or trigonometric. However, these representations require additional computational costs due to the extra unknowns introduced by the theory [39, 42].

3.1.2 Force Based Simulation

The solution to the eigenvalue problem, λ, is the critical load multiplier. This implies that the applied load in the analysis must be multiplied by λ to obtain the linear buckling loading. The critical load multiplier has been applied for a variety of cases, ranging from uni-axial to a combination of loading conditions. The different strategies for these situations will be elaborated next, given the generic loading definition as shown in Figure 3.3.

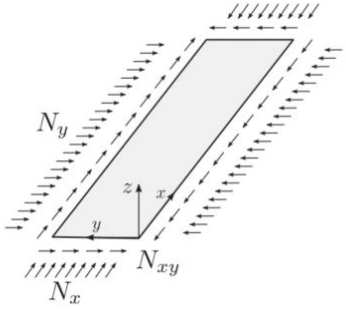

Figure 3.3: Generic plate loading conditions [37].

Guerdal et al. [8] developed a semi-analytical model for uni-axial loading N_x with boundary conditions varying between fixed, clamped or free edges independently through the selection of appropriate approximation function. Instead of compression, Raju et al. [28] applied the eigenvalue problem to in-plane shear buckling N_{xy}.

A combination of shear N_{xy} and axial N_x loading was considered by Vescovini and Bisagni [43], who included both loads in the eigenvalue problem through the TPE formulation and found the critical load multiplier. Furthermore, by incorporating a ratio between the shear and axial edge loading,

different scenarios for the linear buckling multiplier λ could be investigated. This results in knowing the overall load multiplier to be applied to both edge loads, and therefore finding the critical case of when the set of relative loads is applied. Vescovini and Bisagni extended the methodology to a biaxial and shear loading [37].

Castro et al. [34] proposed a method to find the critical buckling multiplier for several applied loadings when some are kept constant. They used the superposition principle of the initial stress state's geometric stiffness matrix of every load, but only applied the eingevalues problem to the varying loads: the geometric stiffness matrices of the constant loads remain unchanged and are added to the linear constitutive matrix. This resulted in a slightly altered formulation and a specific load multiplier λ to only be applied to all varying loads. The case of cylinder with a constant axial compression with varying torsion was presented, as well as the axial buckling of a cylinder under pressure.

3.1.3 Approximation Functions

The Rayleigh-Ritz solution method consists in using approximation functions with unknown amplitudes to replicate the out-of-plane displacement. Solving the linear buckling problem yields the unknown amplitudes, allowing the reconstruction of the displacement field.

A major requirement of possible approximation functions, is that they must satisfy the essential boundary conditions, such as clamped, fixed or free edges. Therefore the function selection is important, as it allows for the representation of boundary conditions, beside incorporating springs to represent the elastic restraints of stiffeners or other supports [34, 38].

In the analysis of conventional laminates, trigonometric functions are widely used [8, 44, 45]. In the case of plates, a double trigonometric sum is used to characterise the out-of-plane displacement depending on both x and y location. The most simple case representing all four edges as simply supported is represented in Figure 3.4 a) and mathematically in Equation 3.3. The shape function for a clamped condition is illustrated in Figure 3.4 b). The number of functions used in the double series dictates the convergence of the solution. Guerdal et al. [8] reported that more terms are needed in the direction of fibre variation than the shift direction to obtain convergence.

$$w(x,y) = \sum_{m=1}^{M} \sum_{n=1}^{N} A_{mn} \sin\left(\frac{m\pi x}{a}\right) \sin\left(\frac{n\pi y}{b}\right) \tag{3.3}$$

(a) Pinned boundary condition.

(b) Clamped boundary condition.

Figure 3.4: Approximation functions and boundary condition representation [38].

To model any boundary condition in between clamped and simply supported, as no real situation is ever neither, Vescovini and Bisagni [37] used a linear combination of both limit case of simply supported and clamped approximation functions. Mittelstedt [44] employed the same technique to represent the stiffeners' displacement field.

In case of uni axial loading, Mittelstedt [44] reduced the double sum to only one term in the axial direction with unknown half ways to describe the buckling shape. In the unloaded direction, only the odd terms of the trigonometric series were retained due to the clamped boundary condition symmetry. Furthermore, Castro et al. [34] enriched the Fourier Series' trigonometric approximation functions by axisymmetric terms to capture local phenomena.

Instead of using trigonometric function, Legendre polynomials have been adopted in the analysis of both CS [46] and VAT [10, 36, 40] laminates. This is because they "*exhibit good convergence properties in the presence of flexural anisotropy (D_{16},D_{26}) in VAT plates*" [10]. Furthermore, Rodrigues' formulation of the Legendre polynomials allows for various boundary conditions representation [47].

3.2 Finite Element Method

The use of FEM is another alternative to finding the linear buckling load. In essence, FEM solves the same eigenvalue problem of Equation 3.2, however the stiffness matrices are now composed of the individual elements' stiffness as meshed in the FEM part. Most analysis have been performed with a four node shell element (S4 in ABAQUS [48]), with four integration points [9, 10, 49]. However several methodologies have been employed to assign the stiffness property. Blom et al. [9] used a user written subroutine to evaluate and pass along the laminate stiffness at each integration point based on CPLT. On the contrary, Setoodeh et al. [12] used the average of the four nodal stiffness to assign it to the element. Oliveri et Milazzo [36] used the reduced integration S4R element, and gave each element an independent lay up, representing the local VAT, to compute the stiffness. Wu [50] used the stacking information of the centroid to construct the element's stiffness. Lastly, to investigate distinctive loading combinations, the different applied loads can be altered to attain the desired ratio and obtain distinctive critical load multiplier.

3.3 Thickness Variation Incorporation

Most literature discussed in the buckling methodology assumes uniform thickness, even in the case of steered fibre, despite taking manufacturing constraints into account. Therefore, this section is dedicated to the little research on the inclusion and simulation of the varying thickness profile due to manufacturing defects.

The thickness variation has been simulated by Wu [50] for comparison with an AFP manufactured cylinder by means of FEM. He first replicated the produced tow courses and subsequent creation of overlap location in a virtual model. This surrogate model included the stacking sequence with local orientations and ply locations for various grid points. Afterwards, the information of the closest grid point to an element's centroid was used to construct the stiffness matrix for the FEM analysis. The view of the discretised thickness used for each element is shown in Figure 3.5.

Secondly, Groh and Weaver [41] investigated the influence of the thickness profile due to CTS manufacturing by means of semi-analytical modelling. They modelled the variation both as a 2D plate and 3D shell with curvature, as shown in Figure 3.6, to assess whether the flat plate behaviour is still valid. They used a single-layer plate model with a FSDT in the 2D case. Therefore, the increased thickness regions are assumed to behave as asymmetric laminates, despite being symmetric. The asymmetric laminates were modelled according to the reduced bending stiffness approach. For the shell like modelling, it was implemented in the semi-analytical simulation with Donell's non-linear theory, and the 3D FEM verification was setup with linear brick elements.

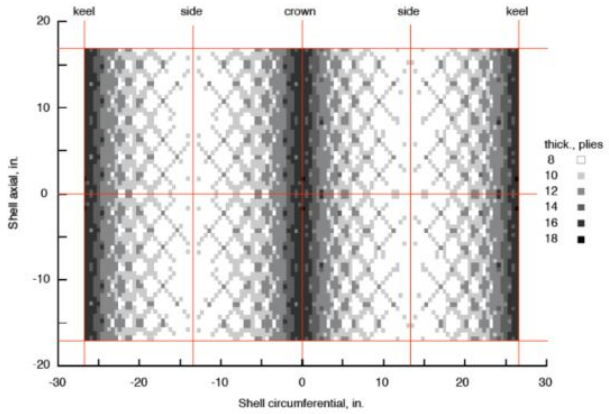

Figure 3.5: Discretised laminate thickness [50].

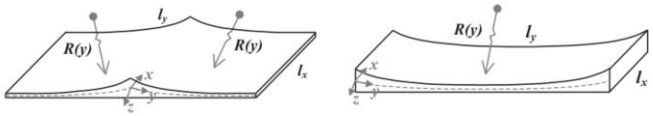

Figure 3.6: Thickness variation and modelling due to CTS [41].

Lastly, Castro et al. [51] proposed a smeared thickness formulation to approximate the local thickness of an AFP ply, as shown in Equation 3.4. It depends on the the manufacturing path angle ϕ, as defined in Figure 2.4, and t_{local} and t_{tow} are respectively the local smeared thickness and nominal tow thickness. This formulation is derived assuming the same material volume must be preserved along the shift direction together with the tow width approximation from Blom et al. [9].

$$t_{local} \approx \frac{t_{tow}}{\cos \varphi} \tag{3.4}$$

This smeared approximation is similar to the expression of the thickness variation in CTS manufacturing in Section 2.3.2, where θ is defined as 90°-ϕ. In CTS, the fibres are physically deformed to keep the same volume, resulting in the exact validity of Equation 2.9.

3.4 Results and Defects Influence

Following the different approaches on simulating linear buckling, also with the inclusion of thickness variation, the results of these numerical simulations are discussed next. Furthermore, experimental data supporting the numerical results is also reviewed. However, besides buckling, gaps and overlaps also have an effect on other structural behaviour of composites. Lozano et al. [13] gave a general overview of the influence of AFP defects on different mechanical properties, shown in Figure 3.7.

		Gap	Overlap	Half Gap/Overlap	Twisted Tow
Tension		—	—	↘	↗
Compression		—	↗	—	—
In-Plane Shear	Length	—	—	↘	↘
	Width	↗	↘	↘	↘
OHT		—	—	—	
OHC	Length	↗	↗	↗	
	Width	↘	↘	↘	

↗ ≥ 3% increase (up to 13%)
— ±3% variation
↘ ≥ 3% decrease (up to 12%)

Figure 3.7: AFP defects influence on mechanical properties [13].

3.4.1 Numerical Simulations

The semi-analytical verification with FEM of the different buckling procedures is conclusive. For conventional laminates, it has been shown that the semi-analytical methodology is in good correspondence with FEM result [34,37,38,44] as is the case for VAT designs [10,28,36,40]. Figure 3.8 shows a comparison between the first two buckling mode of a semi-analytical and FEM modelling for a VAT laminate. Moreover, the increase in approximation functions shows a rapid convergence towards a stable result, as displayed in Figure 3.9.

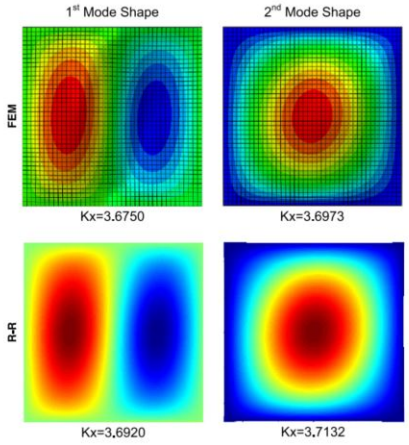

Figure 3.8: Buckling mode verification between FEM and semi-analytical modelling for VAT laminates [10].

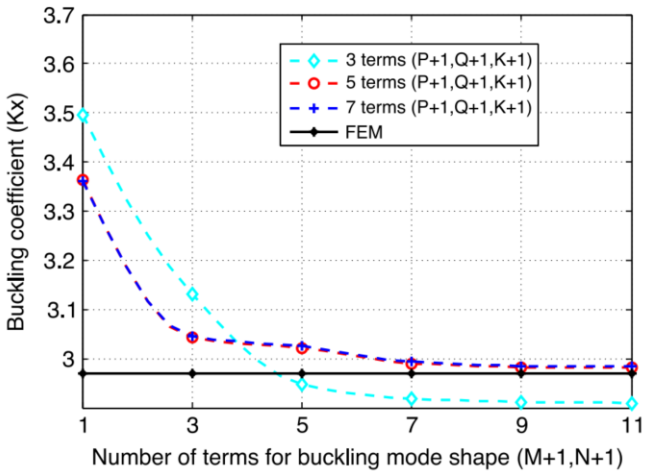

Figure 3.9: Convergence check based on the number of approximation functions [10].

Despite influencing the buckling behaviour in case of large magnitudes, Guerdal et al. [8] neglected the bending-twisting coupling in their simulations. They motivated this choice by indicating that the coupling is most extreme if successive plies are at 45° difference. However, due to the spatial variation, the positive and negative plies are often close together, only barely leading to the maximum angle difference. They did no investigate the influence further. On the contrary, Coburn et al. [40] included the bending-twisting terms for thick laminates with the FSDT modelling, and reported to be in good accordance for with FEM.

Furthermore, for almost all previous cases, the B matrix was omitted by building up the laminate in a symmetric manner. Only Groh and Weaver. [41] considered non symmetrical layups due to the offsetting, yet instead of using the stretching-bending coupling, they used the less accurate reduced stiffness and flexibility matrices for A and D. They then determined that a CTS varying thickness profile approaches better the shell like rather than plate like modelling, when compared to their 2D and 3D FEM counterpart. They also saw the possibility of using double curved thickness variation to increase buckling performance.

3.4.2 Experiments

Wu et al. [52] manufactured two shells by the AFP process, one with overlaps and the other with a more uniform thickness distribution using the cut and restart capabilities. Concurrently, they simulated the buckling characteristics of both designs in [50], as discussed in Section 3.3 for the overlap case. The testing of both cylinders allowed for the validation of the modelling procedure and show the overlap benefits. These experiments were displacement controlled, with the test data for the overlap case shown in Figure 3.10. To test if failure or defects had occurred after the load drop, a second test was performed. This showed a similar result for the end shortening, emitting the hypothesis that no damage was sustained, yet to be further investigated by the authors.

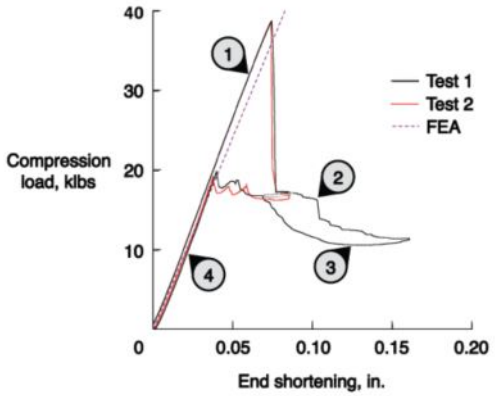

Figure 3.10: Load displacement response curve for an overlap VAT design cylinder in compression [10].

The testing revealed that in case of the overlap design, the normalised stiffness and buckling load are higher than for the uniform shell. Moreover, Wu et al. [52] suggested that VAT design do not exhibit the same sensitivity to fibre orientation than conventional laminates. This observation was also made by Blom et al. [21], stating the little influence of fibre path deviation on the results compared to the computed buckling loads in VAT composites.

Chapter 4

Research Objective and Questions

Based on this review, it is shown that the production of VAT laminates is not straightforward, due to manufacturing constraints, but has potential benefits in structural performance. Taking these requirements into account, a semi-analytical model for the buckling behaviour of varying thickness VAT laminates can be introduced.

Building upon the conclusion from the literature review, the foundation for the new research can be set up. First the research objectives are discussed, followed by the research questions. Lastly, the innovation of this research is discussed.

Research Objective

The research objective is to model linear buckling of VAT laminates by means of semi-analytical methods, considering the thickness variation due to overlaps. This can be further expanded in sub objectives: first the modelling of the tow courses in the manufacturing, and the thickness variation mapping. The mapping involves taking the tow paths to coat the complete plate, and analyse where overlaps are created. Afterwards, the second sub objective is to evaluate buckling semi-analytically.

Research Questions

In order to attain the research objective, a research question and sub questions are set up. The combined answer to each of the sub questions will result in the answer to the main research question.

The main research question is: *How to model linear buckling of VAT plates with thickness variation due to overlaps and AFP constraints by means of semi-analytical methods?* The derived sub questions are as follows:

- How do manufacturing constraints influence the overlaps?
  - What are the possible fibre paths to adhere to the manufacturing constraints?
  - What are the overlaps' locations based on the fibre paths?
- What is the influence of the overlaps on the linear buckling response?
  - How do overlaps contribute to the local stiffness matrix and coupling terms?
  - What accuracy can be achieved in representing buckling kinematics with CLPT?

- How to accurately simulate buckling of VAT laminates?
  - What is a sufficient number of integration points to represent the variable stiffness variable thickness of the laminate?
  - What is a sufficient number of shape functions to evaluate the displacement field?

Innovation

The innovation introduced by this research is to take the thickness influence into account in semi-analytical modelling for linear buckling. Moreover, as VAT laminates increase the design space by allowing the tows to vary continuously, this research sets out to obtain a method which should prove to be faster than computational FEM. Furthermore, by means of control points to define the tow path, the number of variables is drastically reduced, from thousands to only a few dozen. This whilst keeping a high complexity in the tow path possibilities and accounting for manufacturability.

The research allows to investigate further the overlap influence on the buckling behaviour of VAT laminates, but also provides a fast tool for design in preliminary stages or optimisation schemes.

Part II

Methodology

Chapter 5

Virtual Production

This thesis is focussed on the use of continuous fibres during the manufacturing process and subsequent formation of overlaps, therefore a virtual production is setup to find this relevant information. The panel's surrogate model serves to find the locations of the overlaps and layerwise thickness distribution with the corresponding fibre orientation, by virtually plotting the tows. This information is part of a pre-processing step, and can be used for either FEM or semi-analytical modelling.

This chapter starts by discussing the important parameters in defining the fibre path of VAT laminates and special consideration when overlaps are included in Section 5.1. In Section 5.2, the formation of the overlaps and tracking is explained, followed by the approximation of the discrete thickness in Section 5.3. Afterwards, the manufacturing constrains and how to meet them are discussed in Section 5.4. Finally, the mass prediction of the virtual panels is explained in Section 5.5.

5.1 Fibre Orientation

Since the main difference between CS and VAT laminates is the spatial variation of the fibres, their path definition is important. A one dimensional fibre variation will be used in this thesis, in order to setup the analysis methodology and investigate possible benefits of varying thickness and can later be extended to a two dimensional variation if proven successful. It was chosen to represent the varying fibre orientation by the Lagrange interpolation scheme suggested by Wu et al. [10] and that was discussed in Section 2.1.2. This method allows the continuous representation of the fibre orientation with a restrained number of variables, which can then be translated to fibre paths. However, the fibre angle variation can still be tailored to more complex and higher order interpolations, yet easily be checked for manufacturability.

5.1.1 Definition

Before discussing the interpolation scheme, two important coordinate systems must be introduced: the global and manufacturing one, as shown in Figure 5.1. Both coordinate systems are related to each other through the ply rotation angle χ, defined as positive clockwise from the global to the manufacturing coordinate system. The global coordinate system is used to represent the laminate and associated loading conditions, as well as the fibre orientation used to define the ABD matrix. On the contrary, the manufacturing coordinate system is linked to each individual ply which is being constructed during the virtual production process. The manufacturing coordinate system consists of the variation and shifting direction, noted x' and y' respectively.

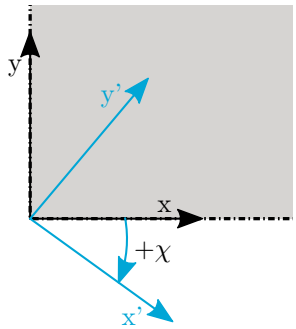

Figure 5.1: Global and manufacturing coordinate system, rotated by the angle χ.

For each ply, the one dimensional Lagrange interpolation scheme defined in Equation 5.1 is used in the manufacturing coordinate system to find the fibre orientations ϕ, also called manufacturing angles, between the Control Points (CP). These CP are located at predefined locations along the variation axis x' with an associated angle value ϕ_m, taken as positive counter-clockwise from the variation axis. Both changing the amount and values of the CP will lead to different tow paths, with different complexity.

$$\phi(x') = \sum_{m=0}^{M} \phi_m \prod_{k \neq m}^{M} \frac{x' - x'_k}{x'_m - x'_k} \tag{5.1}$$

Afterwards, the manufactured fibre orientation must be translated to the global coordinate angle θ, defined positive as counter-clockwise from the x-axis, according to Equation 5.2. The exact method and considerations to rotate a ply are treated in Section 5.1.2. As soon as one variation axis is rotated, a two dimensional thickness and fibre orientation pattern is obtained in the global coordinate system.

$$\theta(x, y) = \phi(x') - \chi \tag{5.2}$$

In order to keep track of this two dimensional information, a global laminate mesh is created in the global coordinate system. It is sampled equivalently by N_s sampling points along the length L and width W of the laminate, in the x and y direction respectively. This mesh can be remapped to the manufacturing coordinate system and be used to construct a ply, as explained in Section 5.1.2. All fibre orientations are calculated specifically at the nodal positions, irrespective of the tow path location. This assumptions is made since small tow widths are considered, in the order of the nodal spacing, and combined with the curvature constraint, which limits the change in angle over small distances, little difference will happen among tows in the direct vicinity of the mesh node. A convergence study on the required number of sampling points is carried out in the results chapter. Furthermore, this mesh will be used to keep track and represent different ply and laminate characteristics, which will be explained in the rest of this thesis. An overview of these characteristics are:

- Manufacturing angle, ϕ
- Global fibre orientation, θ
- Fibre steering curvature, ρ
- Local thickness (either discrete or smeared), t_{local}

5.1.2 Ply Rotation

Rotating a ply as suggested in literature in Section 2.1 is not applicable in case the thickness profile and fibre orientation are considered simultaneous. Both these characteristics must be judged together, as will be illustrated next. For the sake of this example, the thickness variation will be approximated by means of the smeared formulation proposed by Castro et al. [51], introduced in Section 3.3 and treated in more detail in Section 5.3. However, the same explanation also holds true for overlaps.

One can construct two different plies to obtain the same global fibre orientation, according to the characteristics given in Table 5.1. However, the thickness profile is different for both cases, as it is only related to the manufacturing angle. Until now, literature only assumed uniform thickness fibres at any location, hence the rotation angle χ could simply be added afterwards, as it does not influence the manufacturing process and the simulated laminate can still be obtained. However, by means of this example, it is clear that for overlap creations, the rotation angle must be judged concurrently with the manufacturing angles. It cannot be simply added afterwards since this will result in different spatial and thickness locations.

Table 5.1: Different thickness profile for the same global fibre orientation.

		CP 1		CP 2		CP 3	
	χ [°]	ϕ_1 [°]	Thickness ratio [-]	ϕ_2 [°]	Thickness ratio [-]	ϕ_3 [°]	Thickness ratio [-]
Case 1	0	0	1	-45	$\sqrt{2}$	0	1
Case 2	-45	45	$\sqrt{2}$	0	1	45	$\sqrt{2}$

When considering the production process, the complete plate is rotated and encompassed in a bigger rectangular domain representing the manufacturing area, as shown by the dotted blue line in Figure 5.2. This manufacturing area can be viewed as a big plate where tows, such as in Figure 5.5, are being deposited next to each other by the machine head to fully cover the black dotted plate domain.

In order to obtain the manufacturing angles, the global laminate mesh is remapped to the manufacturing coordinate system by means of Equation 5.3, which can then be used in the interpolation of Equation 5.1. The new x' still serves as location for the interpolation, however, the y' part is also important in order to know the exact overlap location, as there could only be partial overlapping depending on the manufacturing angle, as explained in Section 5.2.

$$\begin{Bmatrix} x' \\ y' \end{Bmatrix} = \begin{bmatrix} \cos(-\chi) & \sin(-\chi) \\ -\sin(-\chi) & \cos(-\chi) \end{bmatrix} \begin{Bmatrix} x \\ y \end{Bmatrix} \tag{5.3}$$

Secondly, the Lagrange interpolation scheme only works with regular CP located along the variation axis. Therefore, it was decided to define the CP locations as percentages, in such a way that for the a rotated manufacturing domain, they are repositioned relative to the largest distance along the variation axis.This has no influence on possible variation outcome, as the degree of interpolation is maintained and by selecting a different set of CP values, the same distribution of orientations can be obtained. Finally, a positive ply rotation yields a varying manufacturing angle pattern from the top left corner to the bottom right one, the opposite holding true for a negative rotation. Remapping the CP in this way allows the extreme locations still to be associated to a CP value, as they represent the longest distance.

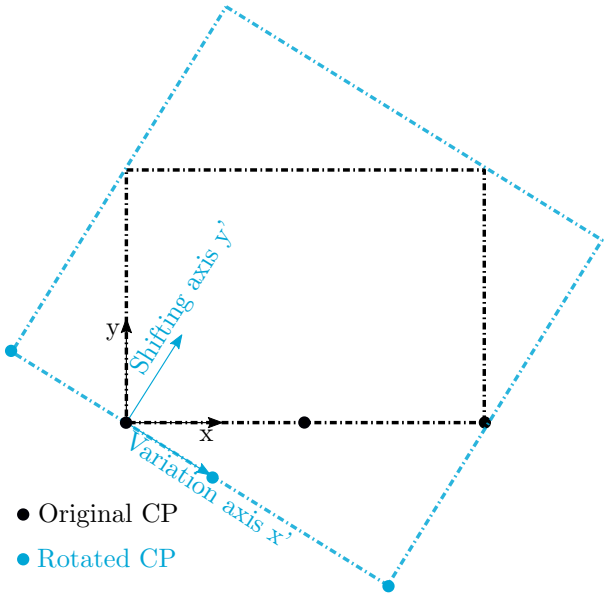

Figure 5.2: Plate and rotated manufacturing, with associated Control Points rotation.

The ply rotation can serve two purposes, either increasing the thickness for a given global fibre orientation, or to achieve a global orientation not possible due to the constraint on the manufacturing angles, discussed later, or a combination of both.

This rotation strategy, and subsequent steps in this methodology, are demonstrated on an example of a virtual manufactured ply whose characteristics are given in Table 5.2. In Figure 5.3, the fibre orientation is shown in the manufacturing coordinate system, with the plate rotated. When the plate is viewed in its original global coordinate system, then interpolation pattern shown in Figure 5.4 is obtained, where the ply rotation χ has also been applied. It is clear that the CP value of $-45°$ and $45°$ are still obtained at the top left and bottom right corners.

Table 5.2: Virtual manufacturing example characteristics.

Variable	Value	
Length	50	[mm]
Width	50	[mm]
χ	30	[°]
ϕ_1 at 0%	-30	[°]
ϕ_2 at 30%	15	[°]
ϕ_3 at 60%	65	[°]
ϕ_4 at 100%	-50	[°]

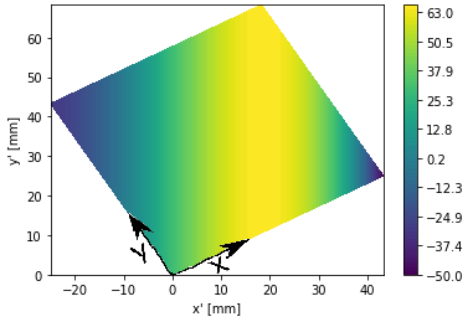

Figure 5.3: Virtual manufacturing example interpolated fibre orientation ϕ in the manufacturing coordinate system.

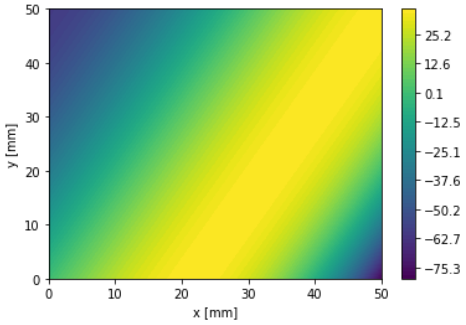

Figure 5.4: Virtual manufacturing example interpolated and rotated fibre orientation θ in the global coordinate system.

5.2 Overlap Location

In order to obtain the discrete thickness profile of VAT laminates, the overlap locations must be tracked as the tows are being deposited. Thereafter, the local thickness t_{local} for a given location can be constructed by simply adding all the plies and their overlaps.

To do so, first the tow paths are determined, followed by graphically representing them with a given opacity for a full ply. The opaque tows can be superimposed and in doing so result in a distinct opacity levels, which can finally be related to discrete thicknesses. This methodology is applied per ply individually, in order to better identify the overlaps, as the distinction becomes less and less accurate with a higher number of overlaps. Furthermore, it does not restrain the total amount of ply for a laminate.

5.2.1 Tow Path

Subsequent to the interpolation of Equation 5.1, the fibre orientation can be translated to tow paths in the manufacturing coordinate system for a given ply. The relation between the manufacturing angle and tow path, given by Equation 5.4 [9], can be integrated by steps as shown in Equation 5.5 to obtain the spatial location of a singular tow path in the x'y' plane. The step size $\Delta x'$ is defined by the length of the encompassed manufacturing domain along the x'axis divided by the (N_s-1). The tow can afterwards be copied in the shifting direction in order to obtain tows covering the complete plate. To this end, it is assumed that for any ply a manufacturing angle of 0° will always be reached, hence to be sure the complete plate is covered and no gaps are presents, the tow shift must be equal to the tow width. The tow path of the virtual manufacturing example is shown in Figure 5.5.

$$\frac{dy'}{dx'} = \tan\phi \tag{5.4}$$

$$\Delta y' = \tan(\phi(x'))\Delta x' \tag{5.5}$$

The path of one tow for the virtual manufacturing example is reconstructed in Figure 5.5 from the interpolated manufacturing angles.

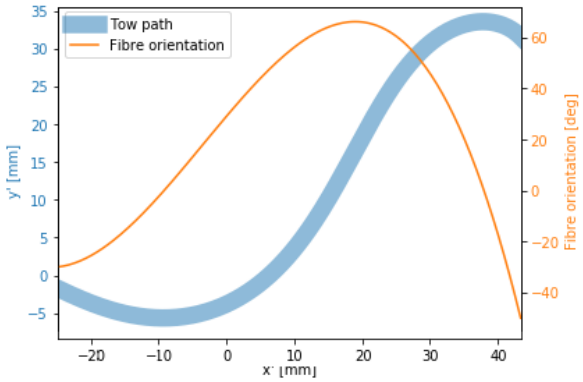

Figure 5.5: Virtual manufacturing example interpolated fibre orientation with corresponding tow path.

5.2.2 Graphical Fibre Representation

To graphically represent the tow paths, the matplotlib library [53] of Python is used. This package provides the possibility to draw graph lines with a certain opacity and width matched to the actual tow width w. In first instance, it is checked whether matplotlib accurately simulates the effective tow w_e width compared to the analytical expression given in Equation 5.6 [9], by using straight lines under an angle. To obtain the graphical width, the number of pixels are counted and transformed to the effective width through the dpi setting. The result of this analysis is displayed in Figure 5.6, showing good agreement between both methods.

$$w_e = \frac{w}{\cos \phi} \tag{5.6}$$

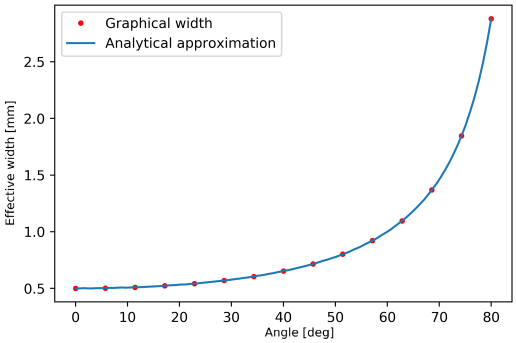

Figure 5.6: Comparison between the analytical and graphical effective width.

With the tools to plot the tow path, the virtual manufacturing can be carried out. Then, according to Equation 5.6 with ϕ equal to 0°, the effective width equals the tow width, and the tows will be adjacent to each other, not creating overlaps. However, as soon as $|\phi|$ becomes greater, then the increased effective width result in partial overlaps. The limit case of a single full overlap happens when each tow is completely covered by respectively the top and bottom half of the previous and subsequent tow. Hence, each tow must effectively be twice as wide to account for these halves to cover up other tows.

Equation 5.7 shows the derivation of the associated manufacturing angle for one full overlap. Furthermore, when $|\phi|$ is further increased beyond 60°, then locations of multiple overlap are created. The manufacturing angles and subsequent overlap formations are shown in Figure 5.7, with more opaque regions representing more thickness and overlaps. Equivalently, Table 5.3 gives the effective tow width ratio to obtain at least a certain amount of overlaps, and the associated manufacturing angle. The total local thickness can be obtained by means of Equation 5.8, meaning the lowest nominal tow thickness is obtained where no overlaps are present, and increases as an integer multiplication for each overlap present.

$$w_e = 2w \approx \frac{w}{\cos\phi} \implies |\phi| \approx 60° \tag{5.7}$$

$$t_{local} = (N_{overlaps} + 1)t_{tow} \tag{5.8}$$

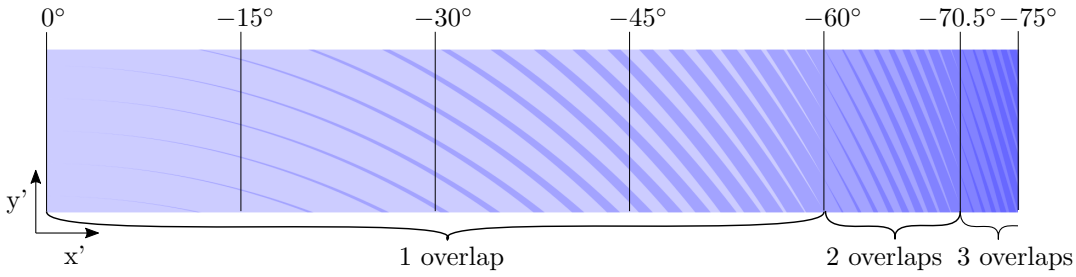

Figure 5.7: Overlap formation depending on the manufacturing angle ϕ.

Table 5.3: Amount of (partial) overlap depending on the manufacturing angle ϕ.

Amount of (partial) overlap(s) [-]	Tow width ratio [-]	$\|\phi\|$ [°]
1	2	60.0
2	3	70.5
3	4	75.5
4	5	78.5
5	6	80.4

5.2.3 Repeat Unit

Once the virtual tows have been drawn graphically, the information must be translated to actual amount of overlaps. Therefore, the first step is to only retain a snippset of the ply along its complete x' distance, defined by the most outward CP locations, by using a repeat unit concept. Since the tow pattern is self repeating along the shifting direction, only a fraction needs to be used in that direction, allowing for better memory management. This permits the use of a higher resolution to differentiate the overlaps. Also, only the plotting within that repeat unit must be accurate. A ply information area is plotted for a y' width of 5 times the tow width, but only the central part equalling one tow width is used as repeat unit and to calculate the overlaps. By subtracting the lowest integer amount of tow width to a given y' location, it can be repositioned within this part combined with the x' location, a specific pixel with a given opacity is obtained to determine the amount of overlap. How the opacity value is applied and converted to overlaps is explained in Section 5.2.4. The repeat unit for the virtual manufacturing example is shown in Figure 5.8.

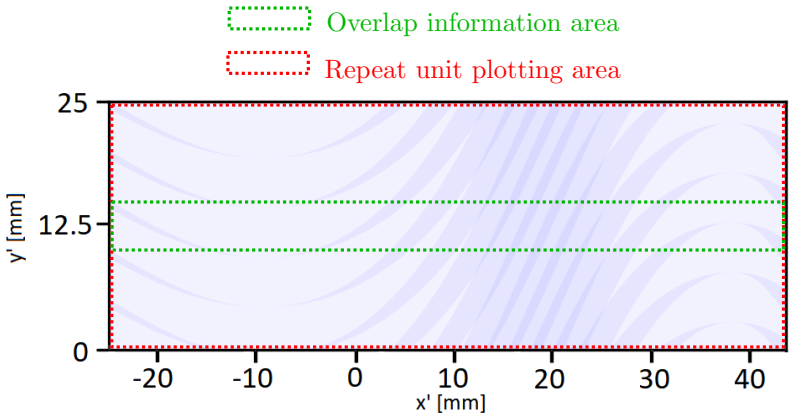

Figure 5.8: Repeat unit definition for the virtual manufacturing example of Table 5.2.

As the laminate mesh was only remapped to the manufacturing coordinate system to have the correct x' and y' components to construct the interpolation and subsequent overlap formation, these informations can be stored for the same entry in the global mesh than for the manufacturing one. Where there are overlaps, the ply thickness according to Equation 5.8 is stored, along the same fibre orientation of that mesh point.

5.2.4 Opacity Tracking

When virtually plotting the tows, each line is given a constant opacity value on the α channel, storing the opacity information in a figure. This value can be selected in the range of 0 to 1 and dictates the opacity of the plot, with lower values being more transparent. A value of 0.05 was selected in order to have a sizeable difference to distinguish up to 10 overlaps on the α channel, whilst not reaching a plateau. The α channel is also coded on the standard 8 bits scale, hence it is not infinite and higher amounts of overlap will converge on the α channel value. This is also the main reason to use the opacity tracking method on a ply basis, where the number of overlaps remains low (two to three), instead on the full laminate. If it were applied on an eight ply laminate with just one overlap, it could possibly lead up to 16 superimposed tows, where the α values have already reached the plateau and becomes hard to distinguish. Decreasing the α value would not help, as even few overlaps would then become difficult to differentiate. Therefore, the overlap tracking by means of opacity is applied on a ply basis, allowing for an infinite amount of plies to be included in the laminate.

When the repeat unit is extracted, the α values of the image can be retrieved in order to determine the amount of overlaps. By testing on a known configuration beforehand (in this case straight lines crossing each other), a scale of threshold values can be set to distinguish the amount of overlaps. An overview of the thresholds up to two overlaps is shown in Table 5.4.

The thresholds were set in order to also include transition α values due to aliasing. These thresholds are fixed, but the overlap contours can be further tuned by the resolution setting. In the current work, it is permitted to use a very high resolution to obtain a converged discrete model, as it serves primordially as a comparison to the smeared case. This latter approximation of the thickness has no influence of the resolution, as it depends solely on the manufacturing angle. Moreover, changing the number of sampling points will have a greater effect on the nodal shift and subsequent acquired

Table 5.4: α thresholds to distinguish the amount of local overlap.

Lower α value [-]	Upper α value [-]	Number of tows [-]	Number of overlaps [-]
6.5	19	1	0
19	30.5	2	1
30.5	41.5	3	2

information. Hence both these parameters' influence is evaluated simultaneous during the validation and convergence of the models.

Continuing with the repeat unit of Figure 5.8, the obtained discrete thickness pattern of the virtual manufacturing example is shown in Figure 5.9 and 5.10. Finally, the overlap and thickness pattern can be used as a first verification step to compare the smeared and discrete laminate thickness, as will be discussed in Section 8.4.

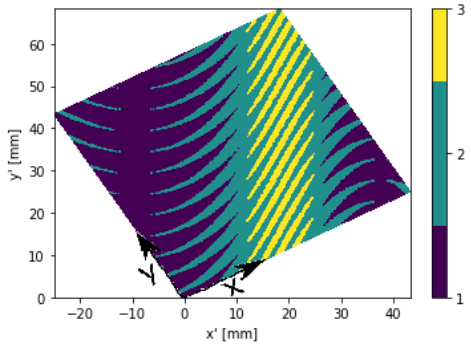

Figure 5.9: Amount of tows in the manufacturing coordinate system for the virtual manufacturing example, showing the overlap locations.

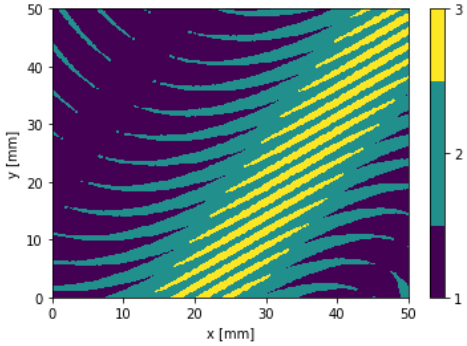

Figure 5.10: Amount of tows in the global coordinate system for the virtual manufacturing example, showing the overlap locations.

5.3 Smeared Thickness

As was presented in Section 3.3, Castro et al. [51] suggested a local thickness t_{local} approximation based on the manufacturing angle ϕ, given again in Equation 5.9. This approximation will be used as an attempt to represent the buckling of continuous AFP laminates with discrete overlaps. This formulation will be referred as smeared thickness for the further part of this thesis, as it distributes the change of thickness in a continuous manner for each ply.

$$t_{local} = \frac{t_{tow}}{\cos \phi} \tag{5.9}$$

Analysing the approximation, it is only valid for $|\phi| < 90°$, as firstly manufacturing angles $> 90°$ will yield a negative thickness which is physically not possible. Furthermore that would coincide with a tow path curling back on itself, which is prohibited, as then tows would never cover the entire laminate.

Secondly, as $|\phi|$ approaches 90°, the smeared thickness of a nominal tow tends to infinite as shown in Figure 5.11. Although when compared to reality in case ϕ equals 90°, all tows will indeed overlap and create a major build-up, equalling the thickness as given in Equation 5.8, however it is neither desired nor will it result in infinite thickness. The approximation is restricted to $|\phi| <= 60°$ alongside considerations discussed in Section 6.1.2, and this corresponds to an increase of 3% in local thickness for one degree increment of the manufacturing angle, as shown in Figure 5.12. The smeared thickness distribution of the virtual manufacturing example is shown in Figure 5.13 and 5.14.

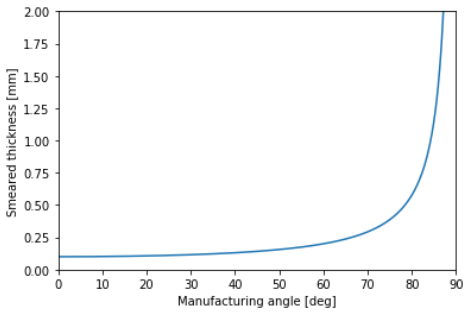

Figure 5.11: Local tow thickness approximation based on Equation 5.9.

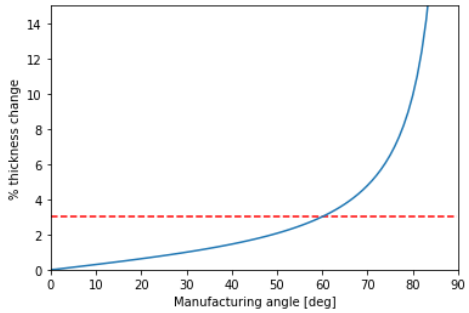

Figure 5.12: Relative local thickness increase for one degree increment of the manufacturing angle.

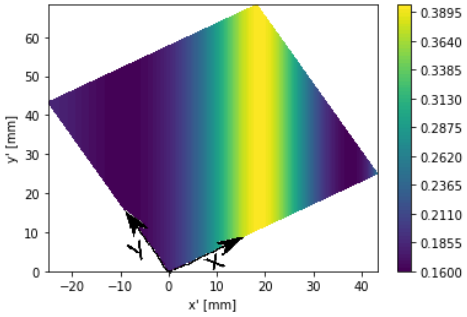

Figure 5.13: Smeared thickness distribution in the manufacturing coordinate system for the virtual manufacturing example.

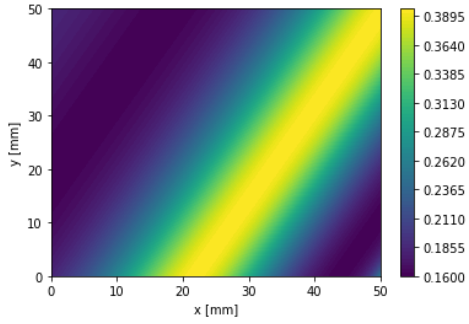

Figure 5.14: Smeared thickness distribution in the global coordinate system for the virtual manufacturing example.

5.4 Manufacturing Constraints

The manufacturing process of AFP VAT laminates is mostly constrained by the steering while depositing fibres. In order to achieve feasible tow paths, their curvature ρ must be lower than 1.575 $1/m$, as discussed in Section 2.3.1. To check this constraint, the radius of curvature of a tow path can be calculated from the interpolation. The radius of curvature r_s of a generic function can be obtained by means of Equation 5.10 [54], which is related to the curvature through $\rho = 1/r_s$.

$$r_s = \frac{\left[1 + \left(\frac{dy}{dx}\right)^2\right]^{\frac{3}{2}}}{|\frac{d^2y}{dx^2}|} \tag{5.10}$$

Applying this expression in the manufacturing coordinate system, the first derivative of the fibre path is the tangent of the fibre orientation as shown in Equation 5.4 and can be obtained straightforward from the initial interpolation, as was elaborated in Section 5.1.1. Deriving Equation 5.4 again with respect to x', the expression shown in Equation 5.11 is obtained for the second derivative.

$$\frac{d^2y'}{dx'^2} = \frac{1}{cos^2(\theta)} \frac{d\phi}{dx'} \tag{5.11}$$

The derivative of the manufacturing angle ϕ can be constructed in a closed form from the mathematical interpolation of Equation 5.1, leading to the expression given in Equation 5.12.

$$\frac{d\phi}{dx'} = \sum_{m=0}^{M} \phi_m \sum_{i=0, i\neq j}^{M} \left[\frac{1}{x_j - x_i} \prod_{m=0, m\neq(i,j)}^{M} \frac{x - x_m}{x_j - x_m} \right] \tag{5.12}$$

The curvature constraint is evaluated for every ply at each point in the laminate mesh, remapped to the manufacturing coordinate system. The fibre variation and steering happens in this coordinate system, and is simply rotated when viewed in the global coordinate system: the rotation does not alter the manufacturing constraints. As soon as any mesh location does not satisfy the curvature limit, then that particular ply can not be manufactured and a different set of CP values or locations has to be selected.

5.5 Panel Mass

In order to effectively compare several panel options, normalising or designing at isomass is common practise. To compute the mass of a uniform thickness panel is straightforward, being the plate area times the number of plies N_{ply} times the nominal tow thickness t_{tow} times the material density ρ_{mat} ($m_{uniform} = \rho_{mat} tLW$). However, an approximation is used with a varying thickness profile, as displayed in Equation 5.13.

$$m = \rho_{mat} A \sum_{i=0}^{N_s-1} \sum_{j=0}^{N_s-1} t_{avg_{ij}} \tag{5.13}$$

This approximation is a two dimensional extension of the integral rule, where the panel is divided in equal element of area A. This area is defined by the laminate mesh, constructed by means of the sampling points N_s along the edges. Since the sampling is always equidistant along the edges, the area is equal for each of the thickness contribution. t_{avg} is taken as the average thickness of the 4 nodes making up the ij^{th} area. In Section 8.3, a convergence study of the amount of sampling points on the panel's mass is performed.

Chapter 6

Linear Buckling Analysis

With the virtually manufactured laminate established, its linear buckling response can be computed, with special considerations to be taken into account due to the varying thickness profile. Section 6.1 deals with the complete derivation of the semi-analytical linear buckling model, followed by the methodology to construct a FEM model for verification purposes in Section 6.2. Finally, an overview of the complete procedure involving virtual manufacturing to obtain the linear buckling results is presented in Section 6.3.

6.1 Semi-Analytical Model

This section is dedicated to the derivation of the semi-analytical model for linear buckling of a composite laminate, represented in Figure 6.1. Firstly, Section 6.1.1 explains the change to the natural coordinate system, followed by a discussion on the appropriate displacement formulation for the one-sided thickness build-up in Section 6.1.2. Based on this, the displacement fields are derived mathematically in Section 6.1.3 and afterwards the shape functions to solve for the unknown displacements are presented in Section 6.1.4. Thereafter, the eigenvalue problem resulting from the neutral equilibrium is set up in Section 6.1.6 and finally, the static analysis to obtain the stress resultants is explained in Section 6.1.7.

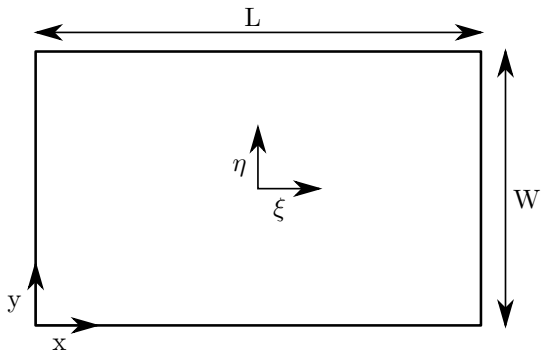

Figure 6.1: Laminate geometry and coordinate system representation.

This complete derivation and methodology was already implemented in the panels package [55] for Python, which has been adapted to incorporate the one-sided thickness build-up and variable thickness into the linear buckling analysis.

6.1.1 Natural Coordinates

In order to express all the structural matrices in a suitable form for numerical integration, natural coordinates are used. They allow to transform any plate of length L and width W to a uniform square, with bounds of $[-1, 1]$, by means of the mathematical transformation given in Equation 6.1. The natural coordinate system is provided in Figure 6.1.

$$\begin{aligned} \xi &= \frac{2x}{L} - 1 \\ \eta &= \frac{2y}{W} - 1 \end{aligned} \tag{6.1}$$

The change of coordinate system and variables must be accounted for in the subsequent integrals of the buckling analysis, by means of the Jacobian given in Equation 6.2, with $dxdy = \det J d\xi d\eta$.

$$J = \begin{bmatrix} \frac{\partial \xi}{\partial x} & \frac{\partial \eta}{\partial x} \\ \frac{\partial \xi}{\partial y} & \frac{\partial \eta}{\partial y} \end{bmatrix} \tag{6.2}$$

Furthermore, following the chain rule as shown in Equation 6.3, the derivatives must also be adjusted in the subsequent definitions.

$$\frac{\partial u}{\partial x} = \frac{\partial u}{\partial \xi} \frac{\partial \xi}{\partial x} \tag{6.3}$$

6.1.2 ABD Matrix

In accordance with VAT laminate characterisation as performed in literature, the current VAT laminate will be simulated on a mesoscale, by means of the ABD matrix, whose generic formulation is given in Equation 6.4. Q_{ij} is the rotated stiffness matrix due to the fibre orientation θ in the global coordinate system as defined in Section 5.1.1. The derivation and formulation of the rotated stiffness Q_{ij} is available in Appendix A. z defines the the position of the ply through-the-thickness, where z_{k-1} is the distance between the bottom of the laminate and the bottom of the ply, and z_k the distance between the bottom of the laminate and the top of the ply, hence the actual ply thickness is $z_k - z_{k-1}$. In this thesis, the varying thickness profile is simplified per ply: in case of overlaps, each ply thickness $z_k - z_{k-1}$ is given by Equation 5.8 and in case of the smeared approach, the ply thickness is given by Equation 5.9.

$$[A_{ij}, B_{ij}, D_{ij}] = \sum_{k=1}^{n} Q_{ij} \left[(z_k - z_{k-1}), \frac{\left(z_k^2 - z_{k-1}^2\right)}{2}, \frac{\left(z_k^3 - z_{k-1}^3\right)}{3} \right] \tag{6.4}$$

When Equation 6.4 is applied locally, the midplane of the layup is used. However, due to the manufacturing techniques for VAT laminates, the cross section is not symmetric. Indeed, when each ply is being deposited, it is done so on a flat piece of equipment, resulting in the bottom face being completely flat as well. Hence the overlap and thickness build-up is only created on the top side, as shown in Figure 6.2. This involves that the geometrical midplane also varies throughout the laminate. Two options are available to model this variation: either using a shell formulation including this varying midplane, or adapt the ABD formulation by including an offset to a common plane along which the forces and moment are assumed to act. This second approach does however not consider the proper strain kinematics due to the shell curvature.

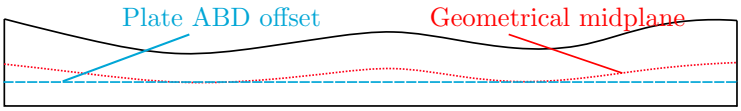

Figure 6.2: Geometrical midplane versus plate ABD offset definition.

An alternative yet very inefficient and expensive way to counter this phenomenon, is to produce a symmetric laminate by using a negative mould. This mould would contain the mirrored shaped of the overlaps, obtained beforehand, and would then be specific to one laminate. Moreover, this would also be an inconvenient if one-side is expected to be flat when i.e. aerodynamic considerations are important.

Groh and Weaver [41] investigated and compared the ABD offset and shell formulations with a detailed 3D FEM model for buckling of varying thickness CTS laminate. Their findings are displayed in Figure 6.3. Both the shell and offset formulation were tested with a semi-analytical model (noted DQ) and FEM implementation, and then compared to a detailed 3D FEM.

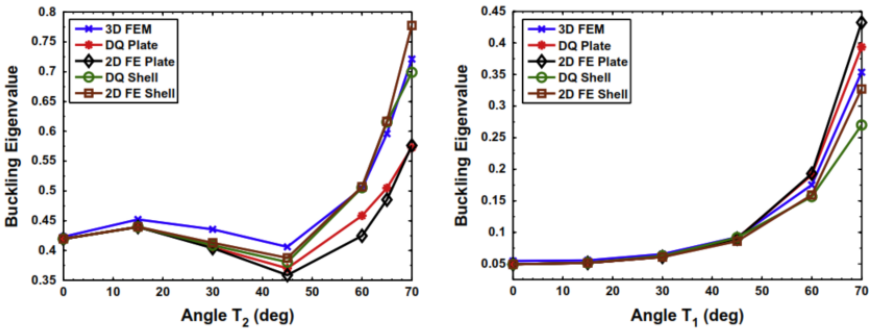

(a) Case B1: λ_{cr} vs. T_2 for a $[90 \pm < 0 | T_2 >]_s$ laminate

(b) Case B1: λ_{cr} vs. T_1 for a $[0 \pm < T_1 | 0 >]_s$ laminate

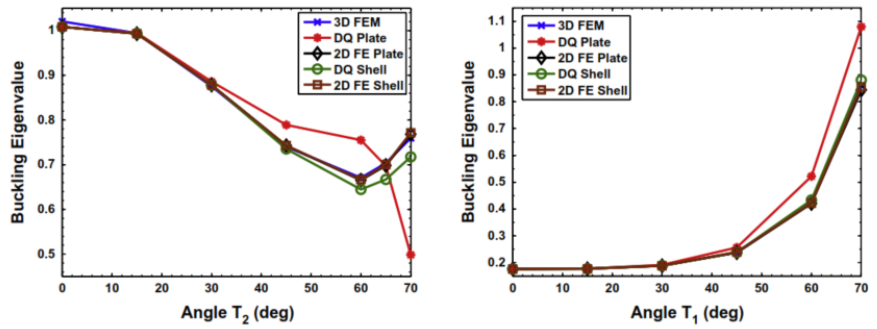

(c) Case B2: λ_{cr} vs. T_2 for a $[90 \pm < 0 | T_2 >]_s$ laminate

(d) Case B2: λ_{cr} vs. T_1 for a $[0 \pm < T_1 | 0 >]_s$ laminate

Figure 6.3: Plate, shell and 3D buckling formulation comparison for variable thickness CTS laminates [41].

All the results show similar trends and are mostly in accordance with the 3D case, except the red DQ plate. This can be explained by the reduced bending stiffness approach used by Groh and Weaver [41] to simulate the influence of the B matrix in the semi-analytical formulation, however can be off by up to 30% [56]. Nonetheless, the plate formulation is adopted in this thesis, but it is expected

that the current developed formulation to coincide with the FEM model, as the subsequent derivation takes all coupling effects into account. This is corroborated by the first verification results of the semi-analytical model with FEM in Chapter 9 for random stacking sequences, allowing to evaluate buckling with the plate FEM trend in Figure 6.3.

For case (a) only, even the FEM plate model does not coincide with the 3D FEM, yet only for angles greater than 45° and it under predicts the eigenvalue. This would result in a more conservative calculation, and can be accepted for the purpose of this thesis, which is an initial semi-analytical model investigating the possible benefits of overlaps. However, when looking at case (b) the comparison between the plate FEM and 3D FEM is good until 60°, after which the plate over-predicts buckling and this is not desired. Therefore it is assumed that using a manufacturing fibre orientation of $|\phi| <= 60°$, a plate formulation that does not consider the effect of curvature on the strain kinematics can still be used to represent the linear buckling characteristics of variable thickness VAT laminates.

6.1.3 Displacement Field

Following the discussion on the kinematic modelling in the previous section, a plate formulation will be used, more precisely the Kirchhoff-Love plate theory. The assumptions of this theory state that the cross section remains normal to the midplane during the out-of-plane deformation, and no thickness change is present: it neglects the out-of-plane shear influence on the laminate. These assumptions are valid for much larger in plane dimensions than the out of plane ones, under which the current model will function. The laminate's dimensions are in the region of meters as not to be constrained by the steering curvature, compared to the laminate's thickness of several millimetres.

The plate's displacement can be characterized by a combination of three components, being $u, v, w.$ respectively the displacements in x, y and z direction. u and v are the in plane displacement, while the out-of-plane displacement with Kirchhoff-Love assumptions is shown in Figure 6.4 in the xz plane. All three displacement components are a function of the two dimensional planar coordinates x and y. The in plane displacement for any location on the cross section can be expressed as a combination of stretching u^0 and bending u_{bend} in the x direction, as shown in Equation 6.5, and analogously v^0 and v_{bend} in the y direction.

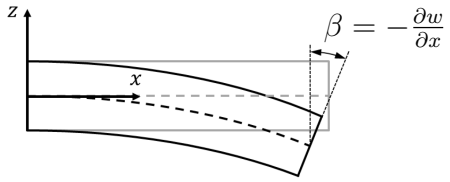

Figure 6.4: Kirchhoff-Love plate out-of-plane displacement, adapted from [33].

$$u = u^0 + u_{bend} \tag{6.5}$$

The bending contribution can be express as shown in Equation 6.6 for small angles, according to the coordinate system and graphical representation given in Figure 6.4. The rotation β is equivalent to the slope of the deflection.

$$u_{bend} = z\beta = -z\frac{\partial w(x,y)}{\partial x} \tag{6.6}$$

Therefore the in-plane displacement u can be characterised by Equation 6.7, and in an analogous manner for v in the y direction.

$$u = u^0 - z\frac{\partial w(x,y)}{\partial x} \tag{6.7}$$

6.1.4 Approximation Functions

The unknown displacement fields u, v and w are solved by means of the Ritz method. This involves approximating the displacements by a summation of shape functions g with associated unknown amplitude c, as shown in Equation 6.8 for u. Let $\{u_p\}^T = \{u, v, w\}$ be the displacement vector, the approximation can then be written in matrix form as $\{u_p\} = [g]\{c\}$, as shown in Equation 6.9, where S_u contains all the shape functions only relevant for the displacements in the x direction, and analogously S_v and S_w for the y and z direction.

$$u = \sum_{i=1}^{n} c_{u_i} g_{u_i} \tag{6.8}$$

$$\begin{Bmatrix} u \\ v \\ w \end{Bmatrix} = \begin{bmatrix} g_{u_1} & 0 & 0 & g_{u_2} & 0 & 0 & \cdots & g_{u_n} & 0 & 0 \\ 0 & g_{v_1} & 0 & 0 & g_{v_2} & 0 & \cdots & 0 & g_{v_n} & 0 \\ 0 & 0 & g_{w_1} & 0 & 0 & g_{w_2} & \cdots & 0 & 0 & g_{w_n} \end{bmatrix} \begin{Bmatrix} c_{u_1} \\ c_{v_1} \\ c_{w_1} \\ \vdots \\ c_{u_n} \\ c_{v_n} \\ c_{w_n} \end{Bmatrix} = \begin{bmatrix} S_u \\ S_v \\ S_w \end{bmatrix} \begin{Bmatrix} c_{u_1} \\ c_{v_1} \\ c_{w_1} \\ \vdots \\ c_{u_n} \\ c_{v_n} \\ c_{w_n} \end{Bmatrix} \tag{6.9}$$

The approximation functions used in this thesis are a form of Legendre hierarchic orthogonal polynomials, derived by Rodrigues [57], and expressed in the natural coordinate system. First of all, literature has proven Legendre polynomials to be fit to represent VAT laminates as discussed in Section 3.1.3. Furthermore, Rodrigues' polynomials already have the different out-of-plane boundary conditions incorporated into them, as will be explained next. In order to include the in-plane boundary conditions and achieve the solution completeness, the shape functions for u and v are enriched. The general Legendre polynomial definition is given in Equation 6.10, which is only used from the 5^{th} term onwards for all u, v and w, and where the integer division is used to express !q = q(q-2)...(2 or 1)0!! = 1 and i/2.

$$S_{i=4}(\xi \text{ or } \eta) = \sum_{p=0}^{i/2} \frac{(-1)^p (2i-2p-7)!!}{2^p p!(i-2p-1)!} \xi^{(i-2p-1)} \tag{6.10}$$

The enrichment for both in-plane displacements consists of two linear function, given in Equation 6.11. Beside providing completeness, these yield a non zero value at respective ξ or η = -1 and ξ or $\eta = 1$, enabling the translation of the edges. By the inclusion of flags, they allow to enable (flag = 1) or prohibit (flag = 0) a specific shape function, related to a displacement mode and associated boundary condition [47].

$$\begin{aligned} u_1(\xi) \text{ or } v_1(\eta) &= \left(\frac{-(\xi+1)}{2} + 1\right) flag_1 \\ u_2(\xi) \text{ or } v_2(\eta) &= \left(\frac{(\xi+1)}{2}\right) flag_2 \end{aligned} \tag{6.11}$$

The characterisation of the out-of-plane displacement is completed with the four first terms of Rodrigues' form of Legendre polynomials shown in Equation 6.12. The first two terms represent respectively a free and simply supported boundary conditions at ξ or $\eta = -1$, and equivalently for last two at ξ or $\eta = 1$. The free boundary condition shape functions give a non zero displacement at the respective end, yet a null rotation. On the contrary, the simply supported boundary condition case allows for a non zero rotation at that given edge, but no translation. All higher order terms given by Equation 6.10 always yield a zero rotation and displacement at both ends. A graphical representation of the first 10 terms of the polynomial is given in [58]. Again, the flag system is used to disable or enable a boundary condition.

$$\begin{aligned} S_{i=1}(\xi \text{ or } \eta) &= \left(\frac{1}{2} - \frac{3}{4}\xi + \frac{1}{4}\xi^3\right) flag_3 \\ S_{i=2}(\xi \text{ or } \eta) &= \left(\frac{1}{8} - \frac{1}{8}\xi - \frac{1}{8}\xi^2 + \frac{1}{8}\xi^3\right) flag_4 \\ S_{i=3}(\xi \text{ or } \eta) &= \left(\frac{1}{2} + \frac{3}{4}\xi - \frac{1}{4}\xi^3\right) flag_5 \\ S_{i=4}(\xi \text{ or } \eta) &= \left(-\frac{1}{8} - \frac{1}{8}\xi + \frac{1}{8}\xi^2 + \frac{1}{8}\xi^3\right) flag_6 \end{aligned} \tag{6.12}$$

An overview of the shape functions and associated approximation order is given in Table 6.1. A number of m and n shape functions can be selected in respectively the x and y direction, which are then combined together to obtain the final shape function g, as shown in Equation 6.13 and 6.14. All shape functions are included in the permutation, but when a flag is set to zero in order to disable a certain displacement mode, it will result in some final shape functions g being zero. Due to the combination of the basic shape functions, the unknown coefficient vector c has a (3xmxn)x1 dimension. A convergence study on the required number of shape functions is done in Chapter 9.

Table 6.1: Shape function order and numbering.

	1st term	2nd term	3rd term	4th term	5th term	6th term
$u(\xi)$	u_1	u_2	$S_{i=5}$	$S_{i=6}$	$S_{i=7}$	$S_{i=8}$
$v(\eta)$	v_1	v_2	$S_{i=5}$	$S_{i=6}$	$S_{i=7}$	$S_{i=8}$
$w(\xi \text{ or } \eta)$	$S_{i=1}$	$S_{i=2}$	$S_{i=3}$	$S_{i=4}$	$S_{i=5}$	$S_{i=6}$

$$g_u, g_v = \sum_{i=1}^{m} \sum_{j=1, j\neq i}^{n} u_i(\xi) v_j(\eta) \tag{6.13}$$

$$g_w = \sum_{i=1}^{m} \sum_{j=1, j\neq i}^{n} w_i(\xi) w_j(\eta) \tag{6.14}$$

6.1.5 Strains

From the displacement fields, the in-plane material strains can be obtained from the Green-Lagrange strain definition given in Equation 6.15.

$$\varepsilon_{ij} = \frac{1}{2}\left(u_{i,j} + u_{j,i} + u_{k,i} u_{k,j}\right) \tag{6.15}$$

Applying the strain definition to the classical plate theory displacement of Equation 6.7, the normal strain ε_{xx} in the x direction can be obtained, as shown in Equation 6.16.

$$\varepsilon_{xx} = u_{,x} + \frac{1}{2}\left(\cancel{v_{,x}^2}^{\ll w_{,x}^2} + \cancel{v_{,x}^2}^{\ll w_{,x}^2} + w_{,x}^2 \right) = u_{,x}^0 - z w_{,xx} + \frac{1}{2} w_{,x}^2 \tag{6.16}$$

All the crossed out terms have a small contribution compared to the other terms, and can be neglected for the analysis [34]. Analogously, the in-plane normal strain ε_{yy} and in-plane shear strain γ_{xy} can be computed, where the engineering shear strain is related to the Green-Lagrange strain as $\gamma_{xy} = 2\varepsilon_{xy}$.

Defining the strain vector $\{\varepsilon\}$ as given in Equation 6.17, the strains and curvatures of Equation 6.16, and other in-plane components can directly be related to the shape functions and unknown coefficients in matrix form as shown in Equation 6.18.

$$\left\{\varepsilon\right\} = \begin{Bmatrix} \varepsilon_{xx} \\ \varepsilon_{yy} \\ \gamma_{xy} \\ \kappa_{xx} \\ \kappa_{yy} \\ \kappa_{xy} \end{Bmatrix} = \begin{Bmatrix} u_{,x}^0 + \frac{1}{2} w_{,x}^2 \\ v_{,x}^0 + \frac{1}{2} w_{,y}^2 \\ u_{,y}^0 + v_{,x}^0 + w_{,x}\, w_{,y} \\ -w_{,xx} \\ -w_{,yy} \\ -2w_{,xy} \end{Bmatrix} \tag{6.17}$$

$$\left\{\varepsilon\right\} = \left(\left[B_0\right] + \frac{1}{2}\left[B_L\right] \right) \left\{c\right\} \tag{6.18}$$

The matrix $[B_0]$ contains the linear strain component, and $[B_L]$ the non linear ones. The definition of these matrices can be found in Appendix B, where the change of variables is performed, according to the chain rule as given in Equation 6.3 to incorporate the transformation to the natural coordinate system.

6.1.6 Eigenvalue Problem

The response of the laminate is characterised by the Total Potential Energy (TPE) Π principle, given in Equation 6.19, which is the difference between the strain energy U and the external work V. Starting from the definition of the strain energy given in Equation 6.20, Equation 6.21 can be obtained by carrying out the change of variable of Equation 6.1.

$$\Pi = U - V \tag{6.19}$$

$$U = \frac{1}{2} \int_V \{\sigma\}^T \{\varepsilon\} dV \tag{6.20}$$

$$U = \frac{1}{2} \int_z \int_\eta \int_\xi \{\sigma\}^T \{\varepsilon\} \det J d\xi d\eta dz \tag{6.21}$$

Furthermore, incorporating the strain definition derived in Equation 6.16 and alike for the other in-plane strains, followed by the integration with respect to the laminate's thickness, Equation 6.22 is obtained, with $d\Omega = d\xi d\eta$ [47]. $\left\{\varepsilon\right\}$ is still equal to the definition given in Equation 6.17, whereas

$\{N\}^T$ equals $\{N_{xx} \quad N_{yy} \quad N_{xy} \quad M_{xx} \quad M_{yy} \quad M_{xy}\}$, due to the stress integration over the thickness of the in-plane and out-of-plane strains.

$$U = \frac{2}{LW} \iint_{\Omega} \{\varepsilon\}^T \{N\} \, d\Omega \tag{6.22}$$

Equivalently, integrating the plane stress relationship of the laminate $\{\sigma\} = [Q]\{\varepsilon\}$ as defined in Appendix A over the thickness yields the ADB relation as given in Equation 6.23.

$$\begin{Bmatrix} N \\ M \end{Bmatrix} = \begin{bmatrix} A & B \\ B & D \end{bmatrix} \begin{Bmatrix} \epsilon \\ \kappa \end{Bmatrix} \tag{6.23}$$

The general expression for the external work V is defined as shown in Equation 6.24, and represents the dot product of the displacement and the external forces F_{ext} acting on the boundary of the laminate $\partial\Omega$.

$$V = \int_{\partial\Omega} F_{ext} \cdot u d\partial\Omega \tag{6.24}$$

It can be written as Equation 6.25, following the replacement of the displacement by the Ritz approximations, and decomposing the external force vector and displacement in x and y direction.

$$V = \{c\}^T \int_{\partial\Omega} \begin{bmatrix} S_u \\ S_v \end{bmatrix}^T \begin{Bmatrix} F_x \\ F_y \end{Bmatrix} d\partial\Omega \tag{6.25}$$

The buckling problem itself is formulated on the Neutral Equilibrium Criterion of Π, expressed in Equation 6.26, following the derivation in [34, 47]. The neutral equilibrium point defines the point between the stable and unstable region of the structure. This definition is preferred in the context of membrane-bending coupling behaviour, where out-of-plane deflections will be present before the buckling point is attained.

$$\delta^2\Pi = 0 \implies \delta(\delta U - \delta V) = 0 \tag{6.26}$$

The first variation of the external work is given in Equation 6.27. The forces are assumed to be conservative, hence they do not depend on the displacement and have no variation.

$$\delta V = \{\delta c\}^T \int_{\partial\Omega} \begin{bmatrix} S_u \\ S_v \end{bmatrix}^T \begin{Bmatrix} F_x \\ F_y \end{Bmatrix} d\partial\Omega \tag{6.27}$$

The first variation of the strain energy is given in Equation 6.28, and can be simplified to Equation 6.29, due to the symmetry of the constitutive ABD matrix [33].

$$\delta U = \frac{2}{LW} \left(\iint_{\Omega} \{\delta\varepsilon\}^T \{N\} \, d\Omega + \iint_{\Omega} \{\varepsilon\}^T \{\delta N\} \, d\Omega \right) \tag{6.28}$$

$$\delta U = \frac{4}{LW} \iint_{\Omega} \{\delta\varepsilon\}^T \{N\} \, d\Omega \tag{6.29}$$

The variation of the strain vector can be written with a dependency on the unknown coefficients as shown in Equation 6.30.

$$\{\delta\varepsilon\} = \left[[B_0] + [B_L]\right]\{\delta c\} = [\bar{B}]\{\delta c\} \tag{6.30}$$

Replacing the variation of the strain vector results in the expression shown in Equation 6.31, where the unknown coefficient can be taken out of the integrands as they do not depend on the integration variables.

$$\delta U = \frac{4}{LW}\iint_{\Omega}\{\delta\varepsilon\}^T\{N\}\,d\Omega = \frac{4}{LW}\{\delta c\}^T\iint_{\Omega}[\bar{B}]^T\{N\}\,d\Omega \tag{6.31}$$

Afterwards, the second variation is applied to both the external work and strain energy to obtain the expressions given in Equation 6.32 and 6.33 respectively.

$$\delta^2 V = \cancel{\{\delta^2 c\}^T} \ll \delta c \int_{\partial\Omega}\begin{bmatrix}S_u\\S_v\end{bmatrix}^T\begin{Bmatrix}F_x\\F_y\end{Bmatrix}d\partial\Omega \tag{6.32}$$

$$\delta^2 U = \frac{4}{LW}\cancel{\{\delta^2 c\}^T} \ll \delta c \left[\iint_{\Omega}[\bar{B}]^T\{N\}\,d\Omega\right] + \{\delta c\}^T\left[\frac{4}{LW}\iint_{\Omega}\left([\delta\bar{B}]^T\{N\} + [\bar{B}]^T\{\delta N\}\right)d\Omega\right] \tag{6.33}$$

The second variation of the coefficients c is assumed to be much smaller than the product of the first variation, and is therefore be neglected, meaning $\delta^2 V$ is omitted. Furthermore, the first part of the integrand of Equation 6.33 can be rewritten as Equation 6.34 [34], to obtain the geometric stiffness matrix $[K_{G_0}]$. This is only based on the non-linear strain components $[B_L]$, as they are the only one depending on the coefficients c. The initial membrane stress matrix $[N_{K_G}]$ is defined as shown in Equation 6.35, and obtained from a static analysis, as explained in Section 6.1.7, and $[G]$ is given by Equation 6.36 [47]. The definition of the matrix $[K_{G_0}]$ can be found in Appendix B.

$$\frac{4}{LW}\iint_{\Omega}[\delta\bar{B}]^T\{N\}\,d\Omega = \frac{4}{LW}\iint_{\Omega}[G]^T\left[N_{K_G}\right][G]\,d\Omega\{\delta c\} = [K_{G_0}]\{\delta c\} \tag{6.34}$$

$$\left[N_{K_G}\right] = \begin{bmatrix}N_{xx} & N_{xy}\\N_{xy} & N_{yy}\end{bmatrix} \tag{6.35}$$

$$[G] = \begin{bmatrix}\frac{2}{L}\frac{\partial S_w}{\partial\xi}\\\frac{2}{W}\frac{\partial S_w}{\partial\eta}\end{bmatrix} \tag{6.36}$$

The integrals to construct $[K_{G_0}]$ are evaluated numerically, since the stress resultants are also a function of the spatial location and must be kept within the integrand. To this end, a Gaussian quadrature rule is used, where the integral is approximated by Equation 6.37. The weights w_i, w_j and locations x_i, y_i can be obtained from [59]. A convergence study on the required number of integration points is carried out and presented in Chapter 9.

$$\int_{-1}^{1}\int_{-1}^{1} f(x,y)dxdy \approx \sum_{i=1}^{n}\sum_{j=1}^{m} w_i w_j f(x_i, y_j) \tag{6.37}$$

The right hand side of the integrand in Equation 6.33 can be rewritten as shown in Equation 6.38, by using the ABD relationship of Equation 6.23 to obtain the constitutive stiffness matrix $[K_0]$, given in detail in Appendix B. It is based only on the linear strain terms $[B_0]$ of $[\bar{B}]$, since no large displacements are considered in this analysis.

$$\frac{4}{LW}\iint_{\Omega}\left[\bar{B}\right]^{T}\left\{\delta N\right\}d\Omega=\frac{4}{LW}\iint_{\Omega}\left[B_0\right]^{T}\left[ABD\right]\left[B_0\right]d\Omega\left\{\delta c\right\}=\left[K_0\right]\left\{\delta c\right\} \tag{6.38}$$

$[K_0]$ is also computed numerically, with the evaluation of the ABD matrix at the location of the integration points. Both geometric and constitutive stiffness matrices will have a (3xmxn)x(3xmxn) shape, dictated by the amount of shape functions m and n, in x and y direction receptively. Each entry of those matrices will be evaluated for pxq integration points, again in x and y direction receptively.

Finally, the second variation of Π can be written as Equation 6.39. This must be valid for any δc, therefore introducing the membrane stress load multiplier λ, it is reduced to Equation 6.40, resulting in the general eigenvalue problem of Equation 6.41. Solving this linear problem will give in the buckling eigenvalues λ, and corresponding eigenmodes Φ [33].

$$\delta^2\Pi=\left\{\delta c\right\}^{T}\left(\left[K_0\right]+\left[K_{G_0}\right]\right)\left\{\delta c\right\}=0 \tag{6.39}$$

$$\det\left(\left[K_0\right]+\lambda[K_{G_0}]\right)=0 \tag{6.40}$$

$$[K_0]\{\Phi\}=-\lambda[K_{G_0}]\{\Phi\} \tag{6.41}$$

6.1.7 Force Based

The stress resultants to construct matrix $[N]$ are obtained by means of a static analysis of the laminate undergoing the loading condition of the multiplier λ. This analysis stems from the first variation of the TPE, which dictates the equilibrium of the laminate, given in Equation 6.42.

$$\delta\Pi=0\implies\delta U-\delta V=0 \tag{6.42}$$

The variation of the internal strain and external work were already derived in the previous section, in Equation 6.27 and 6.31 respectively. Replacing these expressions in Equation 6.42 leads to the expression given in Equation 6.43.

$$\{\delta c\}^{T}\left(\iint_{\Omega}[B_0]^{T}[ABD][B_0]\{c\}d\Omega-\int_{\partial\Omega}\begin{bmatrix}S^u\\S^v\end{bmatrix}^{T}\begin{Bmatrix}F_x\\F_y\end{Bmatrix}d\partial\Omega\right)=0 \tag{6.43}$$

This expression must hold true for any variation of $\{\delta c\}$, hence the solution to this equality is obtained by means of Equation 6.44, where f equals $\int_{\partial\Omega}\begin{bmatrix}S^u\\S^v\end{bmatrix}^{T}\begin{Bmatrix}F_x\\F_y\end{Bmatrix}d\partial\Omega$.

$$\left[K_0\right]\left\{c\right\}=\left\{f\right\} \tag{6.44}$$

Solving this linear problem will result in the value of the unknown coefficients c. These can then be used in junction with Equation 6.16 to obtain the local strains, and then be transformed to membrane stress N_{xx}, N_{yy} and N_{xy} by means of Equation 6.23.

6.2 Finite Element Method

In order to verify the semi-analytical model, its buckling results are compared to those obtained by means of FEM. This section explains the parameters used to perform the FEM analysis. As was discussed in Section 3.2, previous researches have used shell elements and letting the stiffness vary per element. The same approach is adopted in the current FEM analysis.

The model is created as a 3D deformable planar shell, with the S4R element in Abaqus [48]. The S4R is a general purpose shell element, which allows to define a custom layup per element with the respective thought the thickness distribution. The S4R element stiffness matrix is derived from the FSDT, resulting in a more compliant deformation, however for the same definition of the buckling problem. The element layup is retrieved from the closest laminate mesh point to the element's centroid, which holds the information about the global fibre orientation and thickness of each ply.

In order to mimic the plate offset, each element layup was repositioned to have a flat bottom face and the same ABD plane. The integrated offset feature of Abaqus was used to perform this, where each layup was given an offset ratio according to Equation 6.45. t_{local} is the local thickness of the element at hand, whereas t_{min} is the smallest thickness of the laminate. This leads to the laminate representation shown in Figure 6.5.

$$\text{offset ratio} = \frac{-\left(\frac{t_{local}}{2} - \frac{t_{min}}{2}\right)}{t_{loc}} \tag{6.45}$$

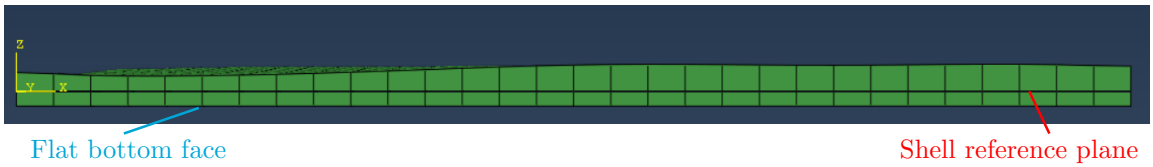

Figure 6.5: Abaqus shell offset to obtain the same ABD plane and a one-sided flat plate.

Lastly, the loading conditions were applied as shell edge loads to the respective element sides, as were the boundary conditions to the corresponding nodes. This complete procedure was automatised by means of a Python script, allowing to quickly and effectively create an Abaqus analysis input file, and evaluate separate cases with different FEM element mesh densities or layups.

6.3 Procedure Overview

Finally, an overview of the procedure to obtain the virtual manufactured panel with either a discrete or smeared thickness, and subsequent buckling analysis, is shown in Figure 6.6.

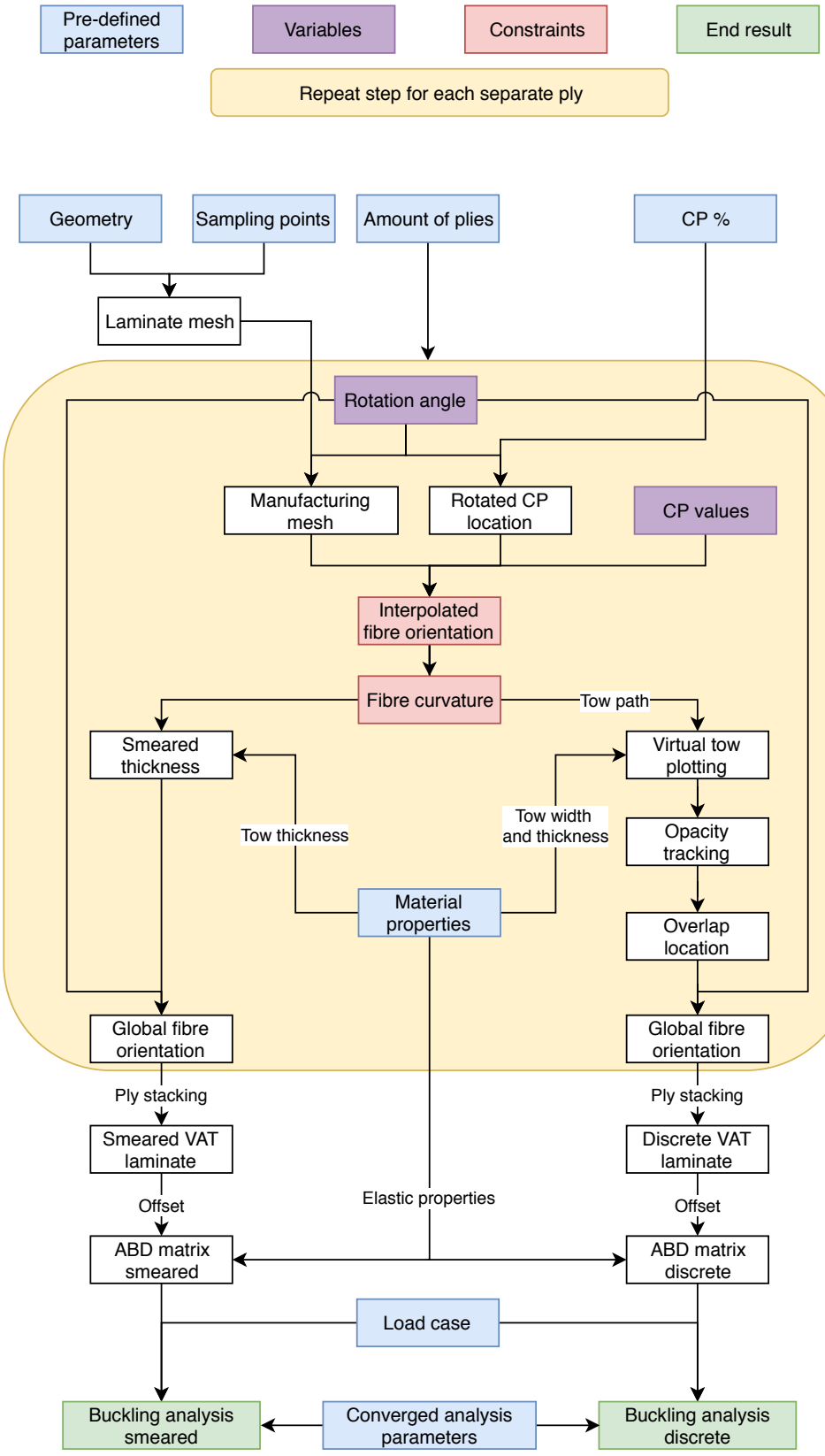

Figure 6.6: Virtual manufacturing and buckling analysis flowchart.

Chapter 7

Optimisation

Once the semi-analytical smeared model has been verified against the discrete FEM case (see Section 7.1), it can be used to analyse, design and optimise the thickness variation alongside the fibre steering. In first instance, an optimisation will be conducted to evaluate possible better designs, from which discussions on the influence thickness variation can be performed. Furthermore, it allows to draw a comparison with the case of steered fibres with a uniform thickness profile, obtained by the use of the cut and restart manufacturing possibility.

The general optimisation problem is stated in Equation 7.1, where the objective function $f(\bar{x})$ returns the negative of the absolute value of the first buckling eigenvalue obtained by the semi-analytical modelling. The different constraints, layups and test cases are discussed next.

$$\begin{aligned} \underset{\bar{x}}{\text{minimise}} \quad & f(\bar{x}) \\ \text{subject to} \quad & g_i(\bar{x}) \leq b_i,\ i = 1, \ldots, m. \end{aligned} \tag{7.1}$$

This problem is solved by means of the implemented SLSQP algorithm in the Scipy.optimize package [60] of Python. This algorithm, based on Sequential Quadrature Programming, solves the Karush–Kuhn–Tucker conditions based on Newton's method [61]. The derivatives of the objective function with respect to the variables are obtained numerically by a forward differentiation scheme. This algorithm is chosen since it handles both constraints and initial variable guesses outside the valid range. The standard algorithm cut-off criteria of changes less than $1e^{-6}$ in $f(\bar{x})$ is adopted, as is the step size of $1.5e^{-8}$ in the determination of numerical derivatives. The optimisation variables can be defined per ply, and are the ply rotation angle χ and equivalent CP values ϕ_m to the amount of CP, defined beforehand. The number of variables increases as an integer multiplication for additional plies.

Each variable is bounded as shown in Table 7.1. The rotation angle is constrained to allow a full rotation in total, and the CP values are limited because of the angle limit set out for the plate assumption and thickness increase. To build confidence in the optimal results, several optimisations are performed starting with different initial guesses of the variables, all chosen randomly within their bounds.

The optimisation is subject to 3 main constraints: mass, fibre orientation and curvature. The first constraint is used to allow the change in thickness to happen locally where the increase in stiffness is required. Starting from a fictional uniform thickness laminate, the maximum mass is set to be equal to that same laminate with 1 added ply. This discrete step in mass allows to also optimise uniform steered fibre laminate with gaps and the cut and restart possibility, and compare possible improvements at isomass of the varying thickness VAT laminates.

Table 7.1: Bounds of the optimisation variables.

Variable	Lower bound [°]	Upper bound [°]
CP value ϕ_m	-60	60
Rotation angle χ	-180	180

The constraint on the fibre orientation interpolation ϕ is subjected to the same limit as the CP values given in Table 7.1, to adhere to the assumptions of the buckling model. Finally, the curvature constraint takes into account the manufacturing possibilities of AFP machines, and is set to a limit of 1.575 $1/m$. Both those last 2 constraints are evaluated for all sampling points, and the most critical is taken to be compared with the constraint. Finally, both the objective function and inequalities are normalised to be used in the scheme.

Along the constraints, 3 different layup possibilities are optimised for: a symmetric and balanced one, a layup with minimised coupling effect and a generic layup. The first 2 layup configurations are defined in order to try and reduce unwanted coupling behaviour between membrane shear, bending twisting and membrane bending. The symmetric and balanced case is based on the rules for uniform laminates, and included in order to evaluate the magnitude of the coupling effects which are then only created by the thickness offset.

The second stacking sequence possibility, is a generic one where the magnitude of the unwanted coupling terms are constrained to be at least an order of magnitude smaller than the next larger term for any location of the laminate mesh.

Lastly, a complete generic stacking sequence free of rules is used to evaluate the full possible benefit of varying thickness varying stiffness laminates. Along those 3 layup conditions for varying thickness, an optimisation is also performed on an uniform thickness steered laminate to compare benefits, where the extra ply of the mass constraint is added. The layup sequence is again either generic or constrained to the symmetric and balanced rules, with the added ply at the centre. This ply violates the balanced rule, but it is expected to be of least influence as it is locate on the midplane. The uniform case modelled with the same methodology as the smeared case, except that the ply thickness is always the nominal thickness everywhere.

All these optimisations are then run for three different cases, discussed next, to represent a variety of geometry, loading and boundary conditions. Furthermore, these cases will also serve as verification examples with a free layup, to prove the suggested methodology for the different conditions.

Case 1

Case 1 is an equal bi-directional loading case for a square plate, simply supported on three sides, with dimensions of 1500x1500 mm. The laminate consists of a four ply for the varying thickness, whilst five layers are used for the uniform case. It is represented in Figure 7.1. In the simulation, the left side is pinned, otherwise numerical errors occur.

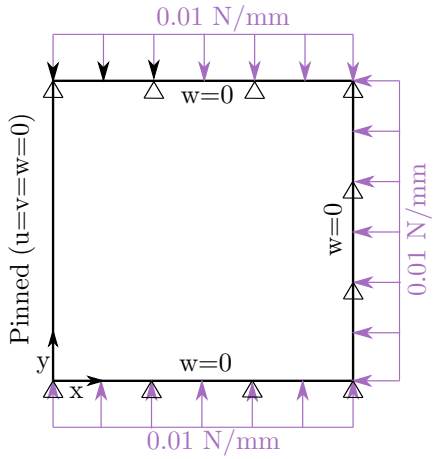

Figure 7.1: Optimisation case 1 geometry, loading and boundary conditions.

Case 2
Case 2 represents a flange, where a plate of higher aspect ratio is simulated, with three edges simply supported and 1 long edge free. It is only loaded in the longitudinal direction, and has a length of 1000 mm and width of 200 mm. The laminate has the same amount of plies as in case 1. It is represented in Figure 7.2.

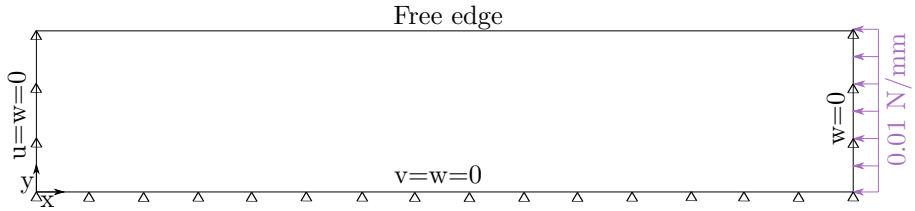

Figure 7.2: Optimisation case 2 geometry, loading and boundary conditions.

Case 3
Case 3 is a multi loading case, representing a scaled up root wing bay due to the large steering radius. It consists of a panel with an aspect ratio of two, being 2000 mm long and 1000 mm heigh. It is loaded by a running load in the y direction $3/10^{th}$ of the distributed load in the x direction and a shear load applied at the opposite side of the clamp with a total load half that of the x direction. The laminate consists of an eight ply for the varying thickness, whilst nine layers are used for the uniform case. It is represented in Figure 7.3.

All the CP are located at 0%, 33%, 66% and 100%. The uniform thickness laminates have the same CP relative positions, but have additional plies corresponding to the mass increased allowed by the constraint in the optimisation. The number of CP was selected to allow for a possible higher degree of interpolation, as it can still produce a linear variation, however still gives the thickness variation to happen more locally by having a higher degree, and therefore assess the effectiveness in improving the buckling.

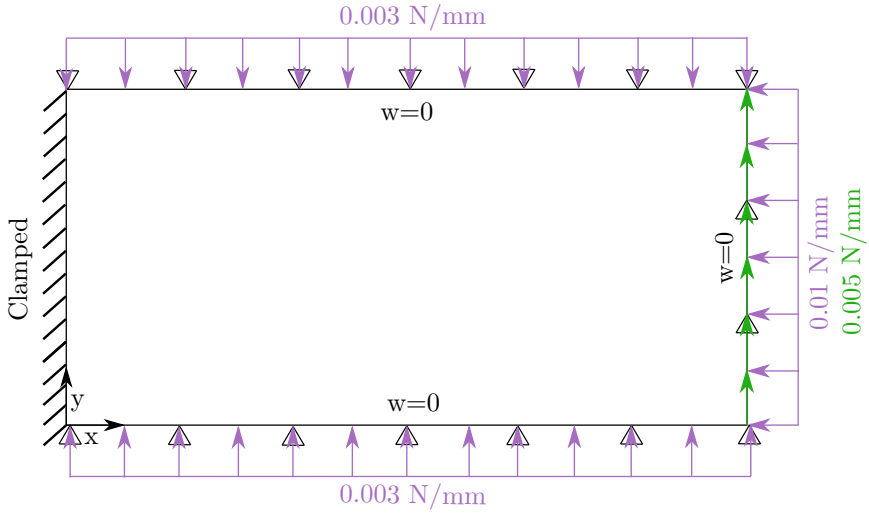

Figure 7.3: Optimisation case 3 geometry, loading and boundary conditions.

Part III

Results

Chapter 8

Virtual Manufacturing Verification

In order to verify the virtual manufacturing approach, several components must be tested. In first instance, the tow path information is compared to known expected values in Section 8.1. Secondly, the overlap retrieval is discussed in Section 8.2. Afterwards, the convergence of the sampling points and the mass prediction are verified in Section 8.3. Finally, Section 8.4 discusses the complete virtual manufacturing, and especially the thickness pattern between the discrete and smeared method.

8.1 Tow Path and Radius of Curvature

The first verification part is focussed on the tow centreline path and curvature calculation, and uses the virtual manufacturing example given in Figure 5.5 and Table 5.2. The tow centreline definition is verified by differentiating numerically the obtained path, and subsequently comparing its orientation by means of Equation 5.4 to the interpolated values of the Lagrange scheme. The comparison is given in Figure 8.1, where both result are in good agreement. Moreover, as was shown in Figure 5.5, the concurrent graph of the tow path and fibre orientation does coincide visually.

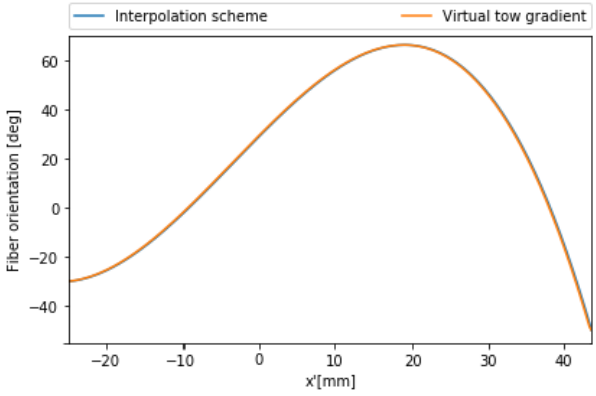

Figure 8.1: Tow path and interpolated orientation comparison.

Secondly, this example is also used to verify the radius of curvature method of Section 5.4. The proposed method is compared to the analytical expression shown in Equation 8.1 [11], which computes the radius of curvature between two points separated by distance a along the x' axis, with associated fibre orientation θ. The result of this comparison is shown in Figure 8.2.

$$r = \frac{a}{\sin\theta_1 - \sin\theta_0} \tag{8.1}$$

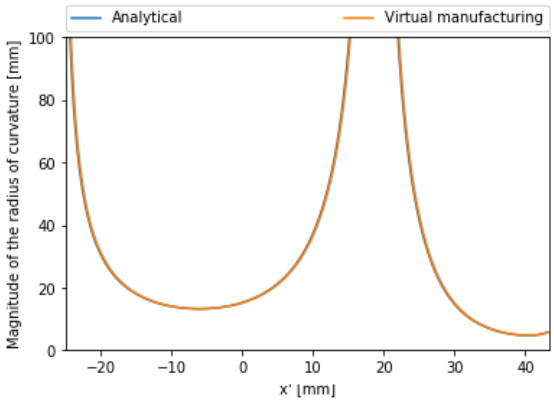

Figure 8.2: Radius of curvature comparison between the virtual manufacturing and the analytical expression of Equation 8.1.

Both methods give equal results, where the graph has been cut-off for very large radius of curvature, corresponding to near flat parts in the tow path.

8.2 Repeat Unit

The next part of the virtual manufacturing to be verified, is the overlap reconstruction based on the tow plotting in the repeat unit. To this end, a visual comparison is made between both plotted and retrieved graphs. A first example of the tow plotting is shown in Figure 8.3 with associated overlap plot in Figure 8.4. The standard resolution of matplotib is used, being 300 dpi, and also $N_s = 200$ to smoothly represent the path. A discussion about the effects of the resolution and sampling points N_s is done in Section 8.3 and Chapter 9.

From both figures, it can be seen that the overall overlap shape is well reproduced, however two errors show up locally. First, when looking at the left side of Figure 8.4, the tows seem to be cut-off and stop abruptly. Comparing this to the virtual plotting at the same location, there the tows do continue in a correct way and are only stopped at the edge. This feature was identified to only happen for tows whose local angle are greater than $|45°|$, demonstrated by the right edge having an angle of 45°, as opposed to the left side where $\phi = 40°$. This error is assumed to come from the built in algorithm of matplolib on the retrieval of the alpha channel, since the virtual plot does not show any distortion. Therefore, the edge CP values will be selected to be lower than $|45°|$ for the cases used to verify the semi-analytical and smeared approached compared to the discrete case.

Secondly, when looking at the overlap boundaries along x' = 20 mm, they are not repeating consistently. This phenomenon is most visible in regions where the manufacturing angle is and the overlap region is small. The same phenomena also happens for larger overlap regions, however it is less visible since it happens at a smaller scale. The reason for this distortion is a combination of numerical errors and small margins. When the overlap region is only a few dots wide, any difference in pixel location will result in being inside of outside that overlap region. This difference is accentuated due to the

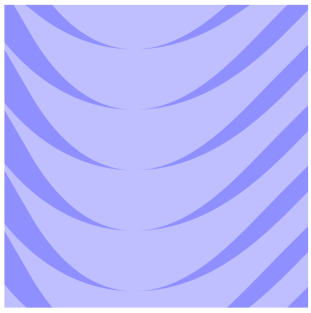

Figure 8.3: Virtual tow path plot example 1.

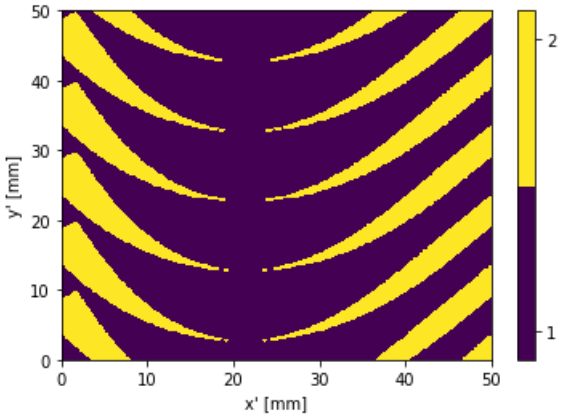

Figure 8.4: Amount of overlaps, retrieved from Figure 8.3(dpi=300, N_s=200).

sampling points not being located at integer numbers, but a fraction of the plate's dimensions, followed by a change of resolution from inches to metric. These two operations can introduce numerical errors, which must be further rounded to obtain an integer location of a pixel, and result in a small differences. This then dictates whether a location falls within or outside an overlap, and creates these local distortions.

A second example of a virtual plotted tow path is shown in Figure 8.5. This is then subsequently translated to the overlap retrieval for the same amount of N_s in case of a small plate in Figure 8.6, and a large plate in Figure 8.7.

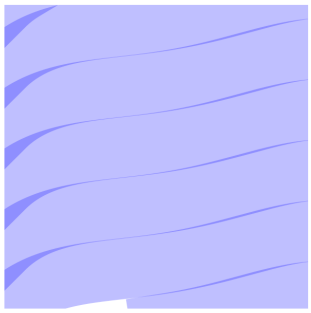

Figure 8.5: Virtual tow path plot example 2.

First of all, the bottom of Figure 8.5 was not completely covered by the plotting of the last tow, it is to counter those possible edge errors that the repeat unit is extracted from the middle of the virtual plot. Furthermore, the overlap contour in Figure 8.6 has the same issue as mentioned for the previous example. However, when looking a the same ply for a scaled up plate as in Figure 8.7, the overlap patterns become even more distorted. There are 2 reasons for this behaviour: the first one is the numerical errors as for smaller plates, and the second being the sampling. In case of the larger dimensions, the mesh is created to store information and be used, rather than visually reproduce the tow path and overlaps. It can still be used to give a global overview, but can not say anything anymore locally. It is considered in the discussion about the resolution and sampling size later on.

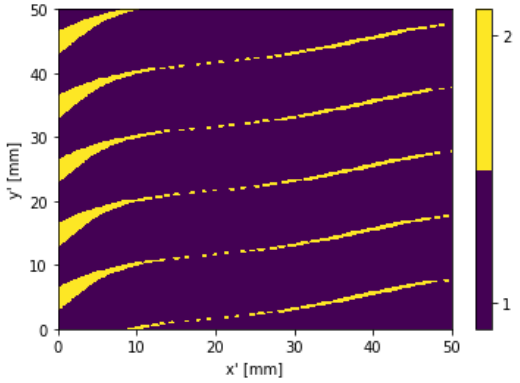

Figure 8.6: Amount of overlaps retrieved from Figure 8.5 for a small plate (dpi=300, N_s=200).

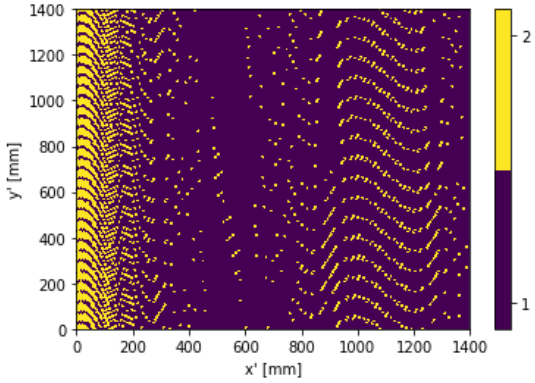

Figure 8.7: Amount of overlaps retrieved from Figure 8.5 for a large plate (dpi=300, N_s=200).

Finally, the matplotlib package reaches its plotting and memory limits for very long x' distance, sometimes not being able to virtual plot the tows over the complete length, and therefore the retrieval of overlaps is not accurate. That restriction was also considered in selecting the verification cases and layups, through appropriate selection of the rotation angles χ.

As a conclusion, the virtual plotting method shows capabilities to represent overlaps, especially at lower scales, but struggles for larger tow width over plate dimension ratios. These limits are surpassed in the verification cases by also investigating the resolution and sampling effect, and selecting appropriate layups. However, for large plates, the virtual manufacturing could not be done without the repeat unit concept, since memory issue would have arisen without it. Therefore it is still deemed the best option for these situations.

8.3 Laminate Mesh Convergence

The first investigation into the effect of the amount of sampling points and resolution is done through the convergence of the panel's mass. To this end, the three optimisations cases are used. They are all given random layups, by means of χ and ϕ_m, however the laminate definition is equal in case of the discrete and smeared approximation. The values for the three cases are shown in Table 8.1, and will also be used in the subsequent verification steps, along the material properties given in Table 8.2. The density was assumed to be that of a general composite, as it is only a constant scaling. The tow width was selected to be 1/4 inch for the discrete thickness, whose effect is further analysed in Section 9.4. The mass prediction based on the amount of sampling points and resolution for all three cases in given in Figure 8.8 for the discrete mass, and in Figure 8.9 for the smeared mass.

Table 8.1: Verification cases layup.

	Layer number	χ [°]	ϕ_1 at 0% [°]	ϕ_2 at 33% [°]	ϕ_3 at 66% [°]	ϕ_4 at 100% [°]
Case 1	1	4	45	7	13	6
	2	59	5	37	-25	-19
	3	-16	27	-25	-8	40
	4	1	-39	53	15	-14
Case 2	1	-42	-25	48	54	-8
	2	86	-42	9	-40	24
	3	-14	-42	-25	-7	30
	4	4	16	-52	-16	-35
Case 3	1	21	-8	-48	12	40
	2	60	-39	-24	-4	42
	3	42	-43	54	-29	-3
	4	68	2	-48	-45	-33
	5	-45	25	-5	43	-13
	6	-47	53	-25	13	10
	7	-52	3	-7	49	-43
	8	9	-33	-29	-10	-39

Table 8.2: Material properties [10].

Property	Value	
E_{xx}	181e3	[GPa]
E_{yy}	10.3e3	[GPa]
ν_{xy}	0.28	[-]
G_{xy}	7.2e3	[GPa]
t_{tow}	0.127	[mm]
w_{tow}	6.35	[mm]
$\rho_m at$	1700	$[\frac{kg}{m^3}]$

First of all, using less than 50 sampling points is not possible, as too little sampling points are available to construct the virtual manufacturing information. Secondly, even for 50 sampling points, the mass has already converged to changes of less than 1% in both smeared and discrete cases. The latter one however, shows higher variation as the amount of N_s is increased. This is because the thickness happens in discrete steps and is not continuous, as opposed to the smeared thickness, which converges steadily. The difference between the higher and lower dpi resolution is between 0.5% and 0.6% for all cases, showing there is little effect of the resolution of the plotting on the global result with a high number of sampling points.

To verify the mass prediction, both smeared and discrete mass for 200 sampling points and 300 dpi are compared to the mass obtained from the average smeared thickness times the plate area and material density. The comparison is shown in Table 8.3. It must be noted that only the discrete mass has dependency on the resolution, as it is used in plotting the tows and retrieving the overlaps. On the contrary, the smeared thickness only depends on the manufacturing angle through Equation 5.9.

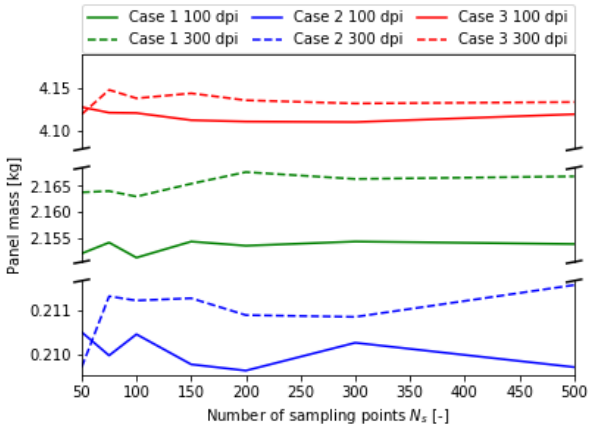

Figure 8.8: Discrete thickness mass convergence.

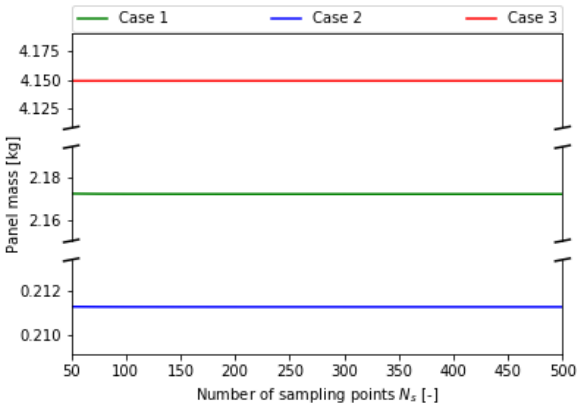

Figure 8.9: Smeared thickness mass convergence.

Table 8.3: Mass verification by comparison with the average smeared thickness mass.

	Average thickness mass [kg]	Discrete mass [kg]	Difference [%]	Smeared mass [kg]	Difference [%]
Case 1	2.17	2.17	0.22	2.17	-0.01
Case 2	0.21	0.21	-0.02	0.21	0.03
Case 3	4.15	4.15	0.00	4.15	0.00

For all cases, both the discrete and smeared mass are in good agreement with each other and the average thickness one, therefore it is concluded that the mass prediction is verified. This also verifies the assumptions made by Castro et al. [51] in the derivation of the smeared expression, requiring the final mass to remain constant. Moreover, it is assumed that the maximum attained manufacturing angle ϕ and curvature have also converged, as they are directly or indirectly linked to all the parameters used in the mass prediction. Hence 50 sampling points would be enough to recreate all the information needed for the buckling analysis. However, for the sake of producing a more detailed information, a sampling of 200 points is decided for all future analysis. This higher amount of points is mostly used just for the visual and detailed comparison between the approximation of the smeared and discrete thickness profile, where efficiency is not the main factor. Once the comparison of thickness modelling is done, then a lower amount of sampling points can be used, as the semi-analytical smeared approach can directly obtained the required information at the integration points without making use of the sampling points. Only for the curvature and maximum manufacturing constraint in the optimisation are the sampling points used, were 50 sampling points suffice.

8.4 Complete Process

Finally, with all the parts verified for the virtual manufacturing, the complete procedure is verified by comparing the discrete thickness distribution visually to the smeared approximation. Despite the smeared method being continuous, both methods should reveal a similar thickness pattern.

Again, this is compared for the geometry of the three optimisation cases, with the layup in formation of Table 8.1. The pattern comparison of case 1 is made in Figure 8.10 and 8.11, whereas Figure 8.12 shows the discrete overlaps and Figure 8.13 the smeared thickness of case 2. Finally, the results of case 3 are shown in Figures 8.14 and 8.15.

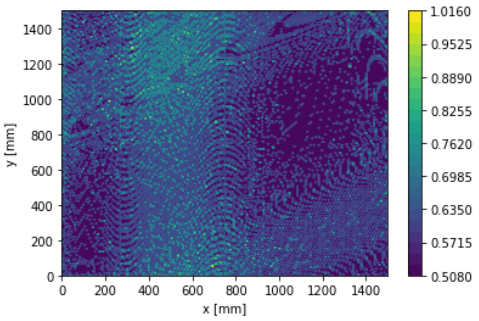

Figure 8.10: Discrete thickness profile of case 1 with the layup of Table 8.1 (dpi=300, N_s=200).

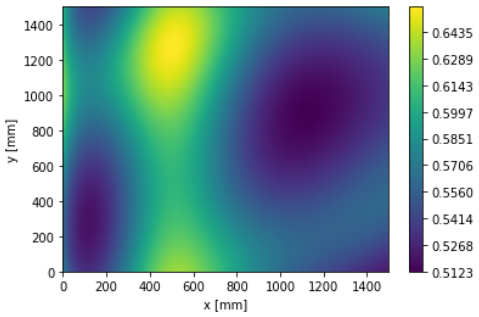

Figure 8.11: Smeared thickness profile of case 1 with the layup of Table 8.1(N_s=200).

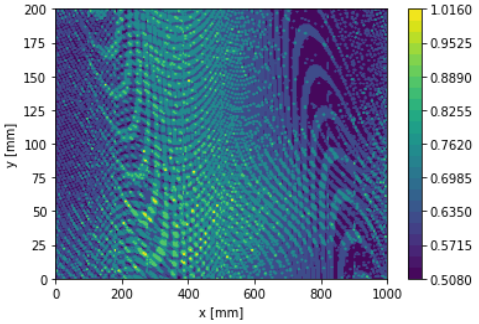

Figure 8.12: Discrete thickness profile of case 2 with the layup of Table 8.1(dpi=300, N_s=200).

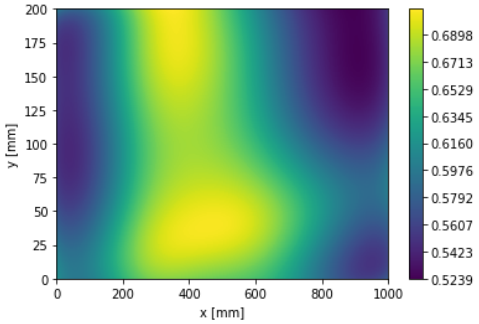

Figure 8.13: Smeared thickness profile of case 2 with the layup of Table 8.1(N_s=200).

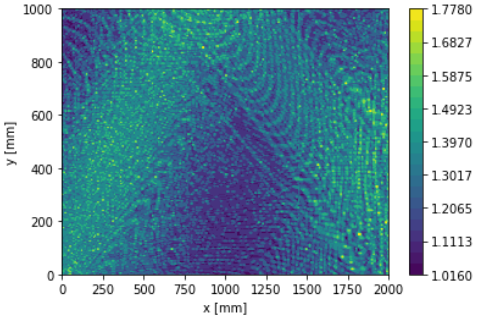

Figure 8.14: Discrete thickness profile of case 3 with the layup of Table 8.1(dpi=300, N_s=200).

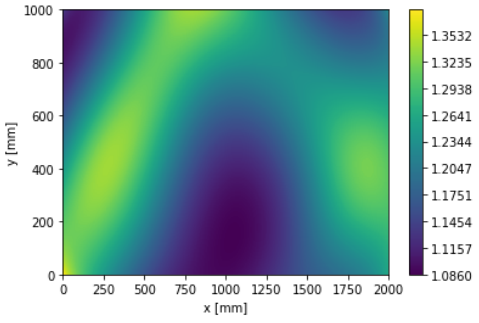

Figure 8.15: Smeared thickness profile of case 3 with the layup of Table 8.1(N_s=200).

When analysing each of the three cases, it can be seen that the thickness patterns are in good agreement, with shape and location of the darker thinner area coinciding, as well as the brighter thicker ones. Therefore, the virtual manufacturing method as explained in Section 5 can be used to predict the location of overlaps, and can be used to map the discrete thicknesses for VAT laminates produced by AFP with continuous fibres.

In Table 8.4, an overview of particular values between the discrete and smeared case is displayed. The maximum discrete thickness is much higher than the smeared one, however can be explained by two reasons. First, the discrete thickness can only jump in distinct steps corresponding to the ply thickness, meaning a sizeable difference will be obtained more easy. Secondly, the high thickness locations are only seldom obtained over the laminate, and are a consequence of very local overlap pattern being superimposed favourably. When comparing this to the smeared profiles, then the maximum thicknesses are spread out and are not related to the local overlap formation, and in consequence provide a smoother but lower magnitude distribution. This fact is corroborated by the average thickness obtained in both the discrete and smeared approximation being very close, replicating the global trends. The influence of the discrete thickness peak is assessed in the simulation by the combination of both an increased amount of elements and sampling points.

Table 8.4: Particular value comparison between the discrete and smeared thickness.

	t_{max} [mm]		$t_{average}$ [mm]		Relative error of
	Discrete	Smeared	Discrete	Smeared	the average thicknesses [%]
Case 1	1.02	0.66	0.57	0.57	0.14
Case 2	1.02	0.71	0.62	0.62	0.07
Case 3	1.91	1.38	1.22	1.22	0.10

Chapter 9

Buckling Verification

With the pre-processing information from the virtual manufacturing verified, it can be used to carry out the buckling simulations. In this section, the semi-analytical model is compared and verified against FEM. In first instance, it is done separately for the smeared thickness approximation in Section 9.1, and afterwards for the discrete case in Section 9.2. Afterwards, the validity of the semi-analytical smeared approximation to the discrete FEM is done in Section 9.3. Moreover, Section 9.4 deals the with the limitation of the approximation. Finally, for all the simulations, the material properties and layups that were given in Table 8.1 and 8.2 are still used.

9.1 Smeared Simulation Convergence

First, the smeared modelling is compared between the semi-analytical and FEM simulation for the three cases. In order to do so, both simulations must first be checked for convergence. As was explained in the Section 8.3, the virtual manufacturing information is constructed with 200 sampling points and standard resolution of 300 dpi, regardless of number of elements or shape functions to find the converged parameters.

The simulation parameters are the number of elements for FEM, and both the amount of integration points and shape functions for the semi-analytical simulation. The convergence of semi-analytical method is discussed in Section 9.1.1, whereas the FEM convergence is treated in Section 9.1.2.

9.1.1 Semi-Analytical Modelling

First of all, in the current implementation of the panel package, it is not possible to select an amount of integration points lower than the number of approximation functions. The complete results of the convergence analysis of the first eigenvalue λ with different amount of integration points and shape functions for all three cases is given in Appendix C. Figure 9.1 shows the convergence study of all three cases for an equal amount of integration points than shape functions (N), with one extra integration point (N+1) and with three extra integration points (N+3). The same number of shape functions and integration points was selected in both x and y direction, since no a priori knowledge about the laminate's behaviour is known.

A first conclusion to be drawn from the data is that the results for a given number of approximation functions converge for N+1 integration points, with little variation for more integration points. This is expected, as the solution exactness increases with the amount of integration points. However, in this situation, the convergence profile does not adhere to the solution exactness rule for a polynomial

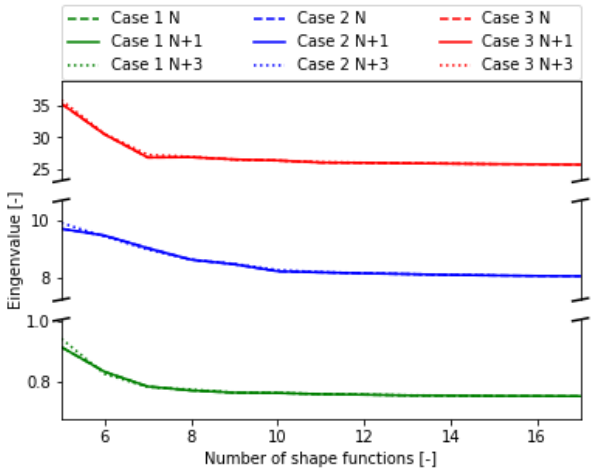

Figure 9.1: Semi-analytical model convergence of the smeared thickness cases for N, N+1 and N+3 integration points.

up to degree 2N-1, since the ABD terms are dependent on the cosine and sine of the fibre orientation θ and therefore the integrand is not a polynomial [62]. Lastly, all three cases show a good convergence profile, with case 2 requiring the most shape functions: a total of 13 shape functions and 14 integration points are needed for a convergence criteria of less than 1% change in the solution.

9.1.2 Finite Element Method

The FEM convergence is only dictated by the amount of elements. Figure 9.2 shows the first buckling eigenvalue for an increased number of elements.

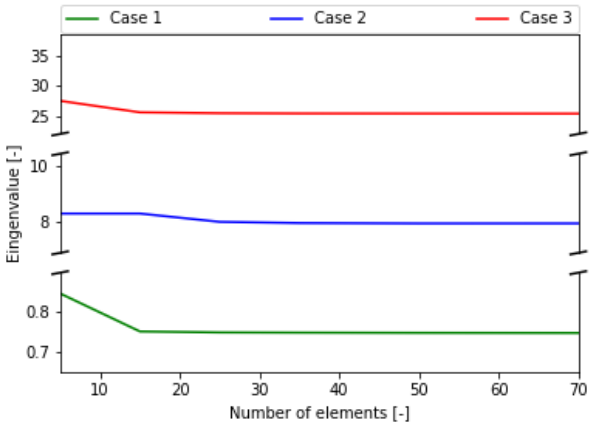

Figure 9.2: FEM convergence of the smeared thickness cases.

From this data, convergence of the model is achieved with 15 elements, regardless of the dimensions of the plate. These 15 elements simulations are finally compared to a much more refined virtual manufacturing model, to assess the influence of the sampling points to construct the elements and resolution. This refined model is created with $N_s = 1000$, a 500 dpi resolution and 100 elements. The results of this comparison are given in Table 9.1.

Table 9.1: FEM refined and converged eigenvalue comparison for the smeared thickness.

	Refined model λ [-]	Converged model λ [-]	Difference [%]
Case 1	0.75	0.75	0.6
Case 2	7.95	8.02	0.86
Case 3	25.35	25.58	0.92

Analysing the results of the comparison, it shows that the refinement of the FEM and manufacturing model has almost no influence on the buckling outcome. Therefore, it can be concluded that the virtual manufacturing parameters are sufficient to acquire the necessary information for the smeared approximation in case of a FEM analysis.

9.1.3 Discussion

The comparison between the converged first eigenvalue λ of both the semi-analytical and FEM simulation for the smeared approximation are given in Table 9.2.

Table 9.2: Converged smeared semi-analytical and FEM eigenvalue comparison.

	Discrete thickness FEM λ [-]	Smeared thickness semi-analytical λ [-]	Difference [%]
Case 1	0.75	0.75	0.19
Case 2	8.02	8.12	1.23
Case 3	25.58	25.79	0.84

It can be noted that case 2 with the free edge, usually the most complex condition to model, has the biggest relative error. However, along case 1 and case 3, the semi-analytical prediction are in good agreement with the FEM results, therefore it can be concluded that the semi-analytical model is verified, and can predict different geometries, loading and boundary conditions. Furthermore, this validates the approach taken in Section 6.1.2. Indeed, including the full ABD matrix in the buckling derivation yields a result very close to the one predicted by FEM, and that simply using an offset can predict the behaviour of one-sided thickness variation.

9.2 Discrete Simulation Convergence

As for the smeared thickness approximation, both FEM and semi-analytical buckling simulations are checked for convergence for the discrete thickness profile. A resolution of 300 dpi and 200 sampling points are still used for the baseline investigation, with again a refined case to assess the influence of these two parameters.

9.2.1 Semi-Analytical Modelling

As for the smeared semi-analytical convergence study, all the data of the convergence study is presented in Appendix C. Only the results for N, N+1 and N+3 integration points compared to the amount of shape functions is shown in Figure 9.3.

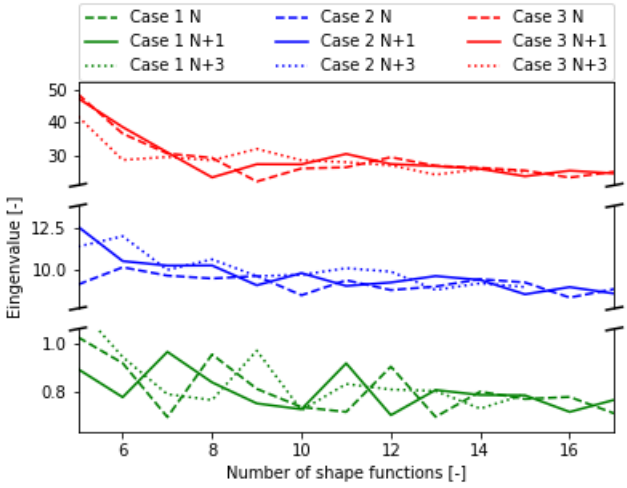

Figure 9.3: Semi-analytical model convergence of the discrete thickness cases for N, N+1 and N+3 integration points.

Looking at the results, a first ascertainment can be made: regardless of the simulation parameters used, all the results oscillate, however a trend seems to emerge, as less variation happens with higher amount of shape functions. Analysing the data further, increasing the amount of integration points for low number of shape functions, makes the result oscillate by up to 20%, due to the discontinuous thickness. As with the mass in Section 8.3, general quadrature rules performed poorly for discontinuous functions [63]. For a higher number of shape function, the solution tends to converge more yet still varies for the same reasons, but to a smaller extend as the approximation functions can better capture the displacements. Nonetheless, the required parameters for a converged semi-analytical simulation can not be predicted with certainty,therefore no refined analysis is carried out.

9.2.2 Finite Element Method

The FEM buckling eigenvalue convergence depending on the number of elements is shown Figure 9.2 for all three cases.

Analysing the FEM results, it does not suffer as much from oscillations as the semi-analytical formulation, since FEM already discretizes the problem. Using the 1% convergence criteria, convergence is attained across all three cases with 50 elements. As was discussed earlier, these converged simulations are finally compared to a much more refined virtual manufacturing model, to assess the influence of the sampling points and resolution on the element's properties. This refined model is created with $N_s = 1000$, a 500 dpi resolution and 100 elements. The results of this comparison are given in Table 9.3.

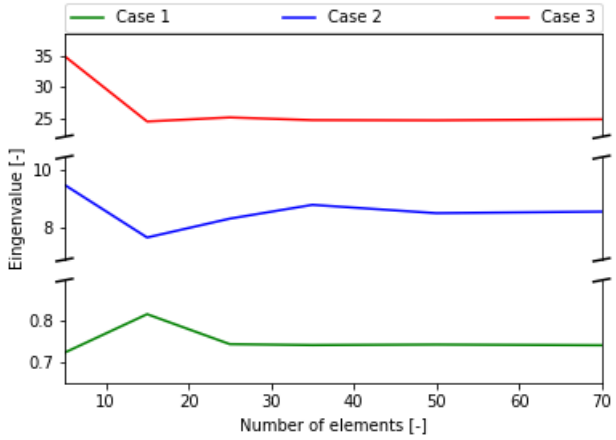

Figure 9.4: FEM convergence of the discrete thickness cases.

Table 9.3: FEM refined and converged eigenvalue comparison for the discrete thickness.

	Refined model λ [-]	Converged model λ [-]	Difference [%]
Case 1	0.74	0.74	0.11
Case 2	8.49	8.52	0.33
Case 3	24.92	24.66	-1.04

This comparison shows once again the little influence of the refinement of both parameters, and that the selected ones to compute the virtual manufacturing (300 dpi and N_s=200) are sufficient.

9.2.3 Discussion

As a conclusion, the FEM results of the discrete thickness case give a clear convergence on the number of elements to use. On the other hand, it is difficult to express parameters for a converged semi-analytical simulation, as it does not approximate the discontinuous thickness well and the result oscillates. However, despite the variation, looking at the global trend from the semi-analytical case, it does seem to approach the FEM results. Finally, a resolution of 300 dpi and 200 sampling points is enough to convey the required information for the discrete thickness to the FEM simulation.

9.3 Discussion on the Thickness Approximation

The previous section has verified the semi-analytical model for a smeared thickness, which is further compared to the discrete thickness FEM simulation in this section. Table 9.4 gives an overview of the first eigenvalue λ for each of the 3 cases by means of both the smeared semi-analytical model and the discrete thickness FEM simulation.

Table 9.4: Comparison of the semi-analytical smeared approximation model and the discrete FEM simulation eigenvalue.

	Discrete thickness FEM λ [-]	Smeared thickness semi-analytical λ [-]	Difference [%]
Case 1	0.74	0.75	1.20
Case 2	8.52	8.12	-4.71
Case 3	24.66	25.79	4.59

In order to understand and assess whether the difference is case or layup specific, another two random layups are simulated both ways for every case. These results can be found in Table 9.5. Firstly, considering all the data, the smeared modelling has a $\pm 5\%$ relative error range with respect to its discrete thickness FEM simulation counterpart, including a small contribution due to the semi-analytical model. This is a satisfactory agreement between the thickness approximation and the real case, even more for this exploratory improvement investigation.

Table 9.5: Eigenvalue comparison for the three verification cases with additional layups.

	Case 1		Case 2		Case 3	
Layup number	2	3	2	3	2	3
Smeared thickness semi-analytical λ [-]	0.71	0.77	5.68	13.23	25.89	25.07
Discrete thickness FEM λ [-]	0.70	0.77	5.84	13.54	25.92	25.03
Relative difference [%]	0.67	-0.25	-2.82	-2.27	-0.14	0.18

Secondly, the range of relative error is regarded as being intrinsic to a given layup sequence and not linked to the smeared approximation. It is assumed to stem from the influence of the local varying discrete thicknesses as opposed to the smooth smeared approximation, as was presented in Table 8.4. The global ABD component patterns are respected as was the case with the total thickness build-up of Section 8.4, however the locally different thickness will result in different ABD components. This can be of significant difference, as the B and D matrices depend respectively on the square and cubic of the thickness, alongside the fibre orientation. Coupled to the complex and interlinked relations forming the linear constitutive and geometric stiffness matrix, this leads altogether to the errors as seen in Table 9.4 and 9.5.

Further comparing the static results of the third verification cases given in Figure 9.5, 9.6 and 9.7 for respectively u, v and w displacement. The comparison of the static results of verification case 1 and 2 are given in Appendix D. These are then used as explained in Section 6.1.6 to obtain the stress resultant to compute the geometric stiffness matrix.

For each case, the displacement patterns are in good agreement. The magnitude of the displacements are in satisfactory accordance, with the in-plane ones being stiffer in the discrete FEM model, whereas it varies for the out-of-plane displacement. The relative errors of these comparisons are given in Table 9.6. The difference in magnitude is again attributed to the difference in ABD components, leading to a slightly different stiffness matrix formulation and subsequent answer for the static and buckling results.

Table 9.6: FEM and semi-analytical static analysis comparison.

	Case 1		Case 2		Case 3	
	min	max	min	max	min	max
u FEM [mm]	-3.29E-04	7.14E-05	-3.85E-04	0	-1.40E-03	7.29E-04
u semi-analytical [mm]	-3.13E-04	5.68E-05	-3.68E-04	0	-1.27E-03	6.42E-04
Difference [%]	-5.01	-20.43	-4.44	0	-9.49	-11.92
v FEM [mm]	-6.18E-04	3.22E-04	-7.97E-07	6.71E-05	0	3.17E-03
v semi-analytical [mm]	-5.71E-04	3.08E-04	0	6.32E-05	0	2.90E-03
Difference [%]	-7.60	-4.23	N/A	-5.86	0	-8.61
w FEM [mm]	-2.16E-02	8.43E-02	0	3.91E-02	-1.02E-02	6.68E-03
w semi-analytical [mm]	-1.79E-02	9.08E-02	0	4.01E-02	-9.90E-03	7.27E-03
Difference [%]	-17.05	7.72	0	2.611	-2.75	8.88

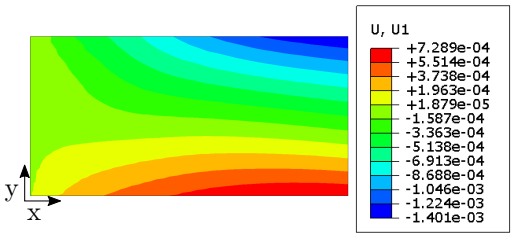

(a) Discrete thickness FEM results.

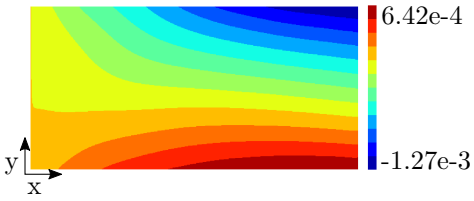

(b) Smeared thickness semi-analytical results.

Figure 9.5: Static u displacement results in mm of case 3.

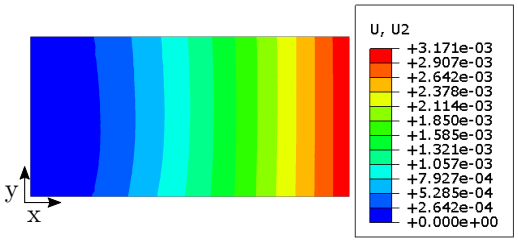

(a) Discrete thickness FEM results.

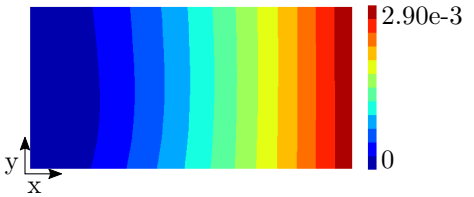

(b) Smeared thickness semi-analytical results.

Figure 9.6: Static v displacement results in mm of case 3.

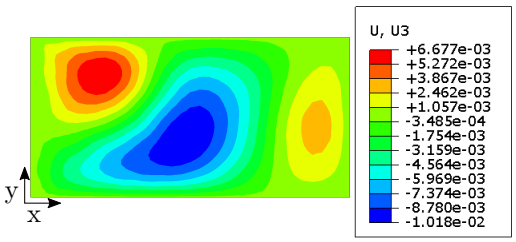

(a) Discrete thickness FEM results.

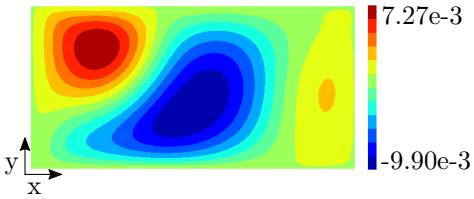

(b) Smeared thickness semi-analytical results.

Figure 9.7: Static w displacement results in mm of case 3.

The eigenmode corresponding to the first eigenvalue is also compared between the discrete thickness FEM simulation and smeared semi-analytical model in Figure 9.8, 9.9 and 9.10 for case 1, 2 and 3 respectively. Again, for all three cases, the patterns are in good agreement.

(a) Discrete thickness FEM results. (b) Smeared thickness semi-analytical results.

Figure 9.8: First eigenmode of case 1 comparison.

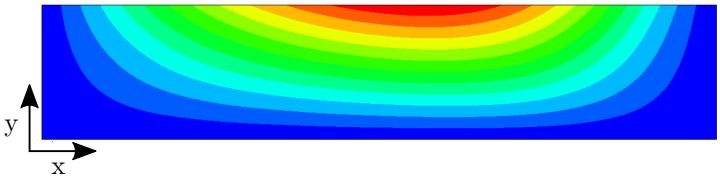

(a) Discrete thickness FEM results.

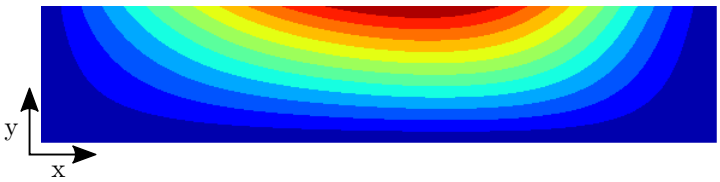

(b) Smeared thickness semi-analytical results.

Figure 9.9: First eigenmode of case 2 comparison.

(a) Discrete thickness FEM results. (b) Smeared thickness semi-analytical results.

Figure 9.10: First eigenmode of case 3 comparison.

Finally, in order to show the importance of including the overlaps in the thickness profile and subsequent analysis, a simulation is also carried out for all cases with the same layup, but assuming a uniform thickness ply. The results of this comparison are given in Table 9.7, and show a sizeable difference between both laminates.

Table 9.7: Eigenvalue of the verification cases with and without thickness build-up.

	Case 1	Case 2	Case 3
Uniform thickness semi-analytical λ [-]	0.56	4.77	14.48
Smeared thickness semi-analytical λ [-]	0.75	8.12	25.79
Relative difference [%]	-25.72	-41.23	-43.86

For all these comparisons, the manufacturing angle ϕ was restricted to 60°, as to adhere to the assumption of Section 6.1.2. However, the semi-analytical modelling uses the global angle θ to construct the ABD matrix, which can be in the range of a full 360° rotation, meaning this model is not restricted to any given angle limit.

With the eigenvalue and eigenmode in satisfactory agreement both in magnitude and pattern, it is concluded that the smeared approach is verified and can be used to characterise the discrete thickness profile obtained by overlaps of continuous AFP tows. Moreover, the smeared approximation is also the exact expression for the thickness build-up in CTS, meaning this semi-analytical model and subsequent conclusions can also be used for CTS manufactured laminates.

9.4 Tow Width Ratio Limit

The smeared thickness approach gives a good approximation for the linear buckling response of VAT laminates with discrete overlaps, however this simplified thickness profile is limited in its representation capabilities: the approximation is well suited for global responses, but local phenomena cannot be modelled, such as stress concentration, local strength and failure at and around overlap regions. These aspects should be evaluated with a refined model locally with the exact physical representation, as the smeared thickness approximation does not hold any information about tow interactions.

Furthermore, the influence of the tow width is investigated on the validity of the smeared approximation, because for larger tow widths the overlap appears within bigger distances such that the smeared approach is expected to become progressively a worse approximation. To this end, all three cases of Chapter 7 are once again evaluated with a discrete thickness FEM analysis for different tows widths. The results are shown in Table 9.8, and the relative difference with their respective smeared eigenvalue in Table 9.9.

Table 9.8: Buckling eigenvalue for different tow widths.

	Tow width [mm]							
	3.175	6.35	25.4	40	65	100	175	350
Case 1 λ [-]	0.73	0.74	0.74	0.74	0.75	0.76	0.76	0.77
Case 2 λ [-]	8.57	8.52	8.40	8.50	8.58	8.72	8.79	8.14
Case 3 λ [-]	24.65	24.66	25.03	24.48	25.63	25.61	25.63	25.23

Table 9.9: Buckling eigenvalue relative error for different tow widths compared to the smeared approximation.

	Tow width [mm]							
	3.175	6.35	25.4	40	65	100	175	350
Case 1 λ [-]	-3.04	-1.19	-1.71	-1.81	-0.35	0.62	1.07	1.80
Case 2 λ [-]	5.63	4.95	3.48	4.75	5.74	7.46	8.27	0.35
Case 3 λ [-]	-4.45	-4.39	-2.97	-5.08	-0.62	-0.72	-0.62	-2.20

The relative difference of Table 9.9 does not show the expected deterioration between the discrete thickness FEM simulation and smeared semi-analytical answer. Despite the lack of the apparent influence of the tow width, it is still assumed that the smeared approximation is not valid. In case of larger tow width ratios compared to the dimensions of the laminate, the angle interpolation is not valid anymore to predict the local orientation. When large tows are used, fibres far away from the centreline can be approximated by a linear angle variation of a bent Euler-Bernoulli beam. This is opposite to the one obtained from the interpolation scheme, which can be of a higher order, and in extreme examples have large differences or an opposite sign. On the contrary, when the tow width is small compared to the plate dimensions, the sampling points are spaced further apart than the tow width, meaning that the centreline angle variation follows the interpolation scheme.

Furthermore, the same arguments hold for the discrete case: the interpolation scheme gives the centreline orientation ϕ, used to construct the virtual manufacturing model, which will result in the tows to be well plotted and represent the overlap locations accurately. This thickness information is then retrieved at the sampling points, where however the orientation transmitted along is still dictated by the interpolation scheme and sampling point location, and does not take into account the bending for large tow ratios. This incorrect associated orientation would then still lead to a different stiffness and erroneous result for large tow width ratios.

Therefore, the effect of the tow width on the validity of the thickness approximation cannot be fully described by the current framework, since the exact fibre orientation is badly predicted for larger tow width ratios. No threshold could be set concerning a maximum tow width ratio, but since the sampling distance in the verification cases corresponds closely to the tow width, the tow width effect does not have consequences on the aforementioned conclusions in this report. However, further investigations should be carried out with a detailed angle model taking the fibre bending into account to assign the orientation to sampling points covering the tow located at a large distance from the centreline.

Chapter 10

Optimisation

This chapter treats the optimisation results of the three cases with the different layup configurations as presented in Chapter 7. First of all, regarding the third layup configuration, which tries to achieve a symmetrical and balanced behaviour by constraining the magnitude of the relevant coupling terms, the optimisation was not successfully and computational more expensive, since the magnitudes had to be checked for each of the sampling points. It yielded results 30-40% off the other optimum solutions, as the offset created by the varying thickness profile was not enough to create an artificial symmetrical and balanced behaviour. Therefore this layup configuration was not investigated further and is not mentioned for any of the cases. The remaining layup configuration possibilities are defined as follow:

- Uniform determined: a uniform thickness profile, attained with a cut and restart capability or gap strategy, and a layup sequence constrained to the symmetric and balanced rules.
- Uniform free: a uniform thickness profile, attained with a cut and restart capability or gap strategy, with no restriction on the layup sequence.
- Smeared determined: a smeared thickness profile, accounting for overlaps' formation, and a layup sequence constrained to the symmetric and balanced rules.
- Smeared free: a uniform thickness profile, accounting for overlaps' formation, with no restriction on the layup sequence.

The symmetry and balanced rules are implemented by stacking a positive and negative ply definition next to one another, and mirroring it all at the layup centre. In case of the extra ply for the uniform case, it is added at the midplane to keep the symmetry. A negative orientation is achieved as given in Equation 10.1, where $-\phi$ is obtained by using the $-\phi_m$ in the interpolation scheme.

$$-\theta = -(\phi - \chi) = -\phi - (-\chi) \tag{10.1}$$

Concerning the added ply in case of the uniform design, it had to be implemented in such a way, to keep the mass ratio constraint as low as possible. When large ratios were allowed, the smeared variable thickness optimisation would only add nearly straight fibres with a high manufacturing angle ϕ. This is the most beneficial, as it adds the most thickness globally. This is expected, since the buckling results are mostly dependent on the D matrix in case of a symmetric and balanced layup, which scales with the cubic of the thickness [32]. For other unsymmetrical and unbalanced layups, the A and B matrix also have an influence in the result, but the effect of the D matrix is still present as well. This defeats the purpose of the variable thickness working locally along the stiffness increase, and it would be easier to just add extra plies.

The variables consist of one rotation angle χ and four interpolation angles ϕ_m located at 0%, 33%, 66% and 100% respectively. This yields a total of five variables per distinct ply, which already defines four plies in case of a determined layup. Furthermore, the presented results are the best solutions found starting from different initial guesses to increase the confidence in obtaining the global optimum, but cannot be affirmed with certainty. The layup corresponding to each optimised result and case is given in Appendix E.

Finally, for all the smeared thickness layup, the mass constraint of the smeared approach is used to the full extend, meaning all results are given at isomass. Moreover, for all the layup answers presented next, either the uniform or smeared thickness case, at least one of the plies is constrained by the steering curvature limit.

10.1 Case 1

The best result of the optimisation for each layup configuration of case 1 is given in Table 10.1. Analysing the results shows that a free and unconstrained layup sequence improves slightly the buckling eigenvalue for both the smeared and uniform approach over their symmetric and balanced ruled counterpart. Moreover, the smeared variable thickness laminate results in a little improvement of the buckling eigenvalue for both layup configurations compared to the uniform thickness case. Looking in more detail at the smeared results, the thickness profile for both the determined and free layup are given in Figure 10.1 and 10.2 respectively.

Table 10.1: Case 1 eigenvalue optimisation results.

	Uniform thickness	Smeared thickness	Difference [%]
Determined layup λ [-]	2.04	2.06	1.33
Free layup λ [-]	2.07	2.08	0.77
Difference [%]	1.47	0.92	

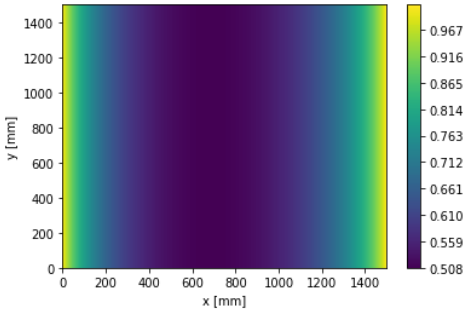

Figure 10.1: Smeared thickness distribution for the optimal determined layup of case 1.

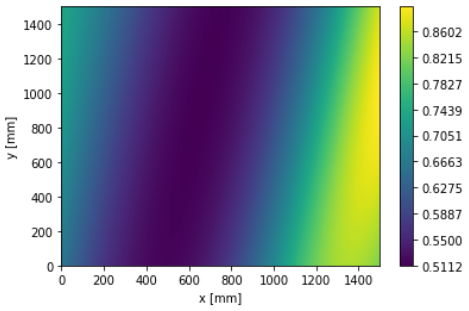

Figure 10.2: Smeared thickness distribution for the optimal free layup of case 1.

It was noted that whilst investigating all optimisation results, the balanced part of the determined layup is not satisfied for plies with a rotation angle χ. Trying the method as given in Equation 10.1, a negative fibre orientation is indeed obtained, as shown in Table 10.2. However, the location of these opposite orientations is not concurrent on the laminate. As shown graphically in Figure 10.3, when χ

is positive, then ϕ_1 is only obtained in the top left corner due to the rotation of the manufacturing coordinate system and CP relocation. The normal line passing through the bottom left corner is already at a distance $\Delta x'$ from the left top corner, meaning a different orientation, ϕ_c, is obtained from the interpolation. Thereafter, ϕ_1 and ϕ_c must be readjusted to the global coordinate system by analogy of Equation 10.1, to obtain θ_1 and θ_c.

Table 10.2: Global fibre orientation for the different signs of the rotation and manufacturing angle.

	ϕ	χ	θ
$\theta = \phi - (\chi)$	30	45	-15
$\theta = \phi - (-\chi)$	30	-45	75
$\theta = -\phi - (\chi)$	-30	45	-75
$\theta = -\phi - (-\chi)$	-30	-45	15

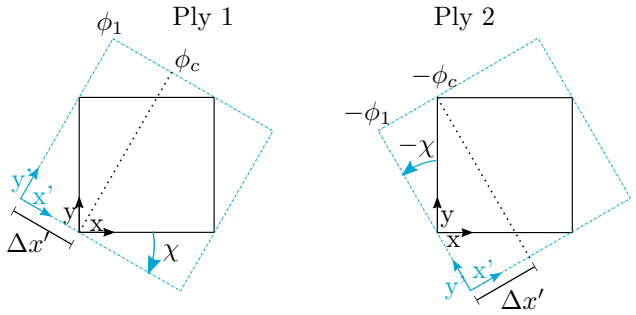

Figure 10.3: Formation of an unbalanced layup.

Moving to the second layer, with a $-\chi$ rotation and negative fibre interpolation as suggested by Equation 10.1, the manufacturing coordinate system is rotated again, and this time starts at the bottom left with the $-\phi_1$ fibre orientation, as shown in Figure 10.3. Again, the normal line to the variation axis passing through the top left corner is at the same distance $\Delta x'$ from the right top corner, the same as for the first ply, resulting in the same $-\phi_c$ value. Applying the global rotation, the angles are found to be $-\theta_1$ and $-\theta_c$ as expected, being the opposite of the first ply. However, θ_1 from the first ply is located at the top left, which coincides with $-\theta_c$ from the second ply. For the bottom right corner, the fibre orientations will be θ_c and $-\theta_1$. This shows that a balanced layup can not be obtained with the current framework with the inclusion of the rotation angle, unless χ equals $0°$ or $180°$. Alternatively, the negative orientation $-\theta$ could just be assigned from the positive θ of the previous ply at each location, and work with Equation 10.1 backwards to find the manufacturing angle and subsequent thickness. However this last option was not included to keep a fair comparison with the uniform layup configuration, as this latter one is already unbalanced due to the added ply.

However, even with a rotation angle different from the four mentioned above, the smeared thickness pattern will be symmetric about the global x axis. Indeed, both top and bottom left corners have one ply with a fibre orientation of $|\phi_1|$ and $|\phi_c|$, and will result in the same total smeared thickness since it only is depends on the cosine of the angle. This also holds true for any other point on the laminate.

The same rotation algorithm was also used for the uniform case, but with the inclusion of the extra ply, both the determined and free layup configuration were already set not to be balanced, and therefore the algorithm was not changed for those layup sequences.

Moving on to the optimisation results of Table 10.1, the optimal determined smeared layup configuration corresponds to a zero rotation angle χ, and is therefore balanced and symmetric in the layup sequence. However, this does not mean that the B matrix vanishes: due to the offset and the variable thickness, the B matrix is present for the determined smeared layup, as it squares with the trough-the-thickness location, alongside the fibre orientation. If it is also balanced, such as this optimum, then A_{16} and A_{26} are zero, as these only depend on the relative thickness of a fibre direction, and are not influenced by the through-the-thickness location. Moreover, B_{16} and B_{26} are also zero. All the other terms of the ABD matrix are mirrored about $y = 750$ mm. An overview of the extreme values for each ABD term of the optimum smeared determined layup is given in Table 10.3.

Table 10.3: ABD components extreme values for the symmetric and balanced smeared laminate of the optimum of case 1.

	Value [N/mm]			Value [N]			Value [Nmm]	
	Min	Max		Min	Max		Min	Max
A_{11}	24027	92359	B_{11}	0	6111	D_{11}	1926	3622
A_{12}	1473	33417	B_{12}	0	8363	D_{12}	32	4955
A_{16}	0	0	B_{16}	0	0	D_{16}	-1316	1322
A_{22}	5256	111065	B_{22}	0	28164	D_{22}	113	16687
A_{26}	0	0	B_{26}	0	0	D_{26}	-3548	3547
A_{66}	3659	37435	B_{66}	0	9470	D_{66}	79	5610

This comparison shows the relative magnitude of the different ABD terms. The B matrix terms are not small anymore, meaning the laminate's analysis can not be uncoupled between the in-plane and out-of-plane problem, and consequently this is the reason for the inclusion of all ABD terms in the buckling problem. If a rotation angle χ were to be present, resulting in an unbalanced stacking sequence, then A_{16}, A_{26}, B_{16} and B_{26} are present and anti-symmetric about $y = 750$ mm. The other A and B terms are still mirrored symmetrically about $y = 750$ mm, whereas the D matrix components do not show any symmetric distribution.

The higher buckling eigenvalue of the free smeared case is assumed to be a consequence of the rotation angle and unbalanced layup restriction: there is a more optimal answer with a rotated balanced layup, but it cannot be found by the unbalanced determined case, hence the free layup configuration approaches it better. This is also supported by the presence of the rotation angle in the smeared free layup configuration. Therefore, to check the previous statement, the smeared free layup configuration is also optimised with the restriction $\chi = 0°$. This optimisation result should approach or even match the determined layup, as this latter one represents a symmetric answer to the problem, and can therefore be judged as optimal.

This optimisation resulted in $\lambda = 2.04$, with the associated thickness distribution shown in Figure 10.4 and the layup given in Appendix E. The layup was not matched as predicted beforehand, as the design space with the free layup is much larger due to the higher amount of variables, resulting in a more difficulty finding the best optimum.

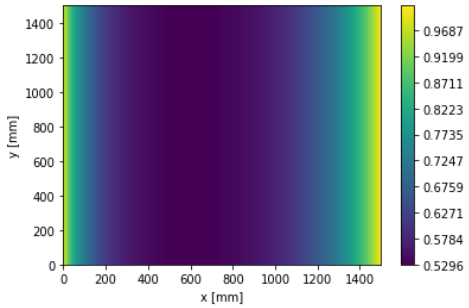

Figure 10.4: Smeared thickness distribution for the free layup of case 1 with $\chi = 0$.

Concerning the uniform thickness results, the determined layup is not balanced, as explained earlier, however symmetric, with a zero B matrix. Moreover, the optimum for this configuration has a zero rotation for each ply, resulting in a symmetrical ABD component distribution about $y = 750$ mm. This is an expected behaviour to a symmetric problem. Moreover, the free layup for the uniform case obtains a slightly higher eigenvalue than the determined layup, still with the rotation angle χ zero for each layer, however also with the presence of B matrix terms. These B coupling terms can add stiffness to the laminate, by lessening out-of-plane displacement due to the in-plane constraints, and help improve the buckling capabilities.

10.2 Case 2

The results of the different optimised layup configurations of case 2 are given in Table 10.4. In this case, no symmetry is present is the problem, since the boundary conditions differ on the right and left side, but also at the top and bottom edge.

Table 10.4: Case 2 eigenvalue optimisation results.

	Uniform thickness	Smeared thickness	Difference [%]
Determined layup λ [-]	25.92	21.84	-40.63
Free layup λ [-]	33.85	36.32	7.31
Difference [%]	30.58	66.30	

Analysing the results, the smeared determined layup gives a much smaller optimal answer than uniform determined case. This can be explained by the symmetry of the thickness profile, regardless of the rotation angle, as shown in Figure 10.5. Due to this, thickness is also added near the free edge where little load is redirected, and makes for an inefficient design, however inherent to the layup configuration. On the contrary, the extra ply and thickness of the uniform determined case gives a better result, as the D matrix scales cubic.

Looking at the free layup configuration, it provides an increase in buckling load for both uniform and smeared case, as would be expected for an unsymmetrical problem, since it allows for a wider and unsymmetrical tailoring capability. The free smeared solution has the biggest improvement over its determined layup configuration, as not only the fibre orientation and layup can be unsymmetrical, also the thickness. At the right side, the gradual increase in thickness from the bottom to the top works in hand with the increase in stiffness, in order to redirect all the loading towards the supported

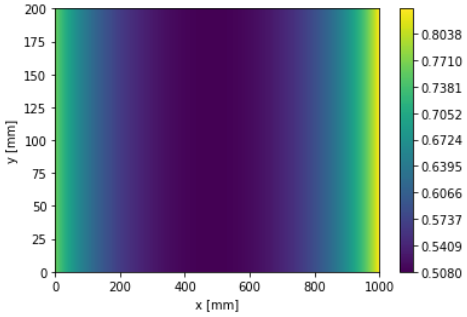

Figure 10.5: Smeared thickness distribution for the optimal determined layup of case 2.

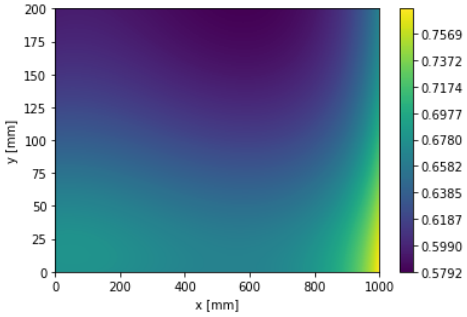

Figure 10.6: Smeared thickness distribution for the optimal free layup of case 2.

bottom edge. This trend is extended over the whole length of the restricted edge, where the bottom is made thicker and stiffer to cope with the redirected load. Finally, at the left side, the displacement is restricted in x, and therefore the reaction force can vary. This is why the thickness and stiffness increase is only concentrated to the bottom part, since it already comes from the bottom edge, and must not be directed to the top.

Although the lowest thickness is near the free edge, the is still thicker than the nominal four ply thickness. This is because when a rotated ply is used to achieve a global orientation with increased thickness, then that thickness increase is also spread in the shifting direction to other locations.

10.3 Case 3

The best result of the optimisation for each layup configuration of case 3 is given in Table 10.5. Due to the shear loading, this case is also unsymmetrical. The thickness distribution for both smeared methods is shown in Figure 10.7 and 10.8.

Table 10.5: Case 3 eigenvalue optimisation results.

	Uniform thickness	Smeared thickness	Difference [%]
Determined layup λ [-]	40.34	37.96	-5.90
Free layup λ [-]	43.40	45.47	4.77
Difference [%]	7.59	19.78	

Concerning the smeared variable thickness optimisation, as for case 2, the smeared determined layup configuration performs worse than the uniform determined layup, since the thickness must is distributed symmetrically as shown in Figure 10.7. However, the smeared free layup is much more performant than the smeared determined layup configuration, because the free layup can be better tailored to the unsymmetrical problem, allowing for the thickness change to work in synergy with the variable stiffness to achieve the improvements. When looking at the thickness distribution of the smeared free layup in Figure 10.8, then the line of increased thickness aligns with the expected compression line due to the shear, which will be altered by both normal loadings, but is shifted towards the right edge as a consequence of the stiffer clamped left edge.

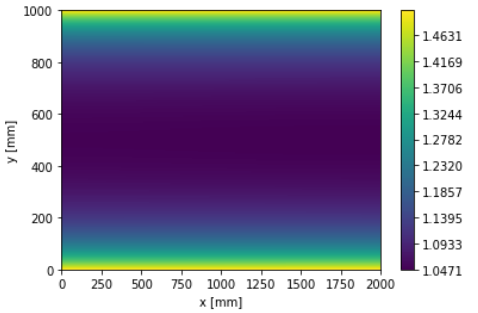

Figure 10.7: Smeared thickness distribution for the optimal determined layup of case 3.

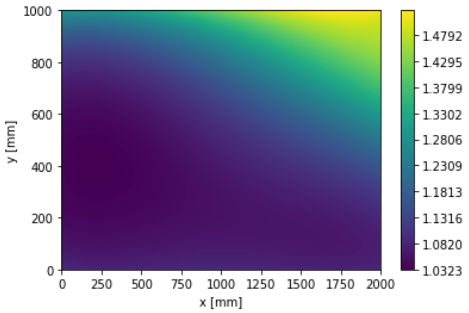

Figure 10.8: Smeared thickness distribution for the optimal free layup of case 3.

Similarly, the uniform free layup configuration performs better than the determined one, as again it allows for a better stiffness distribution suited to the unsymmetrical conditions. However, analogously to case 2, the smeared variable thickness VAT laminate provides a better solution with a higher buckling capability than the uniform thickness VAT laminate.

10.4 Discussion

With all the results presented and analysed, several trends can be observed and are detailed next. First, it must be noted that this was a comparison of unconventional layups sequences, partially since no balanced layup sequence could be included, except in special conditions, but also because the B matrix is present due to the one-sided variable thickness. However, it is believed to still represent the trend offered by variable thickness over their uniform counterparts.

In these conditions, the variable thickness laminates provided a higher buckling load than their isomass uniform thickness counterpart for a free layup configuration. Especially in unsymmetrical conditions, where the thickness increase could be tailored to the desired location along with the fibre orientation, the variable thickness laminates show good improvements. The use of a two dimensional angle interpolation is believed to even increase further these improvements in unsymmetrical cases, since the thickness can be tailored more locally. Further research should also be conducted into including balanced stacking sequences, which is expected to result in slightly better answers for case 1, as then a large symmetric solution space is possible with a rotation angle χ for both the smeared and uniform thickness profile.

This optimisation was an early numerical investigation into the benefits of variable thickness, where the buckling eigenvalue was maximised. However, for the reversed problem where the mass must be minimised for a given loading, the variable thickness is believed to lead to lighter designs. The current study shows similar performance in symmetric conditions, but where a uniform case can only have its mass vary in discrete steps as plies are added or removed. Variable thickness laminates on the other hand, are able to have a more continuous change in their mass, since it depends on the manufacturing angle ϕ. The main drawback of the one-sided thickness variation, is the coupling between in-plane and out-of-plane effects, whether it is modelled with the ABD offset or a shell formulation.

Looking at the optimisation constraints, both the manufacturing angle and steering curvature restrained the outcome. An angle of 60° was used for both the smeared and uniform laminates, however is not entirely representative. For the uniform case, there is no physical reason to constraint it, whereas for the smeared case, it is linked to the model assumptions, but manufacturing-wise it could also be

higher. With the angle limit in practise being larger, it is expected that the optimal answers presented for all cases would be higher, however further research should be conducted to quantify the gains.

Secondly, considering the fibre steering limit, it can be improved for the variable thickness case. The current curvature constraint is linked to the AFP manufacturing process, but the smeared expression also defines the exact thickness profile obtained by means of CTS. This latter method has a relaxed steering limit, as discussed in Section 2.3.2, which plays an especial important role for smaller laminate dimensions, by offering a larger design space compared to AFP, whose constraints can not be relaxed. This would lead to the variable thickness exhibiting even higher performance difference over the uniform case than the margins presented in this work. To this extent, the free smeared layup of case 3 is optimised with a curvature limit equal to ten times of that of AFP. The result is given in Table 10.6, with the layup in Appendix E, and shows a substantial gain. When looking at the CTS thickness profile displayed in Figure 10.9, a similar distribution trend is obtained as the optimum AFP. Alternatively, the uniform profile can also be attained with a higher curvature constraint by means of Tailored Fibre Placement (TFP), which instead varies the matrix and fibre volume ratio to keep a uniform ply thickness [64]. However, the varying stiffness properties can not be modelled in this framework.

Table 10.6: Relaxed CTS steering constraint results compared to AFP for the smeared free layup configuration of case 3.

	AFP smeared free	CTS free	Difference [%]
Eigenvalue λ [-]	45.47	50.08	9.21

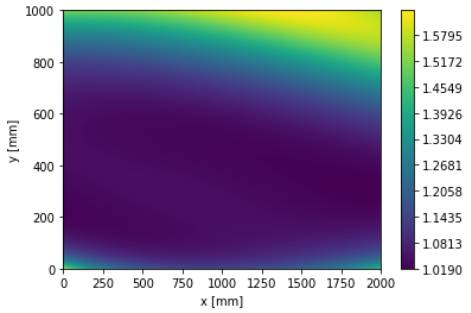

Figure 10.9: Smeared thickness distribution for the free layup of case 3 with CTS curvature constraints.

Moreover, the present models do not consider design guidelines, such as blending, nor does it look at inter-laminar shear stress or pell-off tendency in the layup layup sequence. The influence of these aforementioned effects should be further investigated on the optimal answers, and practical performance gains.

Lastly, a mention regarding literature is made, where the buckling increase with overlaps is suggested. The gains seen in this research are nearly not as high as the one presented. The mentioned work [10] mass normalised the improvements without taking the non-linear thickness influence on the solution into account, which is influenced by the cubic of the thickness by means of the D matrix in constant thickness laminates [32], resulting the lower improvements at isomass.

Chapter 11

Buckling Formulation Comparison

As a last part, the most optimal layups obtained for the free smeared configuration are also simulated with a shell element in FEM, for both discrete and smeared case. This is to allow the comparison with the plate results, and address the discussion of Section 6.1.2.

The FEM model was again created with a scripted input file to transfer the variable stiffness information to the elements. However, the midplane allocation happens in a different manner: no offset is used in the midplane definition of the element, but rather the nodes are placed on the geometrical midplane with a respective z axis distance. This distance is obtained from the physical midplane of the sampling point layup closest to each node location. Afterwards, the layup assign to the element is also retrieved from the closest sampling point to the centroid, as was the case for the plate FEM of Section 6.2. The results of these simulation and comparison with the plate results is given in Table 11.1.

Table 11.1: Comparison of the buckling formulation for the smeared free optimised results.

	Discrete thickness shell FEM λ [-]	Smeared thickness shell FEM λ [-]	Discrete thickness plate FEM λ [-]	Smeared thickness plate FEM λ [-]	Smeared thickness semi-analytical λ [-]
Optimum case 1	2.11	2.05	2.01	2.05	2.08
Optimum case 2	36.30	35.22	35.22	35.24	36.32
Optimum case 3	44.75	46.37	44.75	46.35	45.47

Looking at this data, for the optimal layups for each case, the smeared offset semi-analytical method does approximate well the FEM counterpart as was discussed in Section 9.1. More importantly, it seems that for these particular cases, that the semi-analytical model also approximates well the buckling eigenvalue with a shell formulation, which is the other method suggested by Groh and Weaver [41]. This would seem to confirm the approach taken in this thesis by limiting the manufacturing angle to 60° along the offset in the ABD matrix and a plate deformation in modelling the buckling behaviour of variable thickness variable stiffness laminates, however more research should be conducted if a higher manufacturing angle is desired.

Chapter 12

Conclusion

The purpose of this thesis was twofold: firstly model and approximate the thickness profile of Variable Angle Tows (VAT) due to the Automated Fibre Placement process and incorporate its influence on the linear buckling response in a semi-analytical model. Secondly, investigate the possible benefits offered by a varying thickness profile along VAT by optimising and comparing both uniform and with thickness variation laminates.

The first part consisted in virtually replicating the manufactured laminate: in order to represent VAT, a one dimensional Lagrange interpolation scheme was used to obtain the fibre orientation distribution, allowing for possible complex definitions with few variables. It was observed that including a ply rotation involved a distinct influence on the thickness distribution, and must be considered alongside the steering angle. The tow paths are obtained from the fibre orientations, which are subsequently plotted graphically with a given opacity in a repeat unit concept. As a result of the one dimensionality of the angle variation, any location on the laminate can be retraced inside this unit to retrieve information about the discrete thickness due to overlaps.

Furthermore, a smeared thickness approximation suggested by literature is introduced, which is used to approximate the discrete thickness characteristics for buckling simulations. The approximation expresses the local thickness in a continuous way based solely on the local manufacturing angle. Both the discrete and smeared method incorporate a procedure to determine the fibre curvature at distinct locations over the laminate, directly derived from the interpolation scheme, so that the chosen fibre variation can be checked against manufacturing limits. Finally, a mass prediction of the laminate is added to the virtual manufacturing method.

The semi-analytical buckling simulation is based on the classical Kirchhoff-Love plate kinematics, where an offset is incorporated into the ABD calculations to represent the varying thickness and midplane profile, albeit limited to a manufacturing angle of $60°$. The general eigenvalue problem is derived from the Neutral Equilibrium Criterion, by taking all the ABD terms into account. The displacement fields are solved by means of the Ritz method, with Legendre polynomial shape functions incorporating different boundary conditions through enrichment functions and the internal stress resultants are obtained from a static equilibrium simulation.

The verification of the virtual manufacturing methodology was divided in different parts. First, the curvature calculation implementation was verified against a different approach taken from literature, and yielded a similar results. Moreover, the repeat unit concept was found to be good at providing the required local information on a small scale, but numerical errors arise for large dimensions, from remapping outer location into the repeat unit. This resulted in a distorted graphical representation for narrow overlap regions linked to small manufacturing angles. However, it was deemed to be of little

effect since it is a local phenomena and the mass prediction coincided for the comparison between the discrete and smeared thickness modelling. The last step in verifying the virtual manufacturing method, was to compare the overall thickness pattern, showing a good agreement, with similar locations and shape of thickness build-up.

With the pre-processing information verified, the buckling analysis and thickness approximation validity was investigated. In a first instance, the semi-analytical model was verified against Finite Element Modelling (FEM) for three distinct cases, each one with different geometries, loading and boundary conditions. This was done based on the smeared approximation with a random variable stiffness layup, and showed good agreement between both simulation methods. Thereafter, the discrete thickness profile was also modelled with both the semi-analytical modelling and FEM, with the first method experiencing convergence issues due to the discontinuous thickness with the numerical integration. The latter FEM however did give converged results, which were in satisfactory agreement with the semi-analytical outcome of the smeared approximation, in both the buckling eigenvalue and corresponding eigenmode.

Moreover, the validity of the smeared thickness approximation was examined for a range of tow widths. Despite all the tow width simulations providing a similar eigenvalue for each case, the validity could not be confirmed for large tow widths and is strongly doubted. The predicted angles by means of the interpolation scheme would no coincide with the actual orientation along the bent fibre anymore. This requires further analysis with a more refined model to quantify the difference extend, and therefore no tow width ratio threshold could be established.

Afterwards, gradient based optimisations are carried out for the three verification cases, to assess possible benefits of variable thickness VAT laminates over uniform thickness ones. All cases were subjected to a common steering curvature limit and an equal mass constraint, either by the addition of plies or the maximum thickness build-up. Due to this added ply and the shortcomings of the current framework, balanced layups could not be constructed, except in special cases. Coupled to the influence of the B matrix, which is always present with a one-sided thickness profile, this resulted in unconventional laminate solutions. For unsymmetrical loading and boundary conditions, the variable thickness option with an unrestricted layup sequence showed a sizeable gain over its uniform thickness counterpart, as the thickness build-up could work in hand with the stiffness and load redistribution mechanisms. On the contrary, with a layup constrained to be unbalanced and symmetric, the uniform thickness VAT laminate performed better compared to the variable thickness case, where the thickness still had to be distributed symmetrically and therefore hindering the synergy with the stiffness tailoring. The symmetric problem did not exhibit similar gains, the variable thickness only being marginally better for both layup configurations. It is recommended to investigate the possibilities further by incorporating a balanced layup, but also by including engineering guidelines.

Lastly, each optimal solution for the smeared thickness cases is compared to a FEM with a shell formulation, as suggested by literature. The shell model would be better at representing the buckling behaviour, but the current results are found to be in good accordance with the shell FEM results.

Chapter 13

Recommendations

Following the results and experience gathered during this thesis, a series of recommendations is set out for future improvements and research possibilities. First of all, this complete thesis was solely based on numerical work, therefore it could use experimental data to validate the virtual manufacturing process in first instance, followed by the stiffness and eigenvalue prediction of the proposed methodology, with both discrete and smeared thickness modelling.

Nonetheless, regardless of the plate model validation for the variable thickness profile, the approach taken in this work could be improved upon by extending the formulation to shell elements. Depending on the experimental validation outcome, it would not only increase the manufacturing angle range, restricted to 60° with a plate element, but possibility also predict more accurately the buckling behaviour of one-sided thickness build-up variable stiffness laminates.

Furthermore, as the fibre orientation given by the interpolation is doubted to be correct for large tows with respect to the laminate's dimensions, further research should be conducted into the validity of the smeared approximation for these conditions. A more detailed model, involving the fibre orientation through the tow width as it is bent in AFP, should be used to assign the local layup in the analysis.

Afterwards, the current framework for a ply rotation requires the Lagrange interpolation to be equally rotated and adapted to the manufacturing area dimensions, which resulted in the spatial variation of the interpolated angles and thicknesses for the same interpolation values. Therefore, other interpolation scheme could be explored, which do not depend on a regular grid and would therefore not require the remapping or rotation of the coordinate system, and distort less spatially the outcome.

A buckling analysis is a global structural response, but the proposed model and approximation do not take into account any local phenomena. The effect of the overlaps should be characterised, either in terms of resin pockets formation or stress field at the overlaps resulting from tow drops and out-of-plane contribution. Moreover, the interlaminar shear stresses or peel off tendencies should be considered into defining the variable stiffness layup through adequate definition the interpolation values.

This optimisation was a first investigation into the possible benefits of considering variable thickness along the optimisation of variable stiffness laminates, and was meant to see if improvements are feasible. However, these optimisation results omit several points. The first one being the symmetric layup sequence not being possible in the current framework, and therefore not finding the most optimal solution in most of the cases. This must be remedied with a balanced formulation, either through a different interpolation scheme as was already explained, or reassign the opposite fibre orientation to the nodal location. Secondly, engineering guidelines were not considered, and should be incorporated into the optimisation to acquire feasible and sound designs.

Moreover, as was suggested for the unsymmetrical loading conditions of optimisation case 2, implementing a two dimensional fibre orientation variation could result in higher improvements of the buckling capabilities. A two dimensional interpolation scheme gives more freedom in the tailoring possibilities, with an even better distribution of the stiffness and thickness were they are required, or adversely, where they do not contribute much to the increase of performance.

Finally, this research shows promises for benefits of variable stiffness variable thickness laminates on the linear buckling behaviour. Further analysis should be conducted to investigate if the the varying thickness profile can also improve the post-buckling capabilities of variable stiffness laminates.

Bibliography

[1] S. Yau and T. Chou, "Strength of woven-fabric composites with drilled and molded holes," in *Composite Materials: Testing and Design (Eighth Conference)* (J. Whitcomb, ed.), pp. 423–437, 1988.

[2] S. B. Biggers and S. Srinivasan, "Compression buckling response of tailored rectangular composite plates," *AIAA Journal*, vol. 31, no. 3, pp. 590–596, 1993.

[3] P. J. Crothers, K. Drechsler, D. Feltin, I. Herszberg, and T. Kruckenberg, "Tailored fibre placement to minimise stress concentrations," *Composites Part A: Applied Science and Manufacturing*, vol. 28, no. 7, pp. 619–625, 1997.

[4] Z. Wu, P. M. Weaver, and G. Raju, "Postbuckling optimisation of variable angle tow composite plates," *Composite Structures*, vol. 103, pp. 34–42, 2013.

[5] T. R. Brooks and J. R. R. A. Martins, "On manufacturing constraints for tow-steered composite design optimization," *Composite Structures*, vol. 204, pp. 548–559, 2018.

[6] S. Honda, Y. Narita, and K. Sasaki, "Maximizing the fundamental frequency of laminated composite plates with optimally shaped curvilinear fibers," *Journal of System Design and Dynamics*, vol. 3, no. 6, pp. 867–876, 2009.

[7] L. Parnas, S. Oral, and U. Ceyhan, "Optimum design of composite structures with curved fiber courses," *Composites Science and Technology*, vol. 63, no. 7, pp. 1071–1082, 2003.

[8] Z. Guerdal, B. F. Tatting, and C. Wu, "Variable stiffness composite panels: Effects of stiffness variation on the in-plane and buckling response," *Composites Part A: Applied Science and Manufacturing*, vol. 39, no. 5, pp. 911–922, 2008.

[9] A. Blom, P. Stickler, and Z. Guerdal, "Optimization of a composite cylinder under bending by tailoring stiffness properties in circumferential direction," *Composites Part B: Engineering*, vol. 41, no. 2, pp. 157–165, 2010.

[10] Z. Wu, P. M. Weaver, G. Raju, and B. Chul Kim, "Buckling analysis and optimisation of variable angle tow composite plates," *Thin-Walled Structures*, vol. 60, pp. 163–172, 2012.

[11] T. A. M. Guimarães, S. G. P. Castro, C. E. S. Cesnik, and D. A. Rade, "Supersonic flutter and buckling optimization of tow-steered composite plates," *AIAA Journal*, vol. 57, no. 1, pp. 1–11, 2018.

[12] S. Setoodeh, M. M. Abdalla, and Z. Guerdal, "Design of variable-stiffness laminates using lamination parameters," *Composites Part B: Engineering*, vol. 37, no. 4, pp. 301–309, 2006.

[13] G. G. Lozano, A. Tiwari, C. Turner, and S. Astwood, "A review on design for manufacture of variable stiffness composite laminates," *Proceedings of the Institution of Mechanical Engineers, Part B: Journal of Engineering Manufacture*, vol. 230, no. 6, pp. 981–992, 2015.

[14] H. B. de Quadros and J. A. Hernandes, "A Lagrange parametrization for the design of variable stiffness laminates," *Structural and Multidisciplinary Optimization*, vol. 58, no. 1, pp. 129–137, 2018.

[15] J. M. J. F. van Campen, C. Kassapoglou, and Z. Guerdal, "Generating realistic laminate fiber angle distributions for optimal variable stiffness laminates," *Composites Part B: Engineering*, vol. 43, no. 2, pp. 354–360, 2012.

[16] H. Hahn and S. Tsai, *Introduction to Composite Materials*. Oxfordshire: Taylor & Francis, 1980.

[17] M. M. Abdalla, S. Setoodeh, and Z. Guerdal, "Design of variable stiffness composite panels for maximum fundamental frequency using lamination parameters," *Composite Structures*, vol. 81, no. 2, pp. 283–291, 2007.

[18] S. T. IJsselmuiden, *Optimal Design of Variable Stiffness Composite Structures using Lamination Parameters*. Doctoral thesis, Delft University of Technology, 2011.

[19] B. C. Kim, K. Potter, and P. M. Weaver, "Continuous tow shearing for manufacturing variable angle tow composites," *Composites Part A: Applied Science and Manufacturing*, vol. 43, no. 8, pp. 1347–1356, 2012.

[20] A. Blom, C. S. Lopes, P. J. Kromwijk, Z. Guerdal, and P. P. Camanho, "A theoretical model to study the influence of tow-drop areas on the stiffness and strength of variable-stiffness laminates," *Journal of Composite Materials*, vol. 43, no. 5, pp. 403–425, 2009.

[21] A. Blom, P. Stickler, and Z. Guerdal, "Design and manufacture of a variable-stiffness cylindrical shell," in *Proceedings of the SAMPE Europe 30th International Conference*, pp. 1–8, 2009.

[22] C. S. Lopes, P. P. Camanho, Z. Guerdal, and B. F. Tatting, "Progressive failure analysis of tow-placed, variable-stiffness composite panels," *International Journal of Solids and Structures*, vol. 44, no. 25, pp. 8493–8516, 2007.

[23] A. Beakou, M. Cano, J. B. Le Cam, and V. Verney, "Modelling slit tape buckling during automated prepreg manufacturing: A local approach," *Composite Structures*, vol. 93, no. 10, pp. 2628–2635, 2011.

[24] R. P. Smith, Z. Qureshi, R. J. Scaife, and H. M. El-Dessouky, "Limitations of processing carbon fibre reinforced plastic/polymer material using automated fibre placement technology," *Journal of Reinforced Plastics and Composites*, vol. 35, no. 21, pp. 1527–1542, 2016.

[25] B. C. Kim, P. M. Weaver, and K. Potter, "Manufacturing characteristics of the continuous tow shearing method for manufacturing of variable angle tow composites," *Composites Part A: Applied Science and Manufacturing*, vol. 61, pp. 141–151, 2014.

[26] V. Mishra, D. M. J. Peeters, and M. M. Abdalla, "Stiffness and buckling analysis of variable stiffness laminates including the effect of automated fibre placement defects," *Composite Structures*, vol. 226, 2019.

[27] T. J. Dodwell, R. Butler, and A. T. Rhead, "Optimum fiber steering of composite plates for buckling and manufacturability," *AIAA Journal*, vol. 54, no. 3, pp. 1146–1149, 2016.

[28] G. Raju, Z. Wu, and P. M. Weaver, "Buckling and postbuckling of variable angle tow composite plates under in-plane shear loading," *International Journal of Solids and Structures*, vol. 58, pp. 270–287, 2015.

[29] H. B. Hellweg and M. A. Crisfield, "A new arc-length method for handling sharp snap-backs," *Computers & Structures*, vol. 66, no. 5, pp. 704–709, 1998.

[30] K. Liang, M. Ruess, and M. Abdalla, "The Koiter-Newton approach using von Kármán kinematics for buckling analyses of imperfection sensitive structures," *Computer Methods in Applied Mechanics and Engineering*, vol. 279, pp. 440–468, 2014.

[31] N. Hu and R. Burgueño, "Buckling-induced smart applications: Recent advances and trends," *Smart Materials and Structures*, vol. 24, no. 6, p. 063001, 2015.

[32] C. Kassapoglou, *Design and analysis of composite structures : with applications to aerospace structures*. Aerospace series, Chichester, West Sussex, United Kingdom: John Wiley & Sons Inc., second edition. ed., 2013.

[33] S. G. P. Castro, *Semi-analytical tools for the analysis of laminated composite cylindrical and conical imperfect shells under various loading and boundary conditions*. Doctoral thesis, Clausthal University of Technology, 2014.

[34] S. G. P. Castro, C. Mittelstedt, F. A. C. Monteiro, M. A. Arbelo, G. Ziegmann, and R. Degenhardt, "Linear buckling predictions of unstiffened laminated composite cylinders and cones under various loading and boundary conditions using semi-analytical models," *Composite Structures*, vol. 118, pp. 303–315, 2014.

[35] C. Bisagni and R. Vescovini, "Analytical formulation for local buckling and post-buckling analysis of stiffened laminated panels," *Thin-Walled Structures*, vol. 47, no. 3, pp. 318–334, 2009.

[36] V. Oliveri and A. Milazzo, "A Rayleigh-Ritz approach for postbuckling analysis of variable angle tow composite stiffened panels," *Computers & Structures*, vol. 196, pp. 263–276, 2018.

[37] R. Vescovini and C. Bisagni, "Semi-analytical buckling analysis of omega stiffened panels under multi-axial loads," *Composite Structures*, vol. 120, pp. 285–299, 2014.

[38] C. Mittelstedt and M. Beerhorst, "Closed-form buckling analysis of compressively loaded composite plates braced by omega-stringers," *Composite Structures*, vol. 88, no. 3, pp. 424–435, 2009.

[39] H.-T. Thai and D.-H. Choi, "A simple first-order shear deformation theory for laminated composite plates," *Composite Structures*, vol. 106, pp. 754–763, 2013.

[40] B. H. Coburn, Z. Wu, and P. M. Weaver, "Buckling analysis of stiffened variable angle tow panels," *Composite Structures*, vol. 111, pp. 259–270, 2014.

[41] R. M. J. Groh and P. M. Weaver, "Buckling analysis of variable angle tow, variable thickness panels with transverse shear effects," *Composite Structures*, vol. 107, pp. 482–493, 2014.

[42] J. N. Reddy, *Mechanics of laminated composite plates and shells : theory and analysis*. Boca Raton: CRC Press, 2nd ed., 2004.

[43] R. Vescovini and C. Bisagni, "Buckling analysis and optimization of stiffened composite flat and curved panels," *AIAA Journal*, vol. 50, no. 4, pp. 904–915, 2012.

[44] C. Mittelstedt, "Closed-form analysis of the buckling loads of uniaxially loaded blade-stringer-stiffened composite plates considering periodic boundary conditions," *Thin-Walled Structures*, vol. 45, no. 4, pp. 371–382, 2007.

[45] R. Vescovini and C. Bisagni, "Two-step procedure for fast post-buckling analysis of composite stiffened panels," *Computers & Structures*, vol. 128, pp. 38–47, 2013.

[46] R. Vescovini, L. Dozio, M. D´ Ottavio, and O. Polit, "On the application of the Ritz method to free vibration and buckling analysis of highly anisotropic plates," *Composite Structures*, vol. 192, pp. 460–474, 2018.

[47] S. G. P. Castro and M. V. Donadon, "Assembly of semi-analytical models to address linear buckling and vibration of stiffened composite panels with debonding defect," *Composite Structures*, vol. 160, pp. 232–247, 2017.

[48] *ABAQUS/Standard User's Manual, Version 2019*. Simulia, 2019.

[49] Z. Wu, G. Raju, and P. M. Weaver, "Postbuckling analysis of variable angle tow composite plates," *International Journal of Solids and Structures*, vol. 50, no. 10, pp. 1770–1780, 2013.

[50] K. C. Wu, "Design and analysis of tow-steered composite shells using fiber placement," in *American Society for Composites 23rd Annual Technical Conference*, pp. 1124 – 1141, 2008.

[51] S. G. P. Castro, M. V. Donadon, and T. A. M. Guimarães, "ES-PIM applied to buckling of variable angle tow laminates," *Composite Structures*, vol. 209, pp. 67–78, 2018.

[52] K. C. Wu, B. K. Stanford, G. A. Hrinda, Z. Wang, R. A. Martin, and H. A. Kim, *Structural assessment of advanced tow-steered shells*. Structures, Structural Dynamics, and Materials and Co-located Conferences, American Institute of Aeronautics and Astronautics, 2013.

[53] J. D. Hunter, "Matplotlib: A 2D graphics environment," *Computing in Science & Engineering*, vol. 9, no. 3, pp. 90–95, 2007.

[54] R. Goldman, "Curvature formulas for implicit curves and surfaces," *Computer Aided Geometric Design*, vol. 22, no. 7, pp. 632–658, 2005.

[55] S. G. P. Castro, "Semi-analytical models for panels," DOI: 10.5281/zenodo.2541523. Version 0.2.0, 2019.

[56] M. S. Ewing, R. J. Hinger, and A. W. Leissa, "On the validity of the reduced bending stiffness method for laminated composite plate analysis," *Composite Structures*, vol. 9, no. 4, pp. 301–317, 1988.

[57] A. Peano, "Hierarchies of conforming finite elements for plane elasticity and plate bending," *Computers & Mathematics with Applications*, vol. 2, no. 3, pp. 211–224, 1976.

[58] N. S. Bardell, "Free vibration analysis of a flat plate using the hierarchical finite element method," *Journal of Sound and Vibration*, vol. 151, no. 2, pp. 263–289, 1991.

[59] "Nodes and weights of gaussian quadrature calculator." `https://keisan.casio.com/exec/system/132911461`. Accessed: 26/11/2019.

[60] P. Virtanen, R. Gommers, T. E. Oliphant, M. Haberland, T. Reddy, D. Cournapeau, E. Burovski, P. Peterson, W. Weckesser, J. Bright, S. J. van der Walt, M. Brett, J. Wilson, K. Jarrod Millman, N. Mayorov, A. R. J. Nelson, E. Jones, R. Kern, E. Larson, C. Carey, İ. Polat, Y. Feng, E. W. Moore, J. Vand erPlas, D. Laxalde, J. Perktold, R. Cimrman, I. Henriksen, E. A. Quintero, C. R. Harris, A. M. Archibald, A. H. Ribeiro, F. Pedregosa, P. van Mulbregt, and Contributors, "SciPy 1.0–Fundamental Algorithms for Scientific Computing in Python," *arXiv e-prints*, p. arXiv:1907.10121, Jul 2019.

[61] D. Kraft, *A Software Package for Sequential Quadratic Programming*. DLR German Aerospace Center – Institute for Flight Mechanics, Koln, Germany, Wiss. Berichtswesen d. DFVLR, 1988.

[62] M. P. Stanić, A. S. Cvetković, and T. V. Tomović, "Error bound of certain Gaussian quadrature rules for trigonometric polynomials," *Kragujevac Journal of Mathematics*, vol. 36, no. 1, pp. 83–72, 2012.

[63] S. E. Mousavi and N. Sukumar, "Generalized gaussian quadrature rules for discontinuities and crack singularities in the extended finite element method," *Computer Methods in Applied Mechanics and Engineering*, vol. 199, no. 49, pp. 3237–3249, 2010.

[64] K. Gliesche, T. Huebner, and H. Orawetz, "Application of the tailored fibre placement (TFP) process for a local reinforcement on an "open-hole" tension plate from carbon/epoxy laminates," *Composites Science and Technology*, vol. 63, no. 1, pp. 81–88, 2003.

Appendix A

Rotated Stiffness Matrix

This appendix shows the calculations to obtain the rotated stiffness matrix to be used in order to compute the ABD matrix. With the essential composite material mechanical properties (E_{xx}, E_{yy}, ν_{xy}, G_{xy}) defined, the stress-strain relation for a uni-directional ply with a plain stress assumption can be written as shown in Equation A.1 [32].

$$\begin{bmatrix} \sigma_{xx} \\ \sigma_{yy} \\ \tau_{xy} \end{bmatrix} = \begin{bmatrix} \frac{E_{xx}}{x-\nu_{xy}\nu_{yx}} & \frac{\nu_{xy}E_{yy}}{x-\nu_{xy}\nu_{yx}} & 0 \\ \frac{\nu_{xy}E_{yy}}{x-\nu_{xy}\nu_{yx}} & \frac{E_{yy}}{x-\nu_{xy}\nu_{yx}} & 0 \\ 0 & 0 & G_{xy} \end{bmatrix} \begin{bmatrix} \varepsilon_{xx} \\ \varepsilon_{yy} \\ \gamma_{xy} \end{bmatrix} \tag{A.1}$$

The transverse Poisson's ratio ν_{yx} is obtained by means of Equation A.2.

$$\nu_{yx} = \nu_{xy}\frac{E_{yy}}{E_{xx}} \tag{A.2}$$

For a rotated fibre orientation in the coordinate system displayed in Figure A.1, the following relation exists: $[\sigma_\theta] = [M][Q][M]^T[\epsilon_\theta]$, relating the global stress $[\sigma_\theta]$ and global strain $[\varepsilon_\theta]$ in the x-y coordinate system. $[M][Q][M]^T$ is the rotated fibre stiffness by an angle θ, with [Q] the stiffness matrix of Equation A.1. The rotation matrix [M] is given by Equation A.3, with $m = \cos\theta$ and $n = \sin\theta$.

$$[M] = \begin{bmatrix} m^2 & n^2 & 2mn \\ n^2 & m^2 & -2mn \\ -mn & mn & m^2 - n^2 \end{bmatrix} \tag{A.3}$$

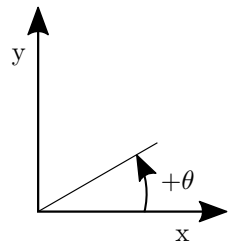

Figure A.1: Fibre orientation θ definition.

Appendix B

Semi-Analytical Buckling Matrix Formulation

This appendix gives the matrix definition of first the strain relationship in Section B.1, followed by the definition of the linear constitutive and geometric stiffness matrix in Section B.2.

B.1 Strain Relations

The relation of between the strains and the shape functions of Equation 6.18 can be written as Equation B.1. The matrix $[B_0]$ contains the linear strain terms, whereas matrix $[B_L]$ contains the non-linear components of the strain definition [47].

$$[B_0] + \frac{1}{2}[B_L] = \begin{bmatrix} B_{0_P} \\ B_{\kappa_P} \end{bmatrix} + \frac{1}{2}\begin{bmatrix} B_{L_P} \\ 0 \end{bmatrix} \tag{B.1}$$

Furthermore, the submatrices of $[B_0]$ and $[B_L]$ are defined in Equation B.2, B.3 and B.4, for $[B_{0_P}]$, $[B_{\kappa_P}]$ and $[B_{L_P}]$ respectively, where the chain rule has been applied along the change to the natural coordinate system. S_u, S_v and S_w are the row vectors containing the shape functions for the displacements as defined in Section 6.1.4.

$$[B_{0_P}] = \begin{bmatrix} \left(\frac{2}{L}\right) S_{u,\xi} \\ \left(\frac{2}{W}\right) S_{v,\eta} \\ \left(\frac{2}{W}\right) S_{u,\eta} + \left(\frac{2}{L}\right) S_{v,\xi} \end{bmatrix} \tag{B.2}$$

$$[B_{\kappa_P}] = \begin{bmatrix} -\left(\frac{4}{L^2}\right) S_{w,\xi\xi} \\ -\left(\frac{4}{W^2}\right) S_{w,\eta\eta} \\ -2\left(\frac{4}{LW}\right) S_{w,\xi\eta} \end{bmatrix} \tag{B.3}$$

$$[B_{L_P}] = \begin{bmatrix} \left(\frac{4}{L^2}\right) w_{,\xi} S_{w,\xi} \\ \left(\frac{4}{W^2}\right) w_{,\eta} S_{w,\eta} \\ \left(\frac{4}{LW}\right) \left(w_{,\xi} S_{w,\eta} + w_{,\eta} S_{w,\xi}\right) \end{bmatrix} \tag{B.4}$$

B.2 Stiffness Matrices

Both the linear constitutive and geometrical stiffness matrices consists of a smaller 3x3 repeatable matrix, dependent on the three degrees of freedom of the plate. These repeatable matrices are situated row-wise by indices i, j and column-wise by indices k, l, with their entries given by Equation B.5 and B.6 [47].

$$
\begin{aligned}
K_p^{ijkl}(1,1) &= A_{11}\frac{W}{L}S_{u,\xi}^{ij}S_{u,\xi}^{kl} + A_{16}\left(S_{u,\xi}^{ij}S_{u,\eta}^{kl} + S_{u,\eta}^{ij}S_{u,\xi}^{kl}\right) + A_{66}\frac{L}{W}S_{u,\eta}^{ij}S_{u,\eta}^{kl} \\
K_p^{ijkl}(1,2) &= A_{12}S_{u,\xi}^{ij}S_{v,\eta}^{kl} + A_{16}\frac{W}{L}S_{u,\xi}^{ij}S_{v,\xi}^{kl} + A_{26}\frac{L}{W}S_{u,\eta}^{ij}S_{v,\eta}^{kl} + A_{66}S_{u,\eta}^{ij}S_{v,\eta}^{kl} \\
K_p^{ijkl}(1,3) &= -2\frac{W}{L^2}B_{11}S_{u,\xi}^{ij}S_{w,\xi\xi}^{kl} - \frac{2}{W}B_{12}S_{u,\xi}^{ij}S_{w,\eta\eta}^{kl} - \frac{2}{L}B_{16}\left(S_{u,\xi}^{ij}S_{w,\xi\eta}^{kl} + S_{u,\eta}^{ij}S_{w,\xi\xi}^{kl}\right) \\
&\quad -2\frac{L}{W^2}B_{26}S_{u,\eta}^{ij}S_{w,\eta\eta}^{kl} - \frac{4}{W}S_{u,\eta}^{ij}S_{w,\xi\eta}^{kl} \\
K_p^{ijkl}(2,1) &= A_{12}S_{v,\eta}^{ij}S_{u,\xi}^{kl} + A_{16}\frac{W}{L}S_{v,\xi}^{ij}S_{u,\xi}^{kl} + A_{26}\frac{L}{W}S_{v,\eta}^{ij}S_{u,\eta}^{kl} + A_{66}S_{v,\xi}^{ij}S_{u,\eta}^{kl} \\
K_p^{ijkl}(2,2) &= A_{22}\frac{L}{W}S_{v,\eta}^{ij}S_{v,\eta}^{kl} + A_{26}\left(S_{v,\xi}^{ij}S_{v,\eta}^{kl} + S_{v,\eta}^{ij}S_{v,\xi}^{kl}\right) + A_{66}\frac{W}{L}S_{v,\xi}^{ij}S_{v,\xi}^{kl} \\
K_p^{ijkl}(2,3) &= -\frac{2}{L}B_{12}S_{v,\eta}^{ij}S_{w,\xi\xi}^{kl} - 2\frac{W}{L^2}B_{16}S_{v,\xi}^{ij}S_{w,\xi\xi}^{kl} - 2\frac{L}{W^2}B_{22}S_{v,\eta}^{ij}S_{w,\eta\eta}^{kl} \\
&\quad -2\frac{2}{W}B_{26}\left(S_{v,\xi}^{ij}S_{w,\eta\eta}^{kl} + 2S_{v,\eta}^{ij}S_{w,\xi\eta}^{kl}\right) - \frac{4}{L}B_{66}S_{v,\xi}^{ij}S_{w,\xi\eta}^{kl} \\
K_p^{ijkl}(3,1) &= -2\frac{W}{L^2}B_{11}S_{w,\xi\xi}^{ij}S_{u,\xi}^{kl} - \frac{2}{W}B_{12}S_{w,\eta\eta}^{ij}S_{u,\xi}^{kl} - \frac{2}{L}B_{16}\left(S_{w,\xi\eta}^{ij}S_{u,\xi}^{kl} + S_{w,\xi\xi}^{ij}S_{u,\eta}^{kl}\right) \\
&\quad -2\frac{L}{W^2}B_{26}S_{w,\eta\eta}^{ij}S_{u,\eta}^{kl} - \frac{4}{W}S_{w,\xi\eta}^{ij}S_{u,\eta}^{kl} \\
K_p^{ijkl}(3,2) &= -\frac{2}{L}B_{12}S_{w,\xi\xi}^{ij}S_{v,\eta}^{kl} - 2\frac{W}{L^2}B_{16}S_{w,\xi\xi}^{ij}S_{v,\xi}^{kl} - 2\frac{L}{W^2}B_{22}S_{w,\eta\eta}^{ij}S_{v,\eta}^{kl} \\
&\quad -2\frac{2}{W}B_{26}\left(S_{w,\eta\eta}^{ij}S_{v,\xi}^{kl} + 2S_{w,\xi\eta}^{ij}S_{v,\eta}^{kl}\right) - \frac{4}{L}B_{66}S_{w,\xi\eta}^{ij}S_{v,\xi}^{kl} \\
K_p^{ijkl}(3,3) &= 4\frac{W}{L^3}D_{11}S_{w,\xi\xi}^{ij}S_{w,\xi\xi}^{kl} + \frac{4}{LW}D_{12}\left(S_{w,\xi\xi}^{ij}S_{w,\eta\eta}^{kl} + S_{w,\eta\eta}^{ij}S_{w,\xi\xi}^{kl}\right) + 4\frac{L}{W^3}D_{22}S_{w,\eta\eta}^{ij}S_{w,\eta\eta}^{kl} \\
&\quad +\frac{8}{L^2}D_{16}\left(S_{w,\xi\xi}^{ij}S_{w,\xi\eta}^{kl} + S_{w,\xi\eta}^{ij}S_{w,\xi\xi}^{kl}\right) \\
&\quad +\frac{8}{W^2}D_{26}\left(S_{w,\xi\eta}^{ij}S_{w,\eta\eta}^{kl} + S_{w,\eta\eta}^{ij}S_{w,\xi\eta}^{kl}\right) + \frac{16}{LW}S_{w,\xi\eta}^{ij}S_{w,\xi\eta}^{kl}
\end{aligned}
\tag{B.5}
$$

$$
K_{G_p}^{ijkl}(3,3) = \frac{W}{L}N_{xx}S_{w,\xi}^{ij}S_{w,\xi}^{kl} + \frac{L}{W}N_{yy}S_{w,\eta}^{ij}S_{w,\eta}^{kl} + N_{xy}\left(S_{w,\eta}^{ij}S_{w,\xi}^{kl} + S_{w,\xi}^{ij}S_{w,\eta}^{kl}\right) \tag{B.6}
$$

Appendix C

Semi-Analytical Verification Cases Data

This appendix presents the convergence data for the semi-analytical models of Chapter 9. For each case, first the smeared thickness results are given, followed by the convergence difference of the smeared solution compared to the result with 16 shape functions and 17 integration points in both x and y. Finally, the discrete thickness results are displayed.

Table C.1: Convergence study of the semi-analytical smeared thickness buckling λ of case 1.

		Number of integration points [-]													
		4	5	6	7	8	9	10	11	12	13	14	15	16	17
Number of shape functions [-]	4	0.90	0.91	0.94	0.94	0.94	0.94	0.94	0.94	0.94	0.94	0.94	0.94	0.94	0.94
	5		0.81	0.83	0.83	0.82	0.83	0.83	0.83	0.83	0.83	0.83	0.83	0.83	0.83
	6			0.78	0.78	0.78	0.78	0.78	0.78	0.78	0.78	0.78	0.78	0.78	0.78
	7				0.78	0.77	0.77	0.77	0.77	0.77	0.77	0.77	0.77	0.77	0.77
	8					0.75	0.76	0.76	0.76	0.76	0.76	0.76	0.76	0.76	0.76
	9						0.76	0.76	0.76	0.76	0.76	0.76	0.76	0.76	0.76
	10							0.75	0.76	0.76	0.76	0.76	0.76	0.76	0.76
	11								0.76	0.75	0.76	0.76	0.76	0.76	0.76
	12									0.75	0.75	0.75	0.75	0.75	0.75
	13										0.75	0.75	0.75	0.75	0.75
	14											0.75	0.75	0.75	0.75
	15												0.75	0.75	0.75
	16													0.75	0.75

Table C.2: Relative difference of the semi-analytical smeared thickness buckling λ compared to the solution with 16 shape functions and 17 integration points of case 1.

Number of shape functions [-]	Number of integration points [-]													
	4	5	6	7	8	9	10	11	12	13	14	15	16	17
4	20.00	21.74	25.93	25.48	25.22	25.48	25.31	25.33	25.38	25.33	25.34	25.34	25.35	25.32
5		7.72	10.81	10.00	9.84	10.07	10.01	10.04	9.99	10.03	10.02	10.03	10.02	10.04
6			3.49	4.26	3.91	4.04	4.11	4.14	4.11	4.13	4.13	4.13	4.12	4.13
7				3.82	2.51	2.92	2.97	3.02	2.99	3.00	3.00	3.00	3.00	3.01
8					0.07	1.56	1.54	1.65	1.63	1.64	1.63	1.64	1.63	1.64
9						1.59	1.40	1.51	1.49	1.50	1.49	1.49	1.49	1.50
10							0.26	0.86	0.90	0.94	0.94	0.94	0.93	0.94
11								0.82	0.64	0.65	0.69	0.69	0.69	0.70
12									-0.13	0.33	0.39	0.41	0.41	0.41
13										0.34	0.26	0.30	0.31	0.32
14											-0.28	0.12	0.15	0.16
15												0.16	0.10	0.13
16													-0.31	0.00

Table C.3: Convergence study of the semi-analytical discrete thickness buckling λ of case 1.

Number of shape functions [-]	Number of integration points [-]													
	4	5	6	7	8	9	10	11	12	13	14	15	16	17
4	1.03	0.89	0.89	1.16	1.00	0.98	0.95	1.18	1.00	1.06	1.06	1.05	0.98	1.05
5		0.92	0.77	1.05	0.94	0.84	0.83	1.08	0.83	0.94	0.95	0.93	0.84	0.91
6			0.69	0.97	0.87	0.79	0.79	1.02	0.78	0.88	0.90	0.86	0.78	0.86
7				0.96	0.84	0.77	0.76	1.00	0.75	0.87	0.88	0.85	0.77	0.85
8					0.81	0.75	0.74	0.97	0.73	0.85	0.86	0.84	0.76	0.84
9						0.73	0.72	0.95	0.72	0.84	0.84	0.83	0.76	0.83
10							0.71	0.92	0.71	0.83	0.82	0.82	0.75	0.82
11								0.90	0.70	0.82	0.81	0.81	0.74	0.82
12									0.69	0.81	0.80	0.80	0.73	0.81
13										0.80	0.78	0.79	0.73	0.79
14											0.77	0.78	0.72	0.79
15												0.78	0.71	0.78
16													0.71	0.76

Table C.4: Convergence study of the semi-analytical smeared thickness buckling λ of case 2.

Number of shape functions [-] \ Number of integration points [-]	4	5	6	7	8	9	10	11	12	13	14	15	16	17
4	9.84	9.70	9.76	9.90	9.97	9.96	9.95	9.95	9.96	9.96	9.96	9.96	9.96	9.96
5		8.25	9.47	9.43	9.44	9.41	9.42	9.42	9.42	9.42	9.42	9.42	9.42	9.43
6			8.63	9.04	8.98	8.98	8.98	8.98	8.99	8.99	8.99	8.99	8.99	8.99
7				8.50	8.64	8.61	8.64	8.64	8.65	8.65	8.65	8.65	8.65	8.65
8					8.35	8.48	8.49	8.50	8.50	8.50	8.50	8.50	8.50	8.50
9						8.16	8.24	8.27	8.28	8.28	8.28	8.28	8.28	8.29
10							8.11	8.20	8.21	8.21	8.21	8.21	8.21	8.21
11								8.09	8.17	8.17	8.17	8.17	8.17	8.17
12									8.09	8.14	8.15	8.15	8.15	8.15
13										8.06	8.12	8.12	8.12	8.12
14											8.06	8.10	8.10	8.10
15												8.03	8.08	8.08
16													8.03	8.07

Table C.5: Relative difference of the semi-analytical smeared thickness buckling λ compared to the solution with 16 shape functions and 17 integration points of case 2.

Number of shape functions [-] \ Number of integration points [-]	4	5	6	7	8	9	10	11	12	13	14	15	16	17
4	21.95	20.22	20.95	22.66	23.58	23.44	23.32	23.33	23.43	23.43	23.41	23.36	23.42	23.45
5		2.24	17.31	16.82	16.95	16.61	16.69	16.69	16.77	16.77	16.76	16.71	16.76	16.78
6			6.96	11.95	11.32	11.33	11.30	11.31	11.40	11.40	11.39	11.35	11.39	11.41
7				5.36	7.04	6.62	7.08	7.11	7.21	7.19	7.17	7.14	7.18	7.20
8					3.44	5.06	5.23	5.28	5.33	5.32	5.31	5.28	5.32	5.33
9						1.16	2.11	2.50	2.65	2.65	2.64	2.60	2.64	2.65
10							0.47	1.63	1.77	1.78	1.77	1.74	1.77	1.78
11								0.24	1.20	1.25	1.25	1.22	1.25	1.27
12									0.29	0.92	0.94	0.92	0.95	0.97
13										-0.19	0.56	0.57	0.60	0.62
14											-0.17	0.32	0.40	0.42
15												-0.51	0.11	0.15
16													-0.46	0.00

Table C.6: Convergence study of the semi-analytical discrete thickness buckling λ of case 2.

Number of shape functions [-] \ Number of integration points [-]	4	5	6	7	8	9	10	11	12	13	14	15	16	17
4	9.09	12.58	12.14	11.38	12.58	11.02	13.05	12.00	11.82	13.24	13.39	11.55	11.93	11.85
5		10.14	10.51	10.75	12.00	10.44	12.27	11.02	11.32	12.25	12.38	10.63	11.38	11.01
6			9.63	10.24	10.83	9.98	11.26	10.48	11.15	11.37	11.84	10.12	11.00	10.62
7				9.46	10.24	9.52	10.61	9.93	10.48	10.88	11.27	9.83	10.54	10.21
8					9.61	9.05	10.21	9.60	10.09	10.61	10.78	9.56	10.23	9.95
9						8.45	9.79	9.24	9.68	10.32	10.32	9.22	9.92	9.70
10							9.36	9.01	9.52	10.08	10.07	9.03	9.72	9.53
11								8.76	9.22	9.79	9.87	8.90	9.48	9.39
12									8.98	9.61	9.66	8.77	9.37	9.20
13										9.42	9.37	8.65	9.17	9.08
14											9.22	8.51	9.04	8.95
15												8.31	8.94	8.74
16													8.83	8.55

Table C.7: Convergence study of the semi-analytical smeared thickness buckling λ of case 3.

Number of shape functions [-] \ Number of integration points [-]	4	5	6	7	8	9	10	11	12	13	14	15	16	17
4	34.84	35.38	36.27	35.95	35.93	36.00	35.97	36.00	35.98	36.00	35.99	36.00	35.99	36.00
5		30.88	30.48	30.22	30.57	30.46	30.48	30.48	30.48	30.48	30.48	30.48	30.48	30.48
6			26.56	26.78	27.35	27.22	27.25	27.23	27.24	27.24	27.24	27.24	27.24	27.24
7				26.46	26.82	26.93	26.92	26.90	26.91	26.91	26.91	26.91	26.91	26.91
8					25.99	26.47	26.44	26.43	26.43	26.43	26.43	26.43	26.43	26.43
9						25.94	26.31	26.24	26.29	26.28	26.28	26.28	26.28	26.28
10							25.79	25.97	26.05	26.05	26.04	26.04	26.04	26.04
11								25.71	25.94	25.94	25.95	25.95	25.95	25.95
12									25.65	25.85	25.88	25.87	25.87	25.87
13										25.61	25.79	25.79	25.80	25.80
14											25.58	25.73	25.75	25.74
15												25.55	25.69	25.69
16													25.53	25.65

Table C.8: Relative difference of the semi-analytical smeared thickness buckling λ compared to the solution with 16 shape functions and 17 integration points of case 3.

Number of shape functions [-] \ Number of integration points [-]	4	5	6	7	8	9	10	11	12	13	14	15	16	17
4	35.84	37.95	41.39	40.16	40.09	40.36	40.24	40.34	40.28	40.34	40.32	40.34	40.32	40.34
5		20.39	18.85	17.82	19.18	18.75	18.85	18.84	18.83	18.84	18.84	18.84	18.84	18.85
6			3.55	4.41	6.62	6.12	6.23	6.18	6.19	6.20	6.19	6.20	6.19	6.20
7				3.16	4.58	5.00	4.96	4.88	4.90	4.91	4.91	4.91	4.91	4.91
8					1.34	3.21	3.10	3.03	3.06	3.06	3.06	3.06	3.06	3.06
9						1.15	2.56	2.31	2.48	2.46	2.46	2.46	2.46	2.46
10							0.56	1.26	1.58	1.54	1.54	1.54	1.54	1.54
11								0.24	1.12	1.12	1.19	1.17	1.17	1.17
12									-0.01	0.78	0.89	0.85	0.86	0.86
13										-0.15	0.57	0.55	0.60	0.58
14											-0.28	0.33	0.39	0.37
15												-0.39	0.18	0.17
16													-0.45	0.00

Table C.9: Convergence study of the semi-analytical discrete thickness buckling λ of case 3.

Number of shape functions [-] \ Number of integration points [-]	4	5	6	7	8	9	10	11	12	13	14	15	16	17
4	48.56	47.34	45.37	41.83	36.58	38.53	38.56	44.14	43.30	41.07	39.48	38.34	37.38	37.91
5		36.64	38.62	37.87	28.70	33.67	32.69	37.18	34.60	34.28	33.77	30.60	31.96	31.64
6			30.66	30.99	24.58	29.63	28.56	33.46	30.81	30.26	29.99	26.76	28.52	27.85
7				29.34	23.45	28.59	28.59	32.80	29.78	29.42	29.11	26.10	27.92	27.35
8					22.22	27.43	28.04	32.07	28.92	28.81	28.45	25.59	27.41	26.67
9						26.16	27.40	31.70	28.61	28.52	27.96	25.38	26.99	26.37
10							26.50	30.54	27.93	28.06	27.51	24.85	26.67	26.03
11								29.54	27.49	27.53	27.08	24.60	26.42	25.86
12									26.96	26.87	26.66	24.28	26.15	25.60
13										26.36	26.04	24.07	25.99	25.41
14											25.52	23.79	25.72	25.19
15												23.42	25.49	24.89
16													25.16	24.65

Appendix D

Buckling Verification Comparison Results

This appendix presents the additional figures of the static analysis comparison. The displacement fields for u, v and w are given in Figures D.1, D.2 and D.3 for case 1, and in Figures D.4, D.5 and D.6 for case 2.

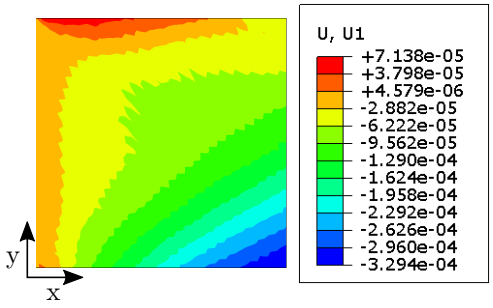

(a) Discrete thickness FEM results.

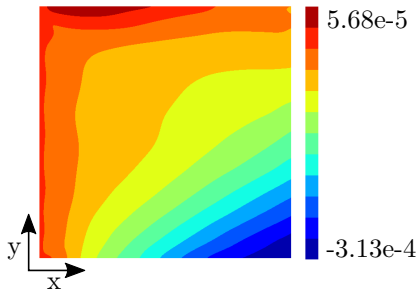

(b) Smeared thickness semi-analytical results.

Figure D.1: Static u displacement results in mm of case 1.

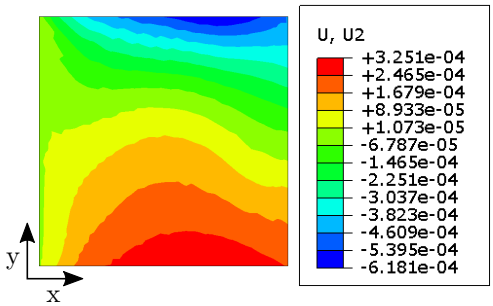

(a) Discrete thickness FEM results.

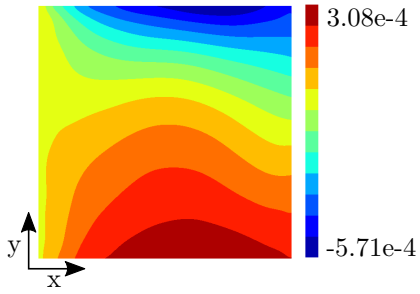

(b) Smeared thickness semi-analytical results.

Figure D.2: Static v displacement results in mm of case 1.

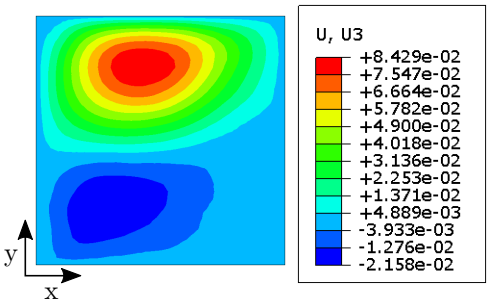

(a) Discrete thickness FEM results.

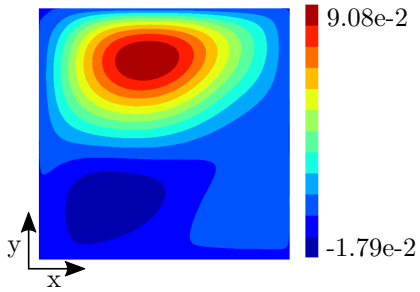

(b) Smeared thickness semi-analytical results.

Figure D.3: Static w displacement results in mm of case 1.

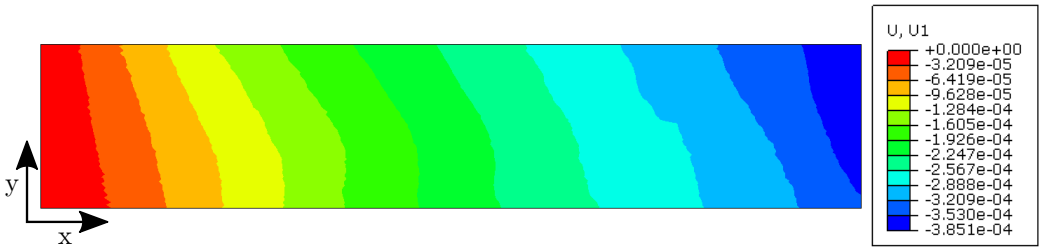

(a) Discrete thickness FEM results.

(b) Smeared thickness semi-analytical results.

Figure D.4: Static u displacement results in mm of case 2.

(a) Discrete thickness FEM results.

(b) Smeared thickness semi-analytical results.

Figure D.5: Static v displacement results in mm of case 2.

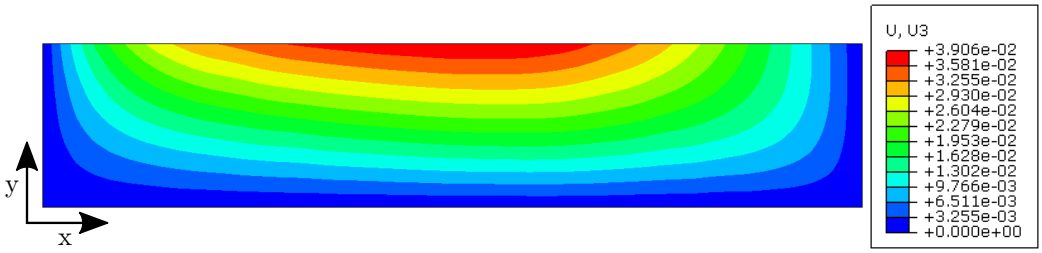

(a) Discrete thickness FEM results.

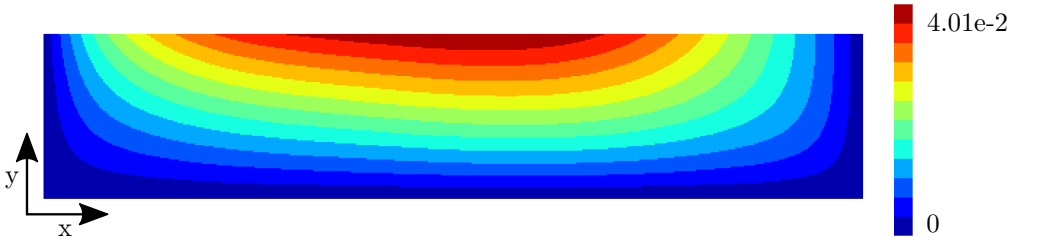

(b) Smeared thickness semi-analytical results.

Figure D.6: Static w displacement results in mm of case 2.

Appendix E

Optimisation Results

This appendix gives the optimal layup for each case and configuration. A ply is represented by the notation suggested by Guerdal et al. [8], as follow: $[\chi\langle\phi_1|\phi_2|\phi_3|\phi_4\rangle]$, where the CP relative locations are set to 0, 33%, 66% and 100%. All the layups for are given in Table E.1, E.2 and E.3, for case 1, 2 and 3 respectively, starting with the first ply being the bottom one.

Table E.1: Optimal stacking sequence for each layup configuration of case 1.

Layup configuration	λ [-]	Layup
Uniform determined	2.04	$[[0.0\langle-49.7\|-19.2\|19.7\|60.0\rangle],[0.0\langle49.7\|19.2\|-19.7\|-60.0\rangle],$ $[0.0\langle45.8\|24.2\|-18.4\|-56.2\rangle],[0.0\langle49.7\|19.2\|-19.7\|-60.0\rangle],$ $[0.0\langle-49.7\|-19.2\|19.7\|60.0\rangle]]$
Uniform free	2.07	$[[0.0\langle-52.5\|-20.1\|17.3\|60.0\rangle],[0.0\langle45.7\|22.3\|-20.7\|-60.0\rangle],$ $[0.0\langle-33.7\|-15.5\|22.9\|60.0\rangle],[0.0\langle-56.2\|-21.7\|-25.5\|-60.0\rangle],$ $[0.0\langle58.3\|17.4\|18.1\|60.0\rangle]]$
Smeared determined	2.06	$[[0.0\langle59.9\|15.1\|-23.0\|-60.0\rangle],[0.0\langle-59.9\|-15.1\|23.0\|60.0\rangle],$ $[0.0\langle-59.9\|-15.1\|23.0\|60.0\rangle],[0.0\langle59.9\|15.1\|-23.0\|-60.0\rangle]]$
Smeared free	2.08	$[[8.7\langle-24.7\|-12.5\|36.7\|58.5\rangle],[2.0\langle53.6\|13.2\|-31.2\|-59.9\rangle],$ $[15.2\langle-15.0\|-6.9\|45.8\|48.0\rangle],[12.7\langle59.7\|25.5\|-22.8\|-18.0\rangle]]$
Smeared free with $\chi = 0°$	2.04	$[[0.0\langle-60.0\|-16.5\|-23.7\|-59.9\rangle],[0.0\langle60.0\|19.2\|32.7\|60.0\rangle],$ $[0.0\langle60.0\|18.4\|30.5\|60.0\rangle],[0.0\langle-56.9\|-16.1\|-21.3\|-60.0\rangle]]$

Table E.2: Optimal stacking sequence for each layup configuration of case 2.

Layup configuration	λ [-]	Layup
Uniform determined	25.92	[[0.0⟨−49.7| − 19.2|19.7|60.0⟩],[0.0⟨49.7|19.2| − 19.7| − 60.0⟩], [0.0⟨45.8|24.2| − 18.4| − 56.2⟩],[0.0⟨49.7|19.2| − 19.7| − 60.0⟩], [0.0⟨−49.7| − 19.2|19.7|60.0⟩]]
Uniform free	33.85	[[−25.0⟨10.0|22.2|17.2|23.5⟩], [90.0⟨33.6|41.1|49.6|60.0⟩], [−85.4⟨−58.7| − 56.8| − 45.3| − 37.9⟩],[−48.0⟨3.6|0.2| − 1.5| − 0.8⟩], [59.0⟨3.4|11.4|8.7|17.2⟩]]
Smeared determined	21.84	[[0.5⟨−34.8| − 36.7| − 31.0| − 52.7⟩],[−0.5⟨34.8|36.7|31.0|52.7⟩], [−0.5⟨34.8|36.7|31.0|52.7⟩],[0.5⟨−34.8| − 36.7| − 31.0| − 52.7⟩]]
Smeared free	36.32	[[−35.2⟨2.5|10.0|8.4|22.5⟩],[7.8⟨−41.4| − 37.2| − 35.4| − 60.0⟩], [−89.1⟨−59.7| − 56.6| − 47.3| − 40.4⟩],[55.1⟨1.4|11.3|11.0|22.1⟩]]

Table E.3: Optimal stacking sequence for each layup configuration of case 3.

Layup configuration	λ [-]	Layup
Uniform determined	40.34	[[90.0⟨60.0|26.9|30.7|60.0⟩],[−90.0⟨−60.0| − 26.9| − 30.7| − 60.0⟩], [90.0⟨60.0|22.3|0.1| − 1.7⟩],[−90.0⟨−60.0| − 22.3| − 0.1|1.7⟩], [−2.6⟨31.1|53.0|59.8|44.1⟩],[−90.0⟨−60.0| − 22.3| − 0.1|1.7⟩], [90.0⟨60.0|22.3|0.1| − 1.7⟩],[−90.0⟨−60.0| − 26.9| − 30.7| − 60.0⟩], [90.0⟨60.0|26.9|30.7|60.0⟩]]
Uniform free	43.40	[[90.0⟨60.0|24.0|21.1|52.8⟩],[−90.0⟨−44.0| − 39.1| − 36.4| − 60.0⟩], [90.0⟨60.0|23.5|17.8|44.3⟩],[−94.0⟨−60.0| − 20.5|4.8| − 4.9⟩], [−4.2⟨29.6|45.9|38.3|60.0⟩],[−90.0⟨−38.7| − 7.4|12.0|2.3⟩], [90.0⟨60.0|23.5|18.2|45.1⟩],[−90.0⟨−43.7| − 40.3| − 36.2| − 60.0⟩], [90.0⟨60.0|24.0|20.9|52.4⟩]]
Smeared determined	37.96	[[39.3⟨28.1| − 15.6| − 17.0| − 1.1⟩],[−39.3⟨−28.1|15.6|17.0|1.1⟩], [88.2⟨−7.0|3.3|35.4|60.0⟩],[−88.2⟨7.0| − 3.3| − 35.4| − 60.0⟩], [−88.2⟨7.0| − 3.3| − 35.4| − 60.0⟩],[88.2⟨−7.0|3.3|35.4|60.0⟩], [−39.3⟨−28.1|15.6|17.0|1.1⟩],[39.3⟨28.1| − 15.6| − 17.0| − 1.1⟩]]
Smeared free	45.47	[[90.0⟨60.0|24.5|16.4|39.3⟩],[106.9⟨−58.3| − 48.3| − 15.4|3.1⟩], [85.5⟨−17.2|5.2|3.6| − 22.5⟩],[84.8⟨−14.9|4.4|2.5| − 12.1⟩], [−72.6⟨−7.8| − 6.2| − 46.1| − 54.0⟩],[−43.8⟨36.4| − 5.7| − 13.5|29.5⟩], [−59.1⟨3.1|11.4| − 31.7| − 59.9⟩],[40.2⟨45.3| − 15.4| − 31.7| − 3.1⟩]]
Smeared free CTS constraint	50.06	[[88.6⟨60.0|25.6|1.3|60.0⟩],[103.1⟨57.0|24.8| − 30.4|56.1⟩], [100.6⟨−55.6| − 36.0|7.1| − 60.0⟩],[−79.4⟨−60.0|8.5| − 34.3| − 55.3⟩], [75.9⟨60.0|5.8| − 10.4|60.0⟩],[82.6⟨−32.3|12.1| − 2.3|60.0⟩], [94.3⟨59.7|31.6| − 2.6|57.8⟩],[−49.3⟨10.6| − 2.4|1.2| − 6.9⟩]]